Dissertation

submitted to the

Combined Faculty of Mathematics, Engineering and Natural Sciences

of Heidelberg University, Germany

for the degree of

Doctor of Natural Sciences

Put forward by

Silva Mežinska

born in: Tukums (Latvia)

Oral examination: 17/01/2024

Coherent control of ^{6}Li multiphoton ionization by a bichromatic laser field

Referees: Priv.-Doz. Dr. Alexander Dorn
Prof. Dr. Markus Oberthaler

Abstract

This thesis deals with the coherent control of the multiphoton ionization (MPI) of ^{6}Li initially in the ground state by an ultrafast bichromatic laser field consisting of 780/390 nm radiation.

We demonstrate a left-right asymmetry control of the photoelectron angular distributions (PADs) of the main photoline with respect to a plane orthogonal to the laser polarization direction by varying the relative phase between the fundamental and second-harmonic (SH) pulses with subwavelength accuracy. Good agreement is found between the measurements and calculations at the appropriate absolute intensities of the two harmonics.

We also study the photoelectron spectra of the main photoline and the first Above-Threshold Ionization (ATI) photoline resulting from the ionization with temporally overlapping and non-overlapping two-color pulses. For this, we perform a delay scan between the two harmonics, which extends between the SH pulse advancing the fundamental pulse and vice versa with a delay step size of 3.36 times the optical period of the fundamental light of 2.6 fs. This reveals delay-dependent features of the photoelectron spectra. To several of them, we can attribute a dominant partial-wave character contributing to the interference pattern of the photoelectron spectrum. Since several MPI pathways exhibit intermediate resonances with long-living Rydberg states, we are also interested in whether the interaction order of the two harmonics has an effect on the photoelectron spectra in the case of both temporally overlapping and non-overlapping pulses. Here, we generally do not find overall agreement with our expectations according to the ionization pathways or the theoretical predictions, except for a few selected features.

All the experimental results are compared with calculations based on the solution of the time-dependent Schrödinger equation in the single-active electron approximation. These calculations were performed by Prof. Klaus Bartschat (Drake University, Des Moines, Iowa, USA).

Zusammenfassung

Diese Arbeit befasst sich mit der kohärenten Kontrolle der Mehrphotonen-Ionisation von ^{6}Li zunächst im Grundzustand durch ein ultraschnelles bichromatisches Laserfeld, bestehend aus 780/390 nm Strahlung.

Wir demonstrieren eine Links-Rechts-Asymmetrie-Kontrolle der Photonen-Elektronen-Winkelverteilungen der Hauptphotolinie bezüglich einer Ebene orthogonal zur Laserpolarisationsrichtung, indem wir die relative Phase zwischen den fundamentalen und zweitharmonischen Pulsen mit einer Genauigkeit unterhalb der Wellenlänge variieren. Bei den entsprechenden absoluten Intensitäten der beiden Harmonischen wurde eine gute Übereinstimmung zwischen den Messungen und den Berechnungen festgestellt.

Wir untersuchen die Photoelektronenspektren sowohl der Hauptphotolinie als auch der ersten oberhalb der Schwelle liegenden Ionisationslinie (ATI), die aus der Ionisation mit zeitlich überlappenden und nicht überlappenden Zweifarbenpulsen resultiert. Dazu führen wir eine Verzögerungsabtastung zwischen den beiden Harmonischen durch, die sich zwischen dem Puls der zweiten Harmonischen und dem Grundpuls mit einer Verzögerungsschrittgröße von 3,36 mal der optischen Periode des Grundlichts von 2,6 fs erstreckt. Dadurch werden verzögerungsabhängige Merkmale der Photoelektronenspektren sichtbar. Einige von ihnen haben einen dominanten Partialwellencharakter, der zum Interferenzmuster des Photoelektronenspektrums beiträgt. Da mehrere Mehrphotonen-Ionisationswege Zwischenresonanzen mit langlebigen Rydberg-Zuständen aufweisen, sind wir auch daran interessiert, ob die Wechselwirkungsordnung der beiden Harmonischen einen Einfluss auf die Photoelektronenspektren hat, und zwar sowohl bei zeitlich überlappenden als auch bei nicht überlappenden Pulsen. Hier haben wir im Allgemeinen keine Übereinstimmung mit unseren Erwartungen gemäß den Ionisierungspfaden oder den theoretischen Vorhersagen gefunden, mit Ausnahme einiger ausgewählter Merkmale.

Alle experimentellen Ergebnisse werden mit Berechnungen verglichen, die auf der Lösung der zeitabhängigen Schrödinger-Gleichung in der Näherung für ein einzelnes aktives Elektron basieren. Diese Berechnungen wurden von Prof. Klaus Bartschat (Drake University, Des Moines, Iowa, USA) durchgeführt.

Contents

List of Abbreviations

ATI	Above-Threshold Ionization
MPI	Multiphoton Ionization
NRMPI	Non-Resonant Multiphoton Ionization
OBI	Over-the-Barrier Ionization
PAD	Photoelectron Angular Distribution
ReMi	Reaction Microscope
REMPI	Resonance-Enhanced Multiphoton Ionization
SH	Second-Harmonic
TOF	Time-of-Flight

Introduction

Ionization of atoms and molecules in strong laser fields has proven to be a powerful tool for investigating properties of the ionizing laser field, the target, and understanding the ionization dynamics [1]. This field has especially flourished with the advent of ultrafast laser systems. In particular, one of the most frequently employed setups in ultrafast laboratories today is the Ti:Sapphire laser system, which generates laser pulses with a duration of tens of femtoseconds. Ti:Sapphire lasers produce light in the near-infrared range with their spectrum centered around 800 nm. Ultrafast radiation in other spectral ranges can be obtained by generating low- or high-order harmonics of the Ti:Sapphire laser pulses. For example, low-order harmonics can be produced by using nonlinear birefringent crystals. High-order harmonics, in turn, can be generated by focusing Ti:Sapphire laser pulses on a noble-gas target such as Ar or Xe [2]. Synchronizing the generated low- or high-order harmonic laser field with the fundamental radiation and the control of their relative phase with subfemtosecond accuracy has opened many opportunities for the coherent control of the strong-field ionization processes.

Strong-field ionization can occur in two ways – either via tunneling if the laser field is quasi-static [3] or by multiphoton absorption if the laser field varies rapidly in time [4]. In tunneling ionization, a fraction of the electrons directly leave their parent ions. At the same time, the remaining electrons are rescattered and can recombine with the parent ions. This is the so-called three-step model, which explains the generation of high-order harmonic radiation (HHG) consisting of trains of attosecond pulses in the extreme ultraviolet (XUV) spectral range [5, 6]. In the tunneling ionization regime, the mixing of the fundamental field with its second-harmonic (SH), where the latter is relatively weak and hence acts as a perturbation, has been applied to control the subcycle electric field structure that the rescattered electron moves in. This has enabled the generation of even-order high harmonics [7–9] in addition to the odd-order harmonics generated via the conventional single-color HHG. Furthermore, the technique has been applied to the measurement and control of attosecond XUV pulses by changing the relative phase between the two harmonics [10].

In multiphoton ionization (MPI), a two-color laser field of commensurate wavelengths induces ionization pathways that lead to the interference between even- and odd-parity partial waves of the ejected photoelectron. As a result, the photoelectron angular distributions (PADs) exhibit a left-right asymmetry with respect to the laser polarization direction, which depends on the relative phase between the two commensurate wavelengths. The left-right asymmetry control via interference between partial waves of opposite parities was first demonstrated with atomic rubidium in 1992 by Elliott and coworkers [11]. Their ionization scheme was based on the interference between single- and two-photon absorption ionization pathways. They observed emission-angle-dependent phase shifts

of the modulated photoelectron signals as a function of the relative delay between the two wavelengths, and they suggested their potential in determining phase differences between the even- and odd-parity continuum wave functions.

This work was followed by Nakajima's theory paper [12], in which he proposed a technique for measuring the phase difference between the even- and odd-parity partial waves. The technique was also based on the interference between one- and two-photon ionization transitions using either appropriate polarizations of the ionizing laser fields or a polarized initial state. This proposal triggered further work by Elliott and coworkers. A year later, they developed an experimental technique similar to that proposed by Nakajima. They were able to carry out measurements of the phase difference between the even- and odd-parity partial waves for the first time.

Interference experiments based on simultaneous one- and two-photon ionization experienced a renaissance with interest to demonstrate the longitudinal coherence properties of free-electron laser (FEL) radiation at FERMI located in Trieste (Italy) [13, 14]. A series of experiments were performed with neon starting from a $2p$ orbital. After demonstrating the left-right asymmetry control of the PADs, experiments followed, which allowed the extraction of several photoionization parameters. In particular, by measuring the PADs as a function of the relative phase between the two harmonics and fitting them with a series of Legendre polynomials, the even- and odd-order β parameters could be determined. The β parameters, in turn, enabled the extraction of the phase difference between the even- and odd-parity continuum wave functions. In addition, the FERMI group performed measurements of the emission-angle-dependent phase shifts of the modulated photoelectron signal as previously observed by Elliott and coworkers in the optical domain. By measuring these phase shifts at three different photon energies, they determined the difference between the photoemission delays resulting from one-photon and two-photon ionization. Thereby, this method establishes a complementary technique to the well-known RABBITT (reconstruction of attosecond beating by interference of two-photon transitions) technique [15, 16], which is extensively used for measuring photoionization delays in various targets [17]. In RABBITT, however, interference occurs between two different two-photon transitions.

In this thesis, we present the left-right asymmetry control of the PADs of ground-state lithium with respect to the relative phase of the two-color laser field of 780/390 nm radiation. This work complements existing demonstrations of left-right asymmetry control. In our experiment, however, in contrast to all previous reports, where the interference occurred between one- and two-photon ionization transitions, all induced ionization pathways include multiphoton absorption. Because of the many intermediate resonances with long-living Rydberg states, our work explores their effect on the photoelectron spectra in the case of temporally overlapping and non-overlapping two-color pulses. In particular, we examine differences between the photoelectron spectra measured and calculated when the fundamental pulse advances the SH pulse and vice versa.

This thesis is organized as follows. Chapter 1 covers the theoretical background required to understand the basic principles of the relevant strong-field ionization phenomena, particularly the MPI of atoms. Chapter 2 describes our experimental apparatus,

including the Reaction Microscope and femtosecond laser system. Chapter 3 introduces the Legendre polynomial basis sets for lithium ground-state ionization with single-color and two-color laser fields. After this, energy shifts of the ground and the relevant Rydberg states due to the AC Stark effect are considered. The chapter finishes with a detailed description of our optical setup for generating the two-color laser field. Chapter 4 is devoted to the presentation and discussion of our results. First, we study the differences between the photoelectron spectra obtained when the fundamental pulse is advancing the SH pulse and vice versa in the cases of overlapping and non-overlapping two-color pulses. After this, we present measurements of the left-right asymmetry control of the PAD of ground-state lithium with subwavelength accuracy. All measurements are compared with theoretical predictions. The latter were obtained by solving the time-dependent Schrödinger equation in the single-active electron approximation with the experimentally determined laser fields. Chapter 5 presents the conclusions of this work and an outlook for possible future studies. Finally, Appendix A describes an introductory project that was carried out at the beginning of the work for this thesis. It deals with the preparation and subsequent ionization of the 2^2P excited state of lithium.

1. Theoretical background

This chapter gives a brief overview of strong-field ionization of atoms. Section 1.1 introduces the relevant interaction regimes in the process. Section 1.2 presents a mathematical description of multiphoton ionization (MPI). In Section 1.3, we introduce the basis set of Legendre polynomials constituting the photoelectron angular distributions (PADs) for Li.

1.1. Strong-field ionization

The simplest photoionization process is single-photon ionization. In this case, the energy of the photon must be either equal to or larger than the binding energy of the electron to be ejected. An example of single-photon ionization is the photoeffect [18], which was observed a long time before the invention of the laser. Single-photon ionization does not require strong-field radiation.

In strong-field ionization, the electric field strength of the laser is comparable to the electric field produced by an electron inside the atom. In the Bohr model of the hydrogen atom, the electron moving in the first Bohr orbit of radius 5.3×10^{-11} m creates an intra-atomic electric field of 5×10^{9} V/cm, which corresponds to an electric field intensity of 3.5×10^{16} W/cm^2.

The ionization of an atom by a strong laser field can occur via MPI or tunneling ionization. The two interaction regimes can be distinguished by means of the Keldysh parameter γ_K [19, 20] given by

$$\gamma_\mathrm{K} = \sqrt{\frac{IP}{2U_\mathrm{p}}}, \tag{1.1}$$

where IP is the ionization potential of the bound electron and U_p is the ponderomotive potential of an electron in a laser field. The ponderomotive potential is the average kinetic energy of the quivering motion of a free electron in a laser field with intensity I and angular frequency ω. It is defined by

$$U_\mathrm{p} = \frac{I}{4\omega^2}. \tag{1.2}$$

If the ponderomotive energy is larger than half of the ionization potential of the bound electron ($\gamma_\mathrm{K} < 1$), then tunneling ionization dominates. In this case, the laser field can drive the electron away from its parent ion. If, on the contrary, the ponderomotive energy is small compared to the electron binding energy ($\gamma_\mathrm{K} > 1$), then MPI dominates. In other words, tunneling ionization can be understood in the picture of the driving laser field, MPI in terms of photon absorption. Therefore, tunneling ionization is often

described in a semi-classical picture, where the atom is treated quantum-mechanically while the electric field is assumed to be classical. In contrast, MPI requires a fully quantum-mechanical description (see Section 1.2). Note, however, that the Keldysh parameter can clearly distinguish between the two regimes only in its limiting values, i.e., $\gamma_K \ll 1$ for tunneling ionization and $\gamma_K \gg 1$ for MPI. For example, if $\gamma_K \approx 1$, both pictures need to be accounted for simultaneously.

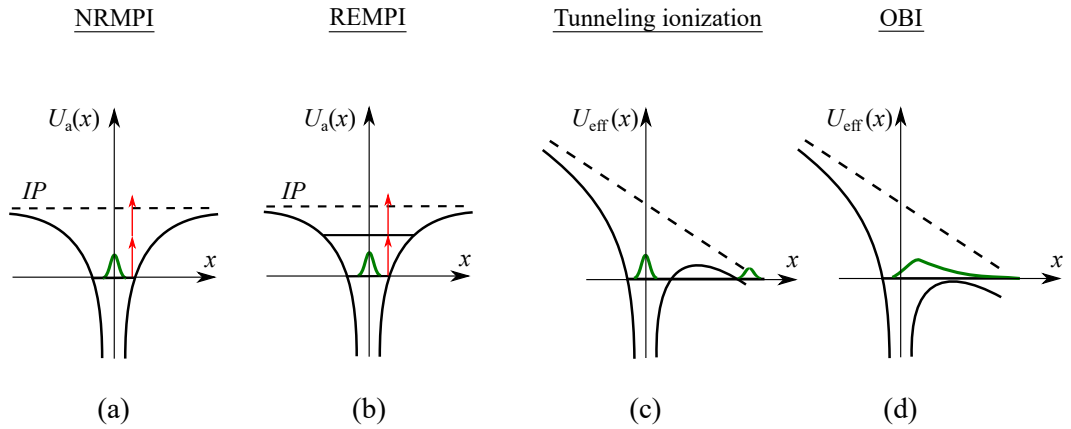

Figure 1.1.: Coulomb potentials of atoms (solid black lines) and sketches of the electron's wavefunction (green) in different interaction regimes with intense laser fields. (a) NRMPI: Non-Resonant Multiphoton Ionization. (b) REMPI: Resonance-Enhanced Multiphoton Ionization. (c) Tunneling ionization. (d) OBI: Over-the-Barrier Ionization.

Figure 1.1 illustrates Coulomb potentials of atoms in different strong-field interaction regimes. Non-Resonant Multiphoton Ionization (NRMPI) is illustrated in (a). In contrast to Resonance-Enhanced Multiphoton Ionization (REMPI) shown in (b), NRMPI does not include intermediate resonances with bound atomic states. In (c), the combination of the atomic Coulomb potential U_a and the potential of the laser field U_l generates the effective potential U_{eff} given as

$$\begin{aligned} U_{eff}(x,t) &= U_a(x) + U_l(t) \\ &= -\frac{Z}{x} - xE(t) \\ &= -\frac{Z}{x} - xE_0(t)\sin(\omega t + \phi), \end{aligned} \tag{1.3}$$

where Z is the number of protons in the atom, and $E(t)$ is the electric field of the linearly-polarized laser pulse with envelope $E_0(t)$ and carrier frequency ω, respectively. The carrier-envelope phase ϕ can have an effect in few-cycle pulses, but it is not needed for the illustration. The effective potential forms a potential barrier, which the bound electron can tunnel through. By further increasing the driving field intensity, the height of the potential barrier can be suppressed below the energy of the bound electron. In this case, the electron escapes the Coulomb potential. This phenomenon, called Over-the-Barrier Ionization (OBI), is illustrated in (d).

In this thesis, we investigate the MPI regime. Its mathematical description is presented in the next section.

1.2. Multiphoton ionization

Atomic units (e = m_e = $\hbar$ = 1) are used in this section unless otherwise stated. The N-photon ionization rate $R(\omega)$ of an atom scales according to

$$R(\omega) = \sigma_N(\omega)\Phi^N = \kappa_N(\omega)I^N, \tag{1.4}$$

where σ_N and κ_N are generalized cross-sections of dimensions $[\sigma_N] = \mathrm{cm}^{2N}\mathrm{s}^{N-1}$ and $[\kappa_N] = \mathrm{W}^{-N}\mathrm{cm}^{2N}\mathrm{s}^{-1}$, Φ is the photon flux, and I is the intensity of the laser field. The generalized cross-section $\sigma_N(\omega)$ can be derived from time-dependent perturbation theory. Here, we only present the final result of this derivation. Details can be found, for example, in [21, 22].

$\sigma_N(\omega)$ is the squared modulus of the N^{th}-order transition matrix element $M^{(N)}(\vec{k};\omega)$ between the initial state $|i\rangle$ and the final continuum state $|\vec{k}_N\rangle$, i.e.,

$$\sigma_N(\omega) \propto \left|M^{(N)}(\vec{k}_N;\omega)\right|^2 \tag{1.5}$$

with

$$M^{(N)}(\vec{k}_N;\omega) \propto \lim_{\varepsilon\to 0^+} \oint\!\!\!\!\!\!\int_{\nu_{N-1}} \cdots \oint\!\!\!\!\!\!\int_{\nu_2} \oint\!\!\!\!\!\!\int_{\nu_1} \frac{\langle\vec{k}_N|\, z\,|\nu_{N-1}\rangle \ldots \langle\nu_2|\, z\,|\nu_1\rangle\langle\nu_1|\, z\,|i\rangle}{(\epsilon_{N-1}-\epsilon_{\nu_{N-1}}+\mathrm{i}\varepsilon)\ldots(\epsilon_1-\epsilon_{\nu_1}+\mathrm{i}\varepsilon)}. \tag{1.6}$$

Here z is the electric dipole operator, and $\epsilon_n = \epsilon_i + n\omega$, where ϵ_i is the initial state energy. The symbol $\oint\!\!\!\!\!\!\int$ indicates a sum of the index ν_n over all bound states and an integral over all continuum states of the target. Finally, $\lim_{\varepsilon\to 0^+}$ provides a prescription of how to go around poles in the complex plane in case of an intermediate resonance (see below). While Eq. (1.4) is useful for the general description of the process, in particular the scaling with the power of the field intensity, Eq. (1.6) is not very practical in actual numerical calculations. Instead, one often solves the time-dependent Schrödinger equation directly and obtains the ionization probability by projecting on the final continuum state.

1.2.1. Resonance-Enhanced Multiphoton Ionization

In the case of intermediate resonances with atomic bound states (see Figure 1.2 (b) for the REMPI process), the denominator of Eq. (1.6) vanishes (this is the reason for the $\lim_{\varepsilon\to 0^+}$ modification). This significantly enhances the ionization rate compared to the NRMPI process illustrated in Figure 1.2 (a), where only virtual intermediate states are involved. The resonant atomic states provide the dominant contributions to the sum. Hence, they are often the only terms kept in approximate calculations of the N^{th}-order matrix element.

In general, one can think of REMPI as a two-step process, where the excitation of an intermediate bound state with m photons is followed by ionization with n photons [23]. If the intermediate resonance state is a high-lying Rydberg state, absorption of a single additional photon might be sufficient to reach the continuum [24].

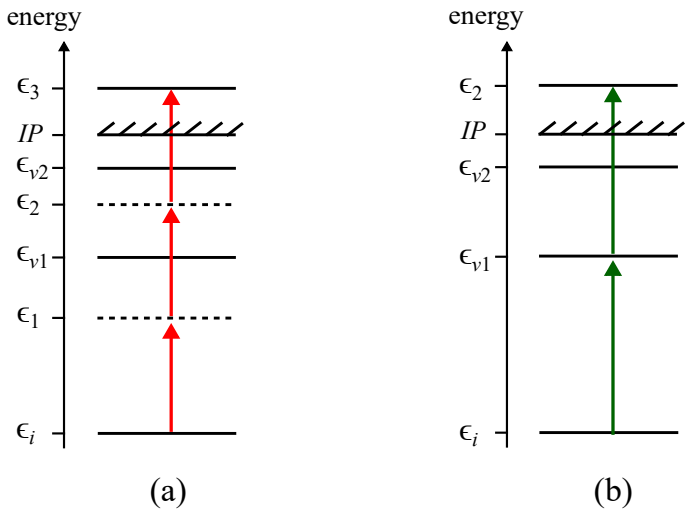

Figure 1.2.: Schematics of the NRMPI (a) and REMPI (b) processes. The dashed lines represent virtual states.

1.2.2. Above-Threshold Ionization

Above-Threshold Ionization (ATI) is a feature in MPI, where an electron absorbs more photons than required to overcome the ionization threshold [25]. Therefore, the energy spacing between the ATI peaks corresponds to the single photon energy as illustrated in Figure 1.3 (a).

Whereas, in general, absorption of photons by a free electron is not possible since it would violate energy and/or momentum conservation, ATI can take place due to the Coulomb interaction with the parent ion that acts as a third body. The number of excited ATI photolines increases with the intensity of the ionizing laser field. Their peak intensities, in turn, decrease with increasing order of the ATI photoline.

1.2.3. AC Stark shifts

In a strong laser field, the energies of the atomic bound states are shifted due to the AC Stark effect. In the following, we briefly summarize the approximations for calculating the AC Stark shifts of deeply bound and high-lying Rydberg states, which are taken from [27].

In second-order perturbation theory, the energy shift of a state $|m\rangle$ with an unperturbed energy E_m is given by

$$\Delta E_m = \left(\frac{E_0}{2\omega}\right)^2 \sum_n \left[|\langle n|\,\vec{p}\cdot\hat{e}\,|m\rangle|^2 \times \left(\frac{1}{E_m - E_n - \omega} + \frac{1}{E_m - E_n + \omega}\right)\right], \tag{1.7}$$

where E_0 is the electric field amplitude, $\vec{p}$ is the dipole operator, $\hat{e}$ is the polarization unit vector of the laser field, and $|n\rangle$ represents a complete set of states of the unperturbed atomic Hamiltonian.

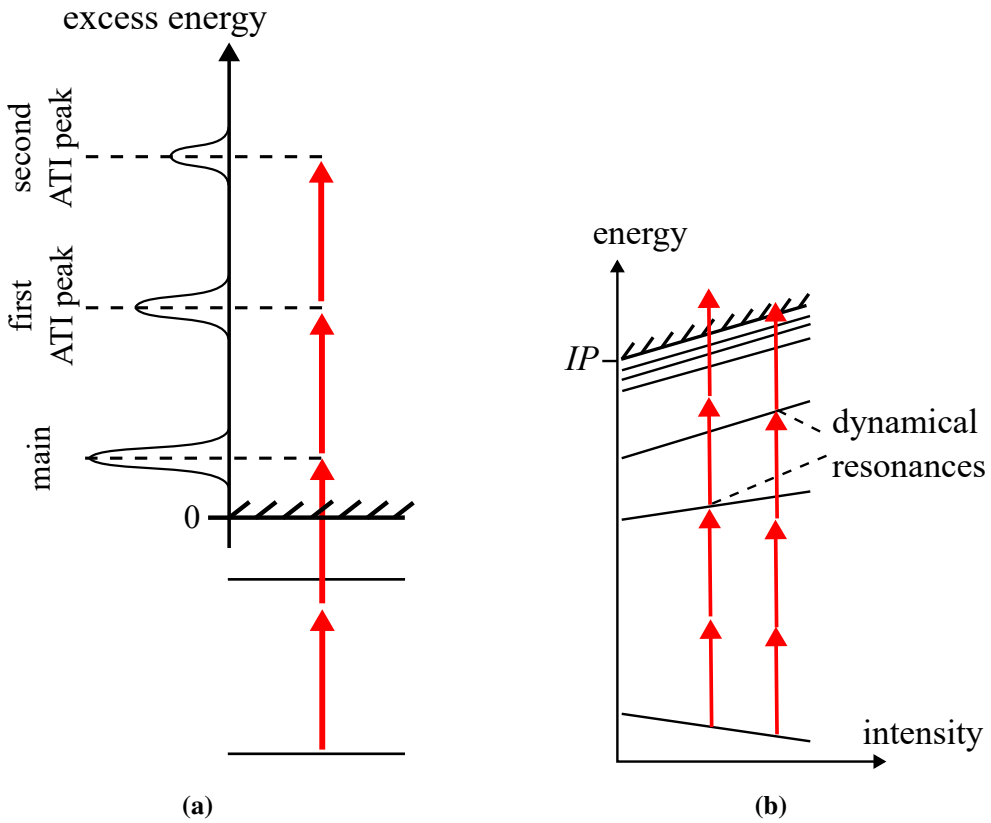

Figure 1.3.: Schematic diagrams illustrating (a) the peaks of the main photoline as well as the first and second ATI photolines; (b) the dynamical resonances. The figure is adapted from [26].

The energy shift of the ground state, ΔE_g, is found by making a low-frequency approximation, i.e., $|E_g - E_n| \gg \omega$ for all $|n\rangle$. Then, ΔE_g can be expanded in a power series of $\omega/(E_g - E_n)$. The first two terms are

$$\Delta E_g = -\frac{E_0^2}{4\omega^2} - \frac{1}{2}\alpha E_0^2. \tag{1.8}$$

The first term is the negative of the ponderomotive potential, while the second term is equivalent to a DC Stark effect. Here, $\alpha = \sum_n \left|\langle n|\vec{p}\cdot\hat{e}\,|m\rangle\right|^2/(E_n - E_g)$ is the ground-state polarizability. Therefore, the AC Stark shift of the ground state is proportional to the laser field intensity I via the relation $E_0^2 = 2I/(\epsilon_0 c)$, where ϵ_0 is the electric permittivity and c is the speed of light. Since $\alpha > 0$, the AC Stark shift of the ground state is negative.

The energy shift of the high-lying Rydberg states $|R\rangle$ can be found by employing a high-frequency approximation for these states, i.e., $\omega \gg |E_n - E_R|$ for all $|n\rangle$. The first term in the expansion of Eq. (1.8) into a power series vanishes, and the second term is negligible. Thus, the high-lying states experience the same energy shift as the continuum, which is that of the ponderomotive shift.

To summarize, the AC Stark effect lowers the energy of the ground state, whereas the energy of the high-lying states is shifted upwards by the ponderomotive potential.

The intensity-dependent energy level shifts discussed above at certain intensities can make transitions between the ground state and one of the high-lying states resonant with the energy of an integer number of photons. These are called dynamical resonances. From there, to overcome the ionization threshold, absorption of a single photon is required. Therefore, dynamical resonances with intermediate states lead to a significant enhancement of the ionization rate. Figure 1.3 (b) illustrates the onset of dynamical resonances with linear changes in the energy shifts of the ground state and the high-lying states as a function of the laser intensity.

1.3. Decomposition of the PAD in terms of Legendre polynomials

For a linearly polarized laser field, as well as a multi-color field with all components polarized along the same direction, and an unpolarized initial state, the problem exhibits cylindrical symmetry. This is the case for all setups used in this thesis. Hence, the PAD depends only on the Legendre polynomials $P_l(\theta)$. Specifically, the differential cross-section can be expressed as

$$\frac{d\sigma}{d\theta} \propto \left| \sum_{l=0}^{l_{\max}} c_l \, \mathrm{e}^{\mathrm{i}\eta_l} \sqrt{2l+1} P_l(\theta) \right|^2 = \frac{\sigma_{\mathrm{tot}}}{4\pi} \sum_{\lambda=0}^{2l_{\max}} [1 + \beta_\lambda P_\lambda(\theta)]. \tag{1.9}$$

The c_l are complex coefficients proportional to the transition matrix elements, and η_l is the phaseshift of the partial wave with orbital angular momentum l. In our case, it is comprised of the Coulomb phase plus a potential-scattering phase that accounts for deviations from a pure Coulomb potential with asymptotic charge $Z_{\mathrm{asym}} = 1$ due to the short-range screening of the full nuclear charge of Li ($Z = 3$) by the $(1s^2)$ core of Li^+. Furthermore, $l_{\max}$ is the maximum number of photons involved in the process, σ_{tot} is the angle-integrated cross-section, and the β_λ are asymmetry parameters. If the parity of the final state is well-defined, only even values of λ are allowed, and the angular distribution is symmetric with respect to $\theta = 90°$. If that is not the case, as in the two-color setups employed in this work, this symmetry can be broken due to contributions from odd values of λ. Examples of such angular distributions will be shown in Chapters 3 and 4.

2. Experimental Apparatus

This chapter gives an overview of the experimental apparatus employed within the framework of this thesis. In Section 2.1, we describe the basic working principle of the Reaction Microscope (ReMi), i.e., a device used in recoil-ion momentum spectroscopy. Besides its arrangement, we consider the reconstruction of the vector momenta of the detected charged particles emerging from the ionization reaction. In Section 2.2, we describe our femtosecond laser system.

2.1. Reaction Microscope

We start this section with a general description of the ReMi arrangement, followed by a description of its detectors. We conclude by explaining the reconstruction of the vector momenta of the detected charged fragments.

2.1.1. Setup

The ReMi is a standard device used in recoil-ion momentum spectroscopy [28–32]. Examples of ReMis are schematically shown in Figure 2.1. The ReMi's main components are the spectrometer and the position- and time-sensitive detectors. The spectrometer consists of a stack of electrodes, which generate a homogeneous electric extraction field along the spectrometer axis for guiding the electrons and ions in opposite directions toward their detectors (see Figure 2.3 (b)). More details on the geometry of the spectrometer are discussed below. In addition, a pair of Helmholtz coils generates a homogeneous magnetic extraction field along the spectrometer axis to confine the electron trajectories by subjecting them to a cyclotron motion. The extraction fields, therefore, determine the trajectories of the charged fragments, and at the appropriate field strengths, a 4π detection efficiency for both ions and electrons can be accomplished. This, in turn, allows performing measurements of ions and electrons in coincidence.

The two examples of ReMis shown differ in their targets – a supersonic gas jet in (a) and a sample of magneto-optically trapped (MOT) atoms in (b). The latter apparatus is called a MOTReMi. Recently, photoionization experiments were also carried out with optically trapped atoms [33–36]. Typically, gas jets serve as a cold target for experiments with inert gases, e.g., He, Ar, or H_2. In contrast, optically trapped samples are used in experiments with alkali metal atoms due to the well-elaborated laser cooling and trapping techniques involving alkali metal gas vapors.

In our laboratory, we have a MOTReMi setup shown in (b). During the work reported in a previous PhD thesis from this laboratory, the transfer of MOT atoms of ^{6}Li into

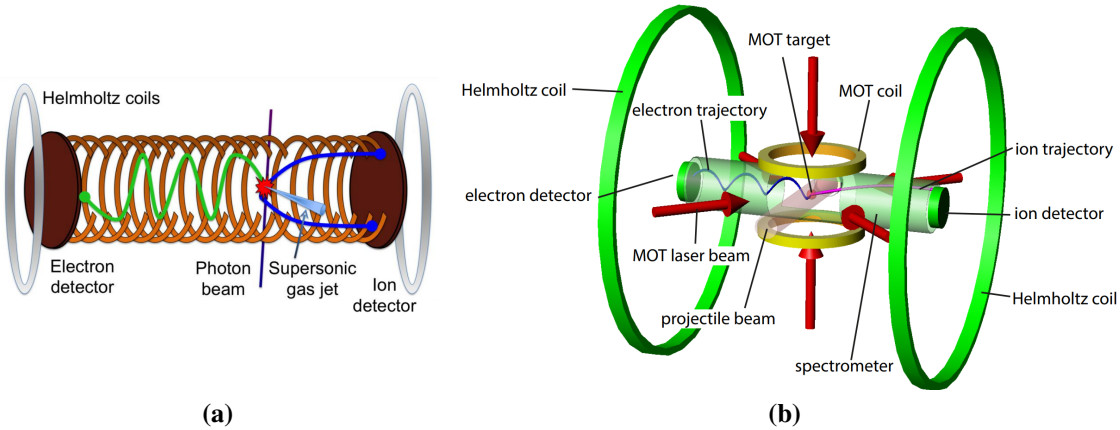

Figure 2.1.: Reaction Microscopes with (a) a supersonic gas jet and (b) magneto-optically trapped atoms as a target. Figure (a) is taken from [37] and (b) from [38].

the optical dipole trap was accomplished. A series of experiments followed, including the ionization of optically trapped ground-state lithium atoms [35] and photoassociated lithium dimers Li_2 [36] by femtosecond laser pulses. On the other hand, the experiments presented in Chapter 4 of the present thesis were performed with a hot lithium atomic beam. Furthermore, a target of lithium atoms trapped in an optical dipole trap was used in the experiments presented in Appendix A.

In addition to the studies of the photoionization processes [30], ReMis are also employed to investigate the electron and ion collisions [30]. For the photoionization studies, femtosecond lasers [39], high-order harmonic radiation sources [40], and free-electron lasers [41] have been used as projectile beams.

2.1.2. Detectors

To detect ions and electrons, position- and time-sensitive detectors are employed. Each such detector is an assembly of a microchannel-plate (MCP) detector [42] and a delay-line anode [43] as illustrated in Figure 2.2 (a).

The weakly charged fragment first hits the MCP detector. The MCP detector is displayed in more detail in Figure 2.2 (b). A high voltage is applied between its front and back sides. The charged fragment impact with the MCP detector causes a slight drop in the applied high voltage. This drop can be read out by the capacitor and determines the arrival time of the charged fragment at the detector, i.e., its Time-of-Flight (TOF). Each microchannel of the MCP detector with a diameter of ~10 μm acts as an electron multiplier. The accelerated charged fragment, after multiple collisions with the walls of the microchannel, produces an electron cloud at the backside of the MCP detector. The electron cloud then hits the position-sensitive delay-line anode.

The working principle of the delay-line anode is illustrated in Figure 2.2 (c). The impinging electron cloud creates a charge distribution within neighboring windings of the anode, which travels in opposite directions and creates voltage spikes at both ends

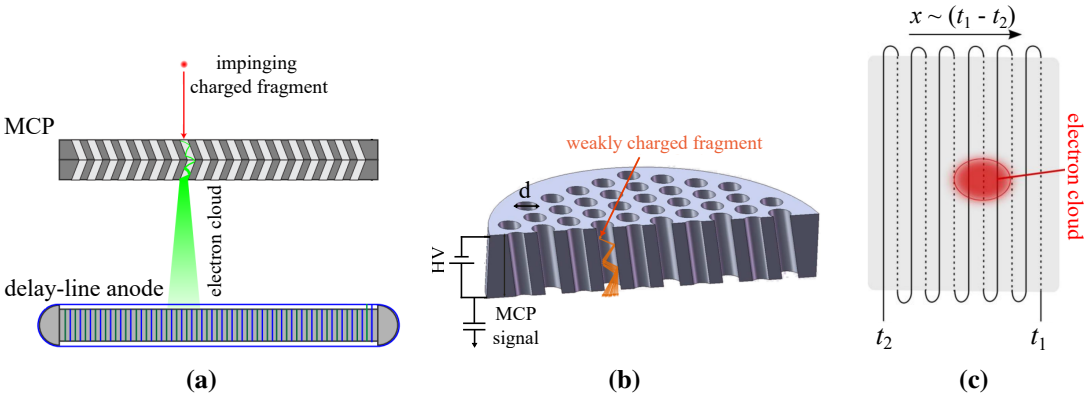

Figure 2.2.: (a) Detector assembly of an MCP and a delay-line anode. (b) MCP detector. (c) Delay-line anode. Panels (a) and (c) were adapted from [38] and Panel (b) from [44].

of the wire. The cloud position on the delay-line anode is proportional to the time difference between the signals detected at the wire ends. To determine both the x and the y coordinates of the electron cloud on the detector, either two orthogonal layers of the delay line anode or three hexagonal layers are usually employed. We use a delay-line anode with two orthogonal layers for detecting the recoil-ions and three hexagonal layers for detecting the electrons. More details on the hexagonal delay line detectors can be found in [45].

2.1.3. Momentum reconstruction

Below we present the momentum reconstruction of the charged particles from the measurements of their TOF and radial positions. The spectrometer exhibits cylindrical symmetry. This allows us to consider the reconstruction of the longitudinal momentum, p_z, and the transversal momentum, p_{tr}, independently. Although in this thesis we only studied momentum spectra of electrons, relations describing the momentum reconstruction of both the ions and electrons are given below.

2.1.3.1. Longitudinal momentum

Before proceeding with the formulae used for the longitudinal momentum reconstruction, let us first have a closer look at the geometry of the spectrometer shown in Figure 2.3 (b). For the sake of simplicity, we only consider the ion side of the spectrometer. In particular, one distinguishes between the acceleration region over a distance L_a and the drift region over a distance L_d. Typically, $L_d = 2L_a$, which corresponds to the McLaren configuration. This configuration accounts for an extended reaction volume, which leads to a time jitter between the charged particles originating from different points within the reaction volume [46]. In the acceleration region, the charged particles are accelerated and gain enough kinetic energy to reach the detector. The potential applied to the drift region is usually the same as that of the last electrode of the acceleration region. Therefore, in the drift region, the charged particle moves at a constant velocity.

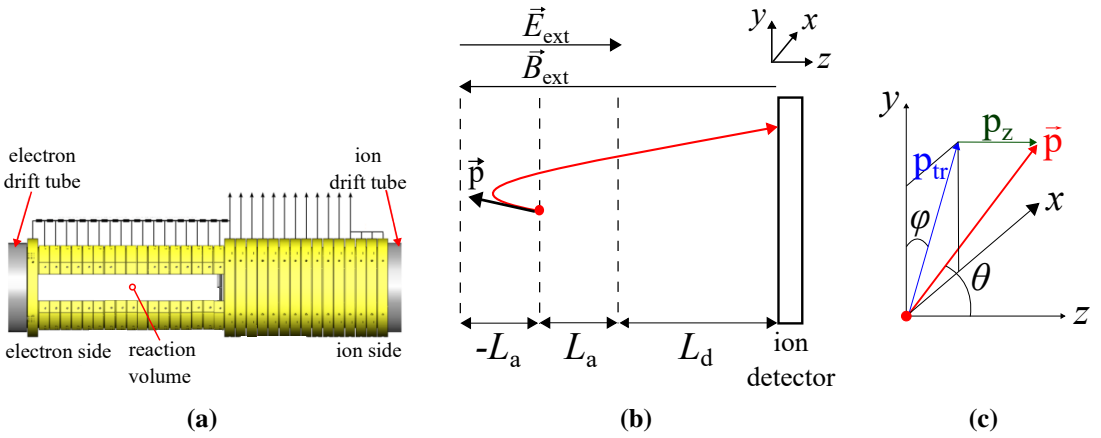

Figure 2.3.: (a) Technical drawing of the arrangement of electrodes of our spectrometer. (b) Schematic drawing of the geometry of the ion side of the spectrometer indicating the acceleration L_a and the drift L_d regions. (c) Schematic drawing defining the polar θ and azimuthal φ angles of the vector momentum $\vec{p}$ of the charged particle.

To summarize, the longitudinal motion of the charged particles is determined by a constant acceleration in the acceleration region and a constant motion in the drift region. The TOF, t_{TOF}, of a charged particle with mass m, charge q, and initial longitudinal momentum p_z is given by

$$t_{TOF}(p_z) = m \cdot \left(\frac{2L_a}{\sqrt{p_z^2 + 2mqU} \pm p_z} + \frac{L_d}{\sqrt{p_z^2 + 2mqU}} \right), \tag{2.1}$$

with

$$U = \int_0^{L_a} -E_{ext} dz = -E_{ext} \cdot L_a, \tag{2.2}$$

where U is the potential across the distance L_a and $E_{ext} = |\vec{E}_{ext}|$ is the electric extraction field. In the denominator of the first term, '+' stands for the electrons and '−' for the ions.

The initial momentum p_z for a given t_{TOF} can be found numerically using Newton's method. Its implementation is described in the Appendix of [47].

2.1.3.2. Transversal momentum

The transverse motion of the charged particle depends only on the magnetic extraction field $\vec{B}_{ext}$ along the spectrometer axis but not on $\vec{E}_{ext}$. However, in our experiment, the ions are hardly affected by the magnetic extraction field due to their much larger mass compared to that of the electrons. The large-mass limit of the particle will be discussed explicitly below. Therefore, the following discussion about determining p_{tr} refers mainly to the electrons.

$\vec{B}_{ext}$ subjects the particle with mass m and charge q to a cyclotron motion with the angular frequency ω_c given by

$$\omega_c = \frac{|q|B_{ext}}{m}, \tag{2.3}$$

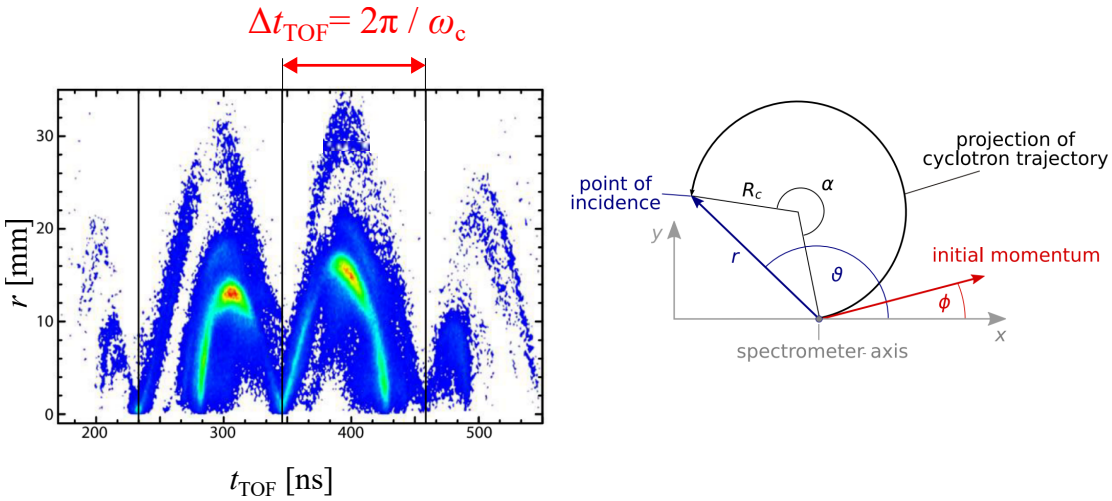

(a) **(b)**

Figure 2.4.: (a) Spectrum of the radial position r of the electron versus its TOF. (b) Projection of the cyclotron trajectory on the detector with all relevant angles for understanding the calculation of the cyclotron radius R_c. Figure (a) is taken from [38] and (b) from [47].

where $B_{ext} = |\vec{B}_{ext}|$. Experimentally, ω_c can be determined from the distribution of the radial position r of the electrons as a function of their TOF. An example of such a distribution is shown in Figure 2.4 (a).

The radius of the cyclotron motion R_c is proportional to the initial transversal momentum $p_{tr} = \sqrt{p_x^2 + p_y^2}$. It is given by

$$R_c = \frac{p_{tr}}{\omega_c \cdot m}. \tag{2.4}$$

Since we do not know the axis of the cyclotron trajectory, we cannot measure R_c directly. Instead, we can calculate it from the relation

$$R_c = \frac{r}{2|\sin(\alpha/2)|}, \tag{2.5}$$

where $\alpha = \omega_c \cdot t_{TOF}$. This relation is derived from the geometrical considerations of projecting the cyclotron trajectory onto the detector plane, as illustrated in Figure 2.3 (b). From Eqs. (2.4) and (2.5), the initial transversal momentum p_{tr} is obtained as

$$p_{tr} = \frac{\omega_c \cdot m \cdot r}{2|\sin(\omega_c t_{TOF}/2)|}. \tag{2.6}$$

Finally, we obtain the limit of Eq. (2.6) in the case of low cyclotron frequencies ω_c, i.e., for a weak magnetic extraction field or a large mass of the particle. With $\sin(x) \approx x$ for small x, we find

$$\lim_{\omega_c \to 0} p_{tr} = \frac{r \cdot m}{t_{TOF}}. \tag{2.7}$$

This expression is commonly used to calculate the transverse momentum of ions.

2.2. Femtosecond laser system

The femtolaser system used in the experiments presented in this thesis is the FEMTOPOWER COMPACT PRO from FEMTOLASERS. Its layout is shown in Figure 2.5. It consists of three main parts.

The oscillator produces a pulse train at the pulse repetition rate of 80 MHz with a pulse energy of ~5 nJ. The oscillator output is amplified using the well-known Chirped Pulse Amplification (CPA) technique [48]. The CPA technique requires stretching the oscillator output pulses before their amplification to prevent damage to the amplifying Ti: Sapphire crystal at high pulse peak intensities. Therefore, before entering the amplifier part, the pulses of the oscillator pulse train are stretched by a pulse stretcher. The latter introduces a strong dispersion, i.e., a chirp, on the pulse spectrum, which results in an increase of the pulse duration by several orders of magnitude.

The amplifier working principle is based on multipass amplification. Specifically, the seed beam of the stretched pulses passes through the amplifying Ti:Sapphire crystal a total of nine times. The Ti:Sapphire crystal is pumped by a Q-switched Nd:YAG pump laser at a pulse repetition rate of 4 kHz. After the 4^{th} pass, the amplified beam goes through the Pockels cell. The latter selects the most intense pulse under the pulse envelope determined by the amplifier pump laser with a temporal width of hundreds of ns (see Figure 2.6). The Pockels cell rotates the polarization of the most intense pulse to be orthogonal to the other pulses. In this way, after passing through the polarizing beam-splitter cube implemented behind the Pockels cell, only the most intense pulse is transmitted and subsequently amplified via the 5^{th} to 9^{th} passes.

Finally, the amplified stretched pulse train is compressed again by the prism compres-

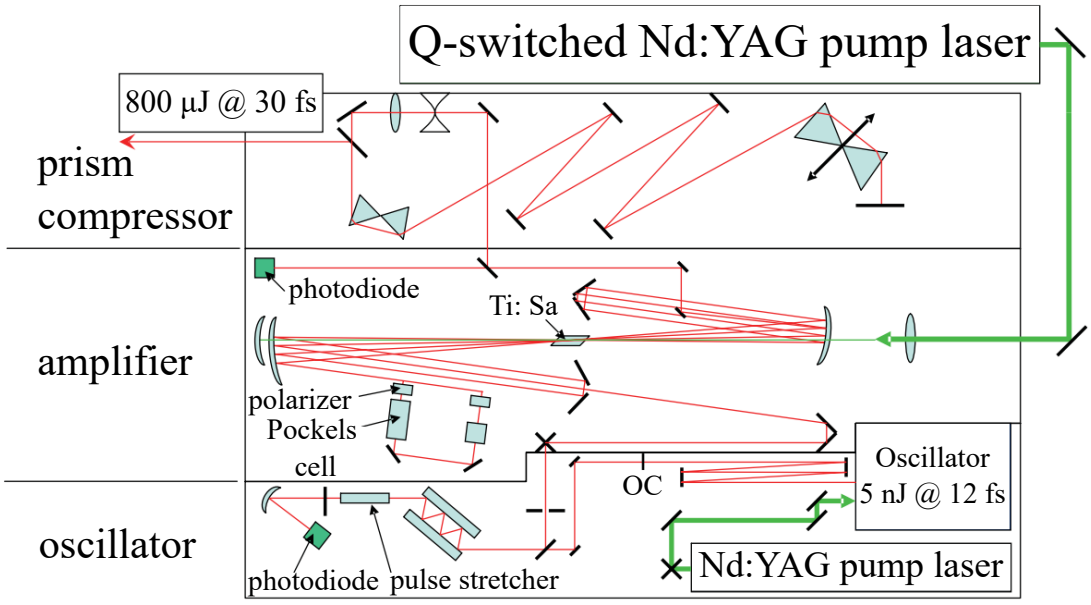

Figure 2.5.: Layout of our femtolaser system. The figure is adapted from [26].

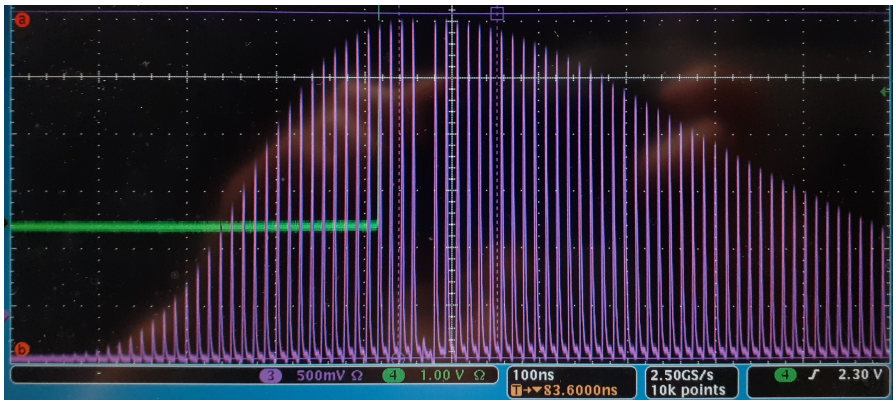

Figure 2.6.: Photograph of the oscilloscope screen showing the photodiode signal of the 80 mHz pulse train after passing through the Pockels cell. The pulses of the amplifier pump laser determine the signal envelope. The photodiode detects the reflected part from the polarizing beam-splitter cube implemented right behind the Pockels cell. Therefore, the most intense pulse under the envelope selected here for further amplification appears as a minimum in the pulse train.

sor. Our femtolaser system can generate pulses with energies up to 800 μJ with a FWHM pulse duration of ~30 fs.

2.2.1. Pulse characterization

For characterizing the pulses of the femtosecond laser directly at its output and those used in the experiments described in Chapter 4, we applied the self-calibrating dispersion-scan technique, which is described in detail in [49]. In contrast to the conventional dispersion scan technique used to characterize few-cycle pulses [50], the self-calibrating dispersion scan technique can also be applied to the multi-cycle pulses. The retrieval of the pulse characteristics by this technique is based on an algorithm that reproduces the measured trace of the second-harmonic spectra as a function of the dispersion introduced by the prism compressor. Such a pulse retrieval is commercially offered by Prof. Benjamin Alonso from the University of Salamanca.

Figure 2.7 shows the results of his pulse retrieval algorithm, where $S(\lambda)$ and $\phi(\lambda)$ denote the spectral intensity and the spectral phase, respectively, and $I(t)$ and $\phi(t)$ the temporal intensity and the phase, respectively. For the pulses at the femtolaser output and those used in the experiment, the spectral phase appears flat across the pulse spectrum. This means that the pulse is well compressed, and the contributions from the second and higher-order dispersion terms are negligible. The temporal intensity profiles of the pulses yield durations at their FWHM of 37.3 fs and 42.5 fs for the output and the experimental pulses, respectively. Nevertheless, even though the algorithm works very well, measuring the dispersion trace of the second-harmonic spectra is a challenging task. Therefore, deviations of the pulse characteristics from those retrieved by the algorithm are possible.

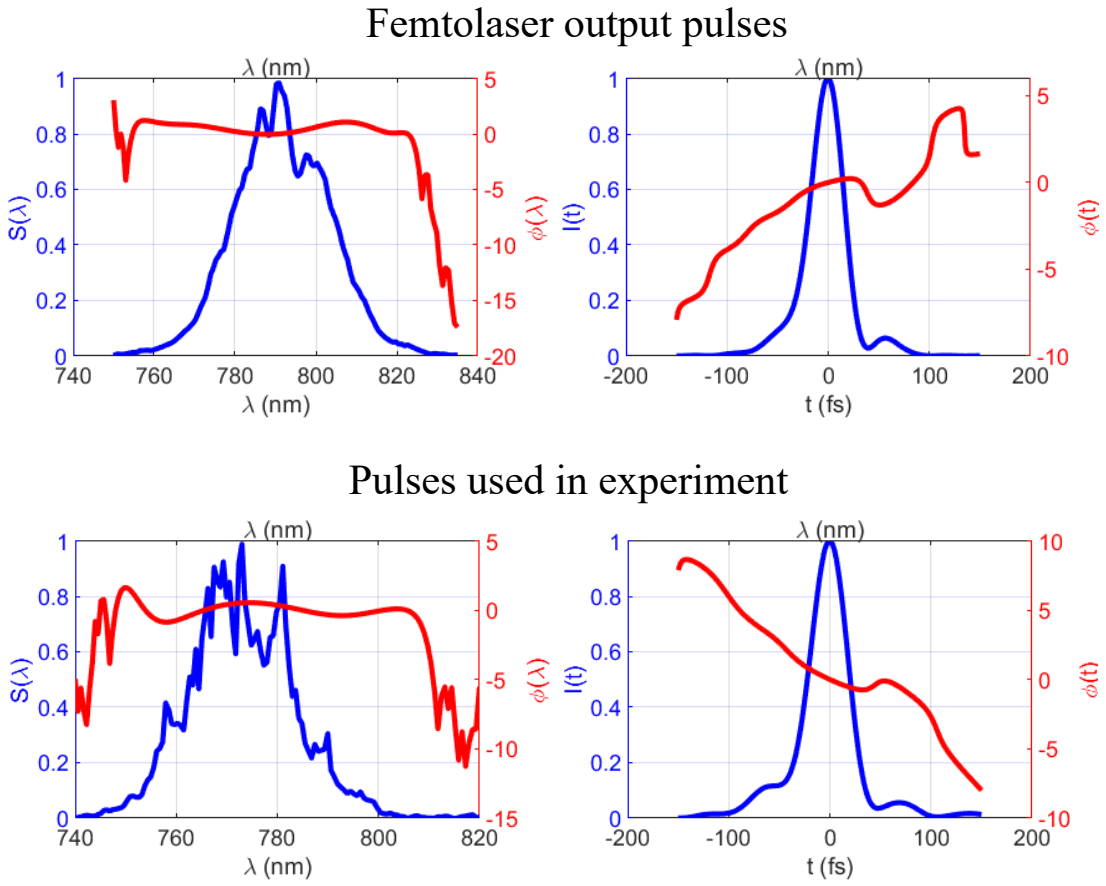

Figure 2.7.: Retrieved spectral intensity $S(\lambda)$ and phase $\phi(\lambda)$ as well as the temporal intensity $I(t)$ and phase $\phi(t)$ by applying a self-calibrating dispersion scan technique for the pulses directly at the femtolaser output and those used in the experiment.

3. Two-color ionization of ^{6}Li: Basics and Setup

This chapter examines the two-color multiphoton ionization (MPI) of ^{6}Li by a bichromatic laser field consisting of 780/390 nm radiation. Section 3.1 presents basis sets of Legendre polynomials for single-color and two-color ionization. We describe the effect of controlling the relative optical phase Φ between the two-color pulses on the interference between partial waves of different parities and angular momenta. In Section 3.2, energy shifts of the ground and Rydberg states of ^{6}Li due to the AC Stark effect are considered. Section 3.3 describes in detail our two-color optical setup.

3.1. Basis set of Legendre polynomials constituting the PADs for Li

In this section, we present basis sets of Legendre polynomials describing the partial waves of the ejected photoelectrons after MPI with linearly polarized single-color and two-color pulses.

3.1.1. Single-color multiphoton ionization

Ionization pathways induced by only the fundamental or second-harmonic (SH) pulses leading to the excitation of the main photoline are shown in Figures 3.1 (a) and (b), respectively. In the case of ionization with single-color pulses, the angular-momentum selection rules ($\Delta l = \pm 1$) restrict the parity of the partial waves in the final state to either even or odd. In (a), ionization by the fundamental pulses requires absorption of at least four photons, which takes place via intermediate resonances with Rydberg states. In (b), ionization by SH pulses requires absorption of at least two photons. Therefore, the partial waves emitted are of even parity in both cases.

Figure 3.2 (a) depicts polar plots of squared Legendre polynomials $P_l(\theta)^2$ describing the angular part of the partial waves constituting the main photoline excited by either fundamental or SH pulses. Figures 3.2 (b1, b2) show the measured 2D momentum distributions of the main photoline displaying photoelectron transversal momenta, p_{tr}, versus their longitudinal momenta, p_z, which result from single-color ionization by either fundamental or SH pulses, respectively. Here, the photoelectron intensity at zero transversal momentum vanishes, although the squared Legendre polynomials in (a) exhibit maxima at 0° and 180°. This is due to the solid-angle-dependent detection of the charged particles by the Reaction Microscope (see Subsection 2.1). The detected number

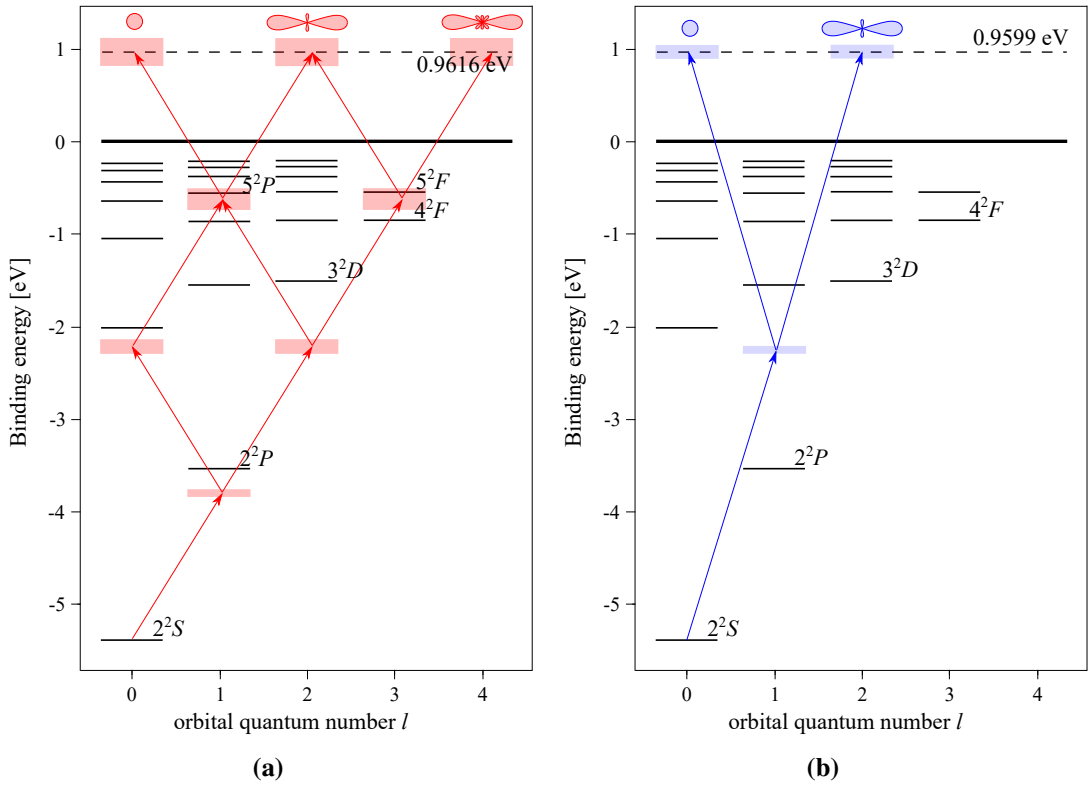

Figure 3.1.: Single-color ionization via absorption of (a) four photons at 780 nm and (b) two photons at 390 nm.

of particles scales with the surface element of a sphere given by the differential solid angle

$$d\Omega = \sin\theta d\theta d\varphi. \tag{3.1}$$

Since $\sin(0°) = \sin(180°) = 0$, the information on particles emitted into these polar angles is lost.

Figures 3.2 (c1) and (c2) show the measured longitudinal momentum spectra, which can be thought of as the 2D momentum distribution integrated over the transversal momenta. In Figures 3.2 (d1) and (d2), we see the measured photoelectron angular distributions (PADs). PADs show the intensity distribution of the emitted photoelectrons at various emission angles. The PAD resulting from ionization with fundamental pulses is predominantly (i.e., in lowest order) a superposition of s-, d-, and g-waves, whereas it is a superposition of s- and d-waves with SH pulses. The relative phase between these partial waves is determined by their scattering phase shifts η_l (see Eq. (1.9)).

3.1.2. Two-color multiphoton ionization

Figures 3.3 and 3.4 display ^{6}Li(nl) energy-level diagrams with ionization pathways induced by two-color pulses, which excite the main photoline and the first Above-Threshold Ionization (ATI) photoline, respectively. For now, in the discussion of lithium

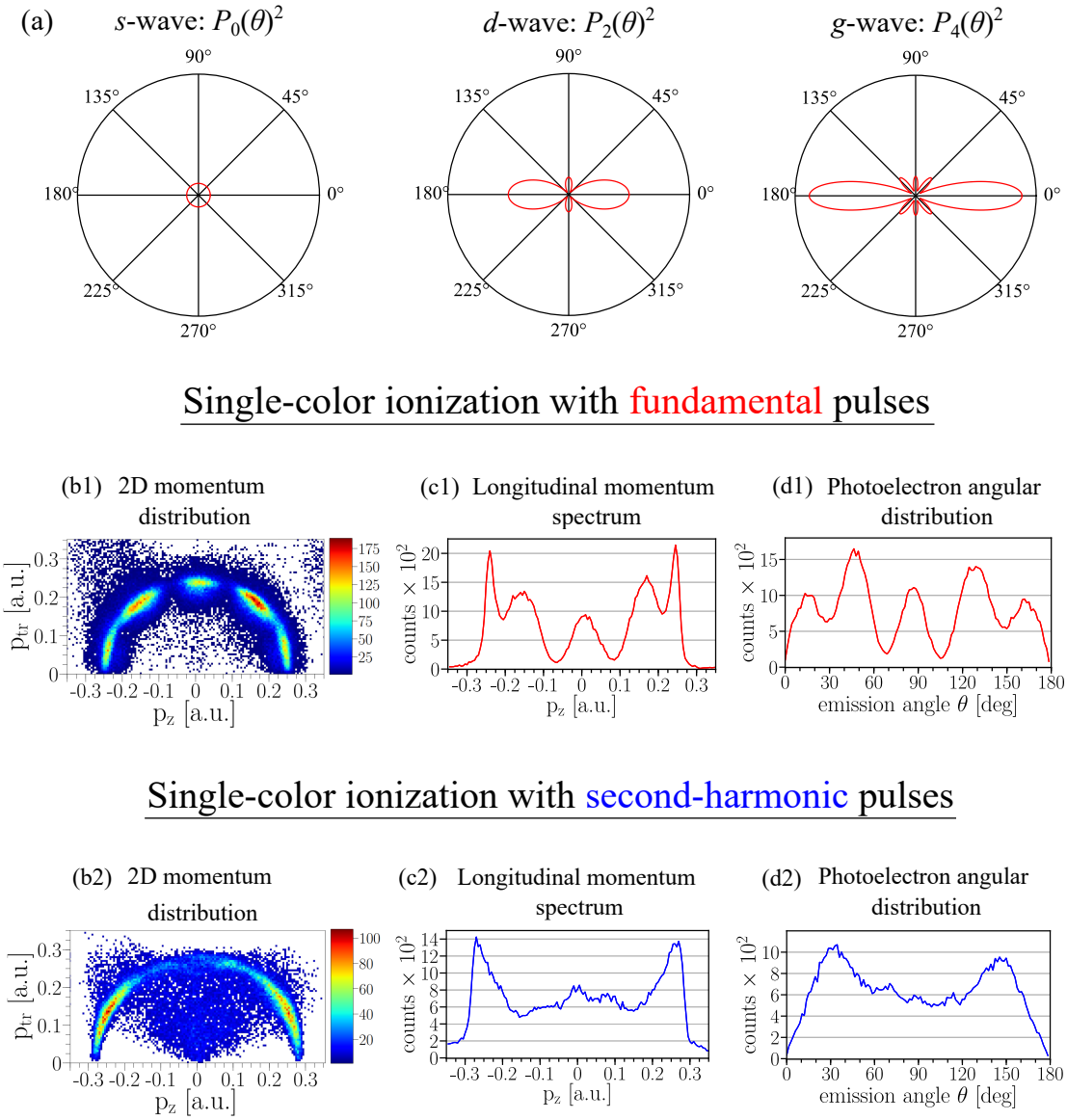

Figure 3.2.: (a) Polar plots of squared Legendre polynomials $P_l(\theta)^2$ describing the angular part of partial waves of the emitted photoelectrons. (b1,b2) 2D momentum distributions. (c1,c2) Longitudinal momentum spectra. (d1,d2) Photoelectron angular distributions.

below, we will concentrate on the main photoline. We see that six partial waves are generated by absorbing two to four photons. The two-color laser field enables the control of the relative phase between partial waves by changing the relative optical phase between the two harmonics of the two-color laser pulse. Describing the relative phase relation between all the partial waves constituting the PAD is by no means straightforward. However, the control mechanism can more easily be described in two-color ionization via single- and two-photon absorption as demonstrated, for example, in a previous study on neon [14]. Therefore, we take a brief retreat from the discussion of lithium and refer to this simpler case of neon. That case is very instructive to understand how the relative

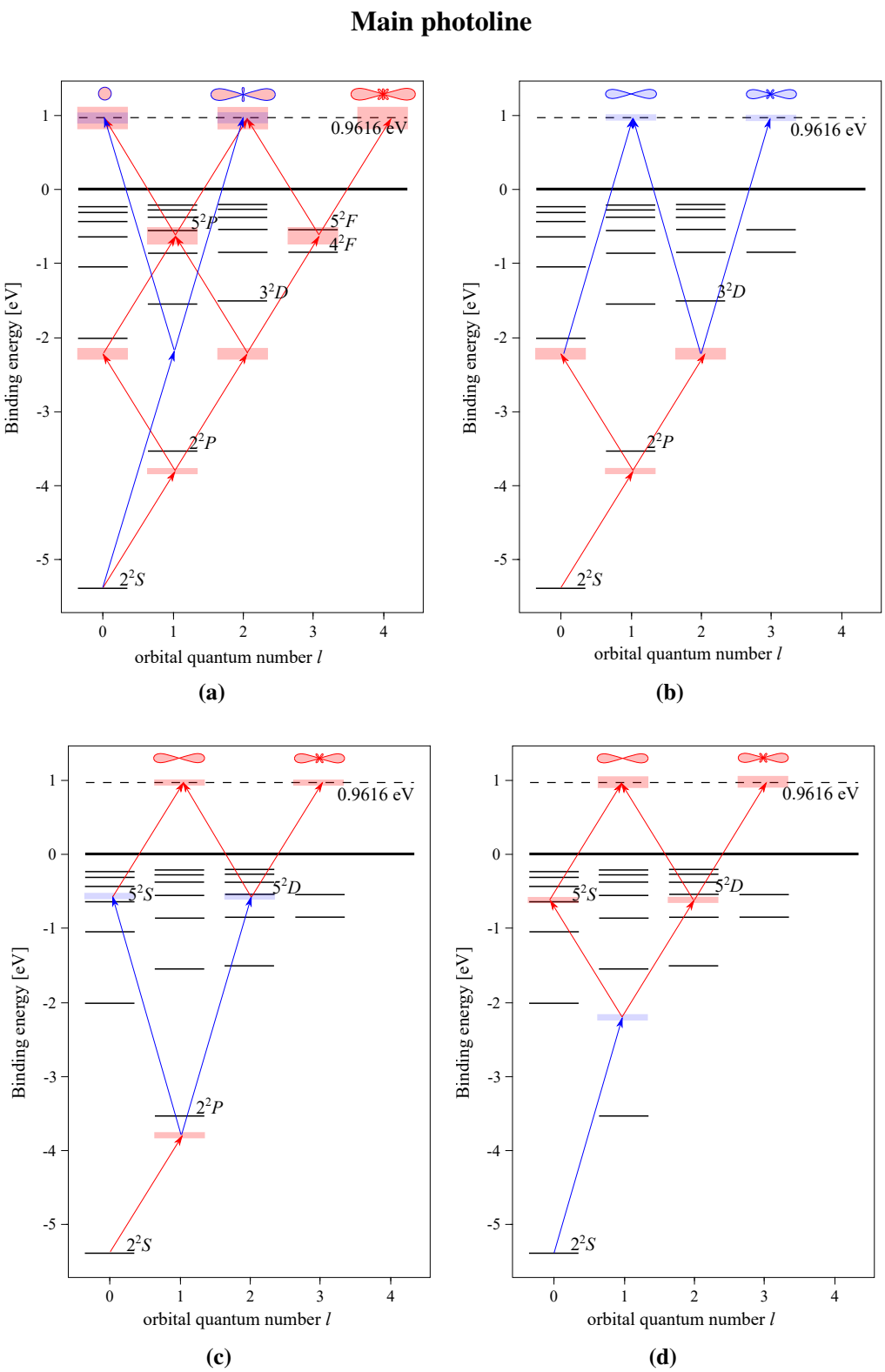

Figure 3.3.: Excitation of the main photoline of ^{6}Li starting from its 2^2S ground state via ionization pathways induced by a bichromatic laser field built from 780 nm (red arrows) and 390 nm (blue arrows) femtosecond laser pulses. Only red arrows: (a) 4-photon interaction via $(4 \times \omega)$ pathway. Only blue arrows: (a) 2-photon interaction via $(2 \times 2\omega)$ pathway. Red and blue arrows: (b) 3-photon interaction via $(2 \times \omega + 1 \times 2\omega)$ pathway. (c) 3-photon interaction via $(1 \times \omega + 1 \times 2\omega + 1 \times \omega)$ pathway. (d) 3-photon interaction via $(1 \times 2\omega + 2 \times \omega)$ pathway.

1st ATI photoline

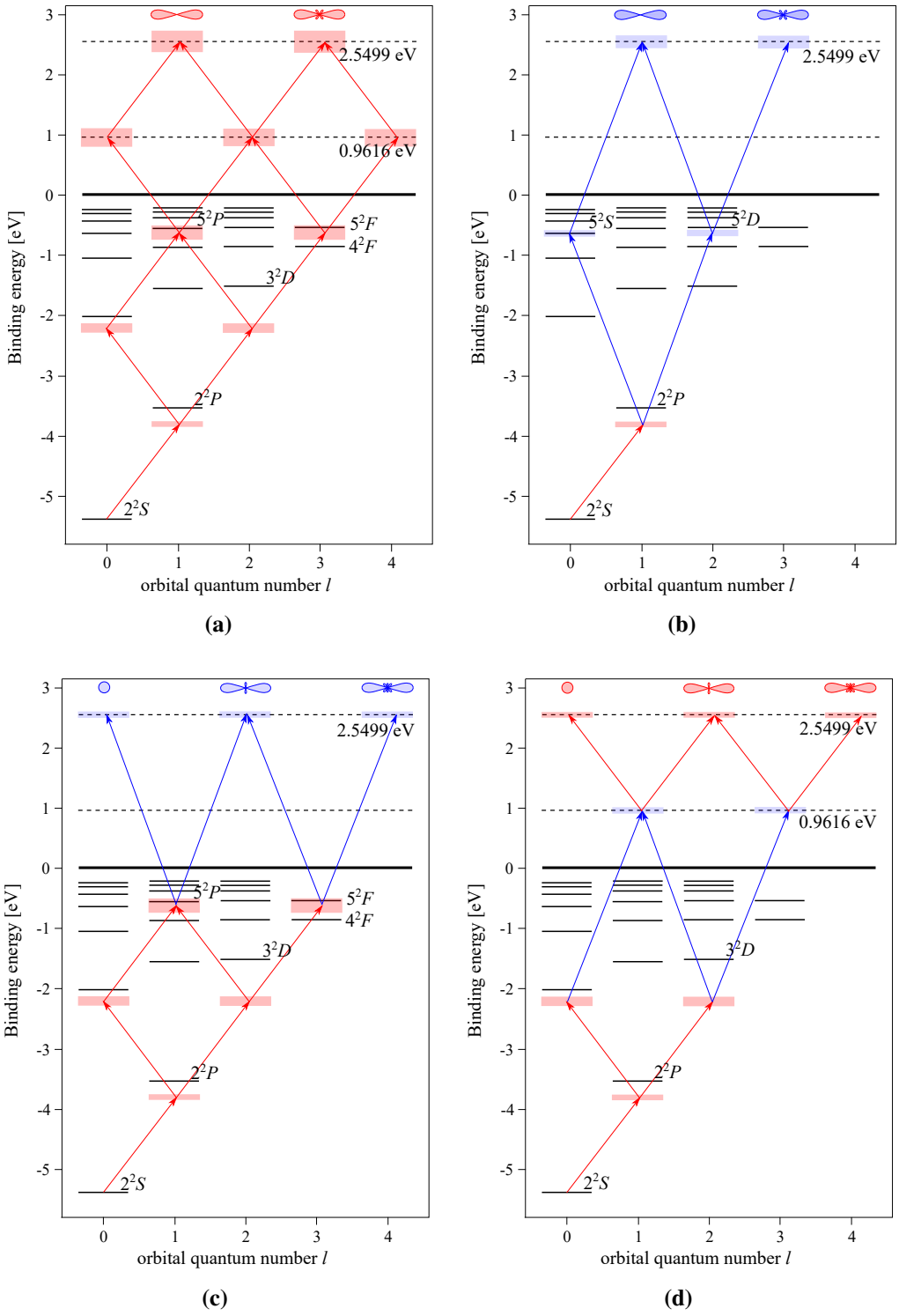

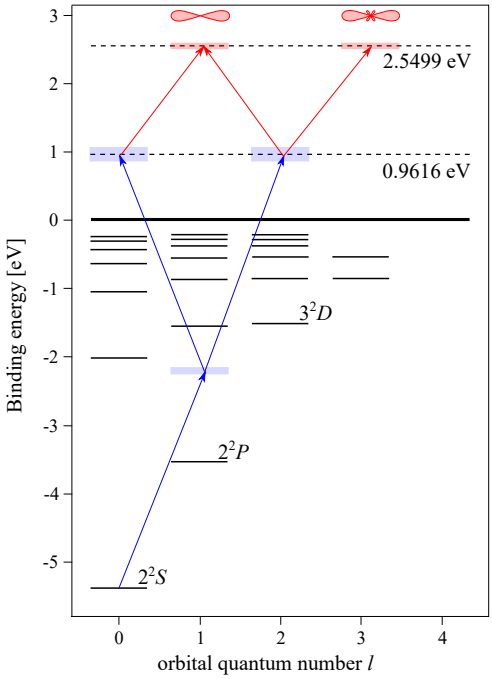

Figure 3.4.: Excitation of the 1st ATI photoline of ^{6}Li starting from its 2^2S ground state via ionization pathways induced by a bichromatic laser field built from 780 nm (red arrows) and 390 nm (blue arrows) femtosecond laser pulses. Only red arrows: (a) 5-photon interaction via $(5 \times \omega)$ pathway. Red and blue arrows: (b) 3-photon interaction via $(1 \times \omega + 2 \times 2\omega)$ pathway. (c) 4-photon interaction via $(3 \times \omega + 1 \times 2\omega)$ pathway. (d) 4-photon interaction via $(2 \times \omega + 1 \times 2\omega + 1 \times \omega)$ pathway. (e) 3-photon interaction via $(2 \times 2\omega + 1 \times \omega)$ pathway.

phase between the partial waves is controlled by varying the relative phase between the two harmonics of the two-color laser pulse.

3.1.2.1. Learning from two-color ionization of neon

Figure 3.5 shows ionization pathways induced in neon by a two-color laser field consisting of the fundamental ω and second-harmonic 2ω frequency components in the XUV spectral range. The fundamental pulses induce an ionization pathway via an intermediate resonance with the $(2p^5 4s)^1P_1$ state. This ionization pathway dominates the other two pathways induced by the fundamental pulses, which are off-resonant with the nearby-lying $(2p^5 3d)$ states. Consequently, the latter two pathways can be ignored in the following discussion.

The two-color laser field is described by

$$E(t) = \sqrt{I_\omega(t)}\cos\omega t + \sqrt{I_{2\omega}(t)}\cos(2\omega t - \Phi), \tag{3.2}$$

where I_ω(t) and $I_{2\omega}$(t) are the pulse intensity envelopes, and Φ is the relative optical phase between the two-color pulses. The ionization yield $I(\theta)$ of the PAD can then be

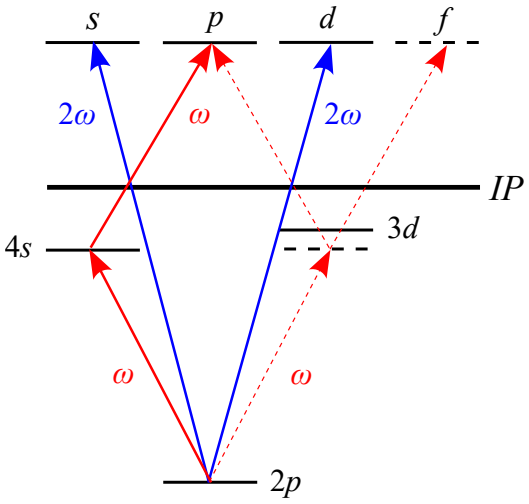

Figure 3.5.: Ionization pathways induced in neon starting from the $2p$ orbital in the $(2p^6)^1S$ initial state via two-photon absorption at frequency ω and single-photon absorption at frequency 2ω. The red dashed arrows indicate the ignored ionization pathways. The figure is adapted from [13].

described as

$$I(\theta) = \left|c_s e^{i\eta_s} P_0(\theta) + c_p e^{i(\eta_p+\Phi)} P_1(\theta) + c_d e^{i\eta_d} P_2(\theta)\right|^2, \tag{3.3}$$

where c_s, c_p, and c_d are partial-wave amplitudes, θ is the polar angle with respect to the polarization direction, and η_s, η_p, η_d are scattering phase shifts. Equation (3.3) shows that the relative phase Φ between the two harmonics enables control of the phase between the even- and odd-parity partial waves and, thereby, the control of the left-right asymmetry of the photoelectron emission pattern. An example of the measurement of such an asymmetric photoelectron emission pattern can be found in Figure 2 of [13].

3.1.2.2. Anisotropy and asymmetry control of PADs

In contrast to the single-color ionization of the ground state lithium with 780 nm or 390 nm laser pulses, where the parity of the partial waves is restricted to even, a two-color laser field can induce ionization pathways that lead to both even- and odd-parity partial waves (see Figure 3.3). In particular, the 780/390 nm laser field excites the odd-parity p- and f-partial waves in addition to the even-parity s-, d- and g-partial waves. The polar plots of the squared Legendre polynomials $P_l(\theta)^2$ of the odd-parity p- and f-partial waves are displayed in Figure 3.6 (a).

The measured 2D momentum distribution, longitudinal momentum spectrum, and PAD of the main photoline, in the case of the two-color ionization at 780/390 nm, are displayed in Figures 3.6 (b), (c) and (d), respectively. Compared to the photoelectron spectra with only fundamental pulses (see Figures 3.2 (b1 - d1)), the two-color spectra exhibit higher photoelectron yield around the minima. This enhancement at the minima can most likely be attributed to the odd-parity f-wave, which can only be induced by the two-color field.

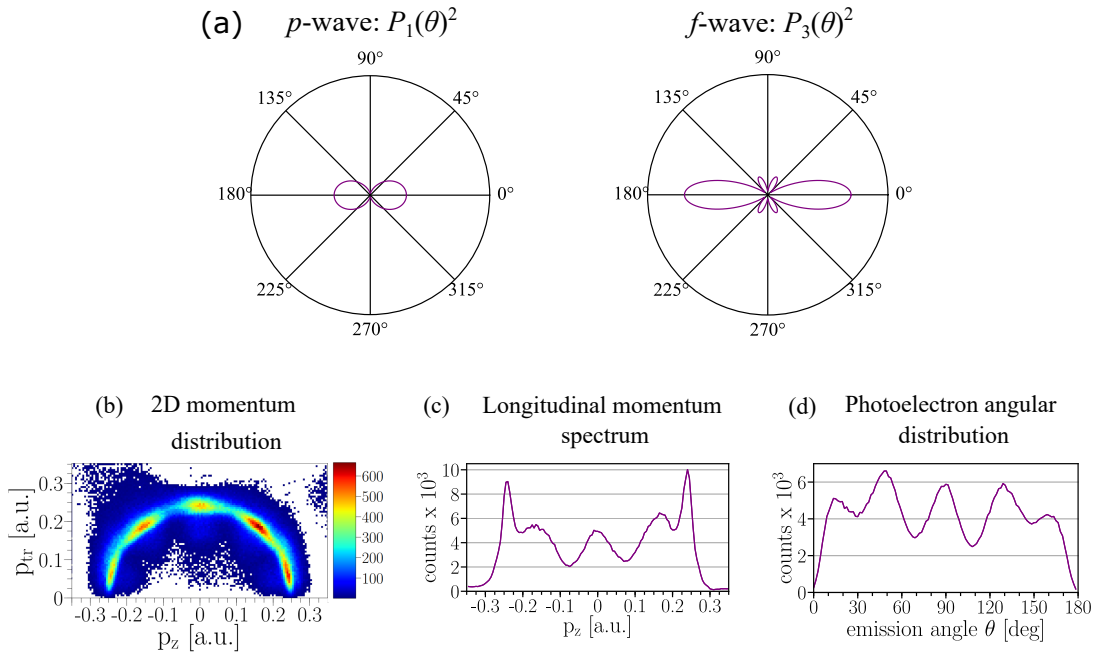

Figure 3.6.: (a) Polar plots of squared Legendre polynomials $P_l(\theta)^2$ describing odd-parity p- and f-waves of the ejected photoelectrons, which are produced by MPI of the lithium ground state by two-color pulses with 780 nm and 390 nm. (b) Two-dimensional momentum distribution. (c) Longitudinal momentum spectrum. (d) Photoelectron angular distribution.

The pathways depicted in Figures 3.3 and 3.4 show that in ionization of lithium by a two-color laser field, we can distinguish three cases of interference between two partial waves depending on their parity and angular momenta. Specifically, interference between partial waves of:

- the same angular momentum (see, e.g., s- and d-partial waves in Fig. 3.3 (a));
- different angular momenta of either even or odd parity (see, e.g., interference between the pairs of s- and g-waves as well as d- and g-waves in Fig. 3.3 (a));
- even and odd parity (see Figure 3.3 for interference between ionization pathways induced by absorption of three photons as in (b), (c), and (d), and the ionization pathways induced by single-color frequency components as in (a)).

Figure 3.7 depicts examples of PADs for each case at various relative optical phases Φ. First, in Figure 3.7 (a, left column), we examine interference between partial waves with the same angular momentum. In this case, changing the relative phase Φ can enhance or reduce the amplitude of the partial wave. Next, we look at the interference between partial waves with different angular momenta. In Figure 3.7 (b, middle column), PADs resulting from interference between the partial waves of the same parity are shown. Their

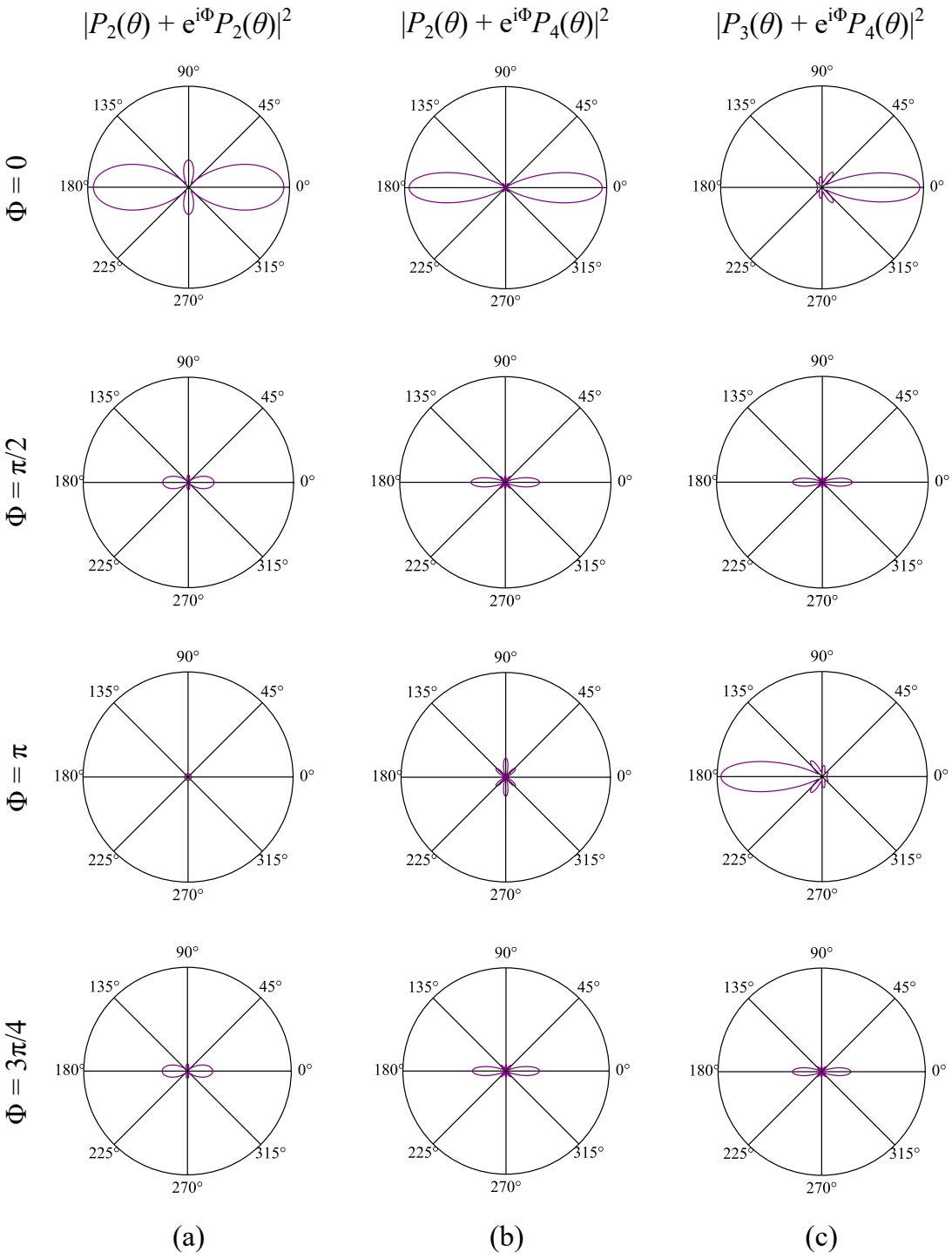

Figure 3.7.: Examples of interference between (a) partial waves with the same angular momentum, (b) even-parity partial waves with different angular momenta, and (c) odd-parity and even-parity partial waves with various relative optical phases Φ between the two harmonics of the two-color pulse.

dependence on the relative phase Φ shows a strong effect on the anisotropy. Finally, in Figure 3.7 (c, right column), PADs resulting from the interference between partial waves of opposite parity are shown. Changing the relative phase Φ between the even- and odd-parity partial waves enables control of the left-right asymmetry of the PADs.

Besides the interpretation of the left-right asymmetry of PADs in terms of the interference between the odd and even parity partial waves, alternatively it might be considered from the point of view of the changes in the total electric field of the two-color pulses $E(t)$ (see Eq. 3.2) with the relative phase Φ as shown in Figure 3.8. We see that $E(t)$ exhibits a phase-dependent substructure and that its relative amplitudes of the pulse envelopes at positive and negative electric fields vary. The displayed electric fields were used in the calculations presented in Chapter 4.

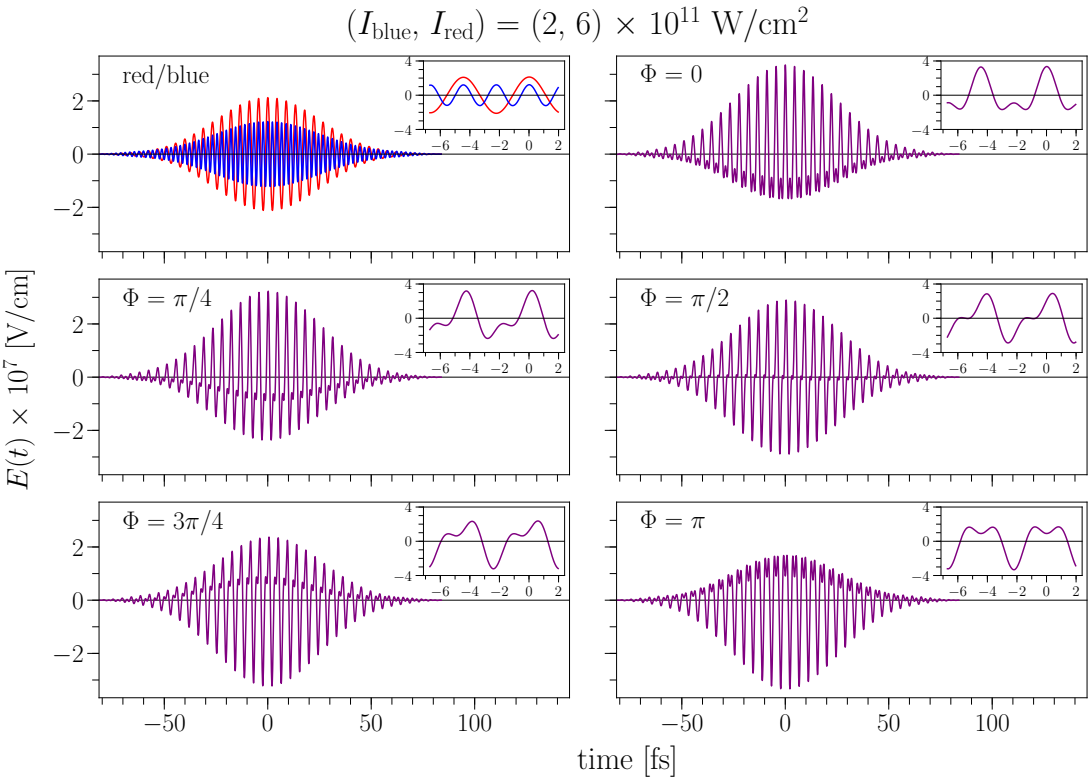

Figure 3.8.: Individual components (top left panel) and the total electric field $E(t)$ of two-color pulses (remaining panels) at various relative phases Φ. The insets show a few cycles near the maximum of the envelope functions.

3.2. Energy level shifts

This section considers the dynamical resonances with the Rydberg states of ^{6}Li. As explained in Subsection 1.2.3, dynamical resonances occur at certain intensities of the ionizing radiation when the energies of the unperturbed bound states are shifted in or out of resonance with the virtual states due to the AC Stark effect.

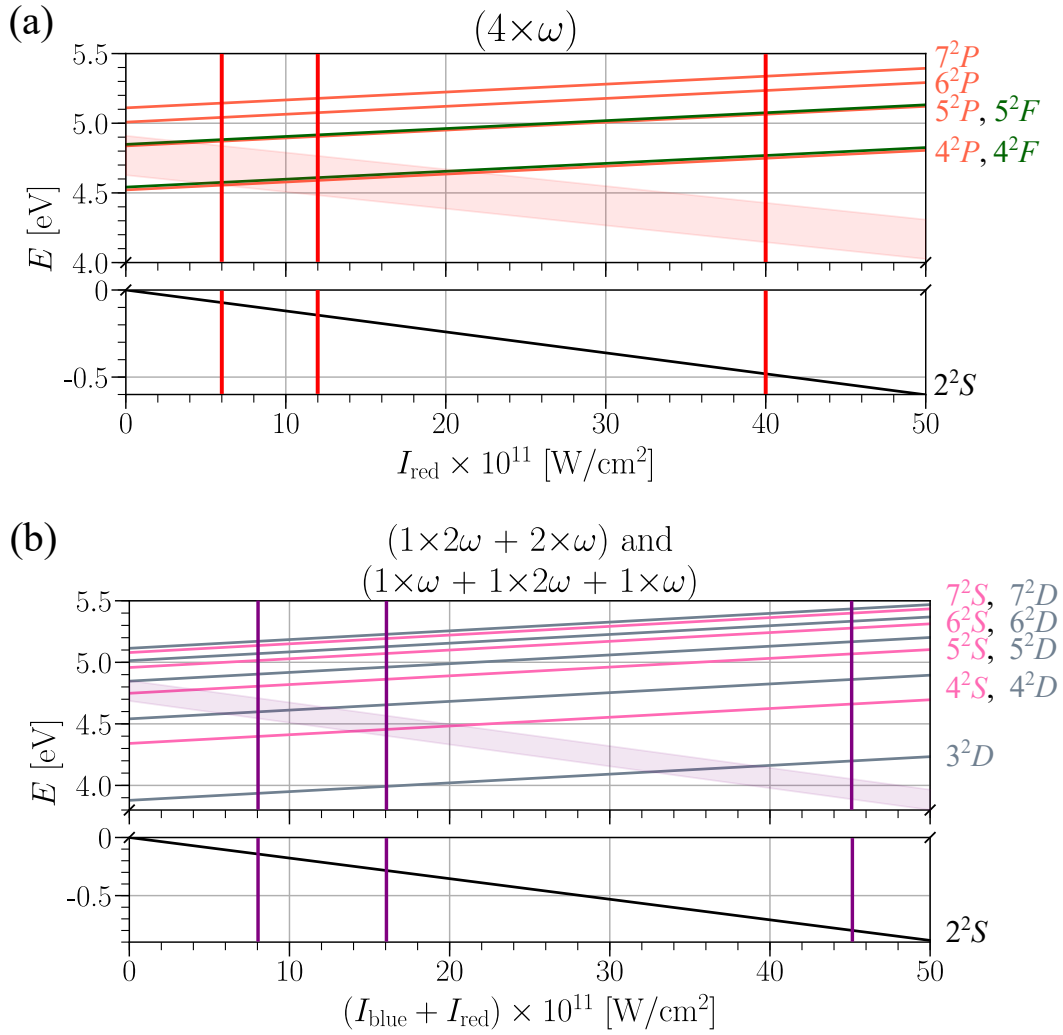

Figure 3.9.: AC Stark-shifted energies of the ^{6}Li ground state and Rydberg states versus (a) fundamental radiation intensity, I_{red}, and (b) total intensity of the fundamental and SH radiation, $I_{\text{red}} + I_{\text{blue}}$. The shaded areas mark the energy width of the virtual states after absorption of (a) three fundamental light photons and (b) one fundamental and one SH light photon with the fundamental photon energy of $E_{\text{ph}}(\omega) \pm \Delta E_{\text{ph}}(\omega) = 1.59 \pm 0.02$ eV and the SH photon energy of $E_{\text{ph}}(2\omega) \pm \Delta E_{\text{ph}}(2\omega) = 3.18 \pm 0.018$ eV. The uncertainties $\Delta E_{\text{ph}}(\omega)$ and $\Delta E_{\text{ph}}(2\omega)$ are given by the HWHM of the photon energy spectrum. The figure titles indicate ionization pathways, which can exhibit dynamical resonances with the Rydberg states (see Figure 3.3). The red and purple vertical lines indicate the different absolute intensities of (a) the fundamental and (b) the sum of the fundamental and SH light, respectively, used in the calculations in Chapter 4 (see Figures 4.10 and 4.11).

In the case of excitation of the main photoline, several ionization pathways include intermediate resonances with Rydberg states. Specifically, the ionization pathways shown in Figure 3.3 exhibit intermediate resonances via single-color ionization with the fundamental radiation in (a) and via two-color ionization in (c) and (d). In Figure 3.9, we inspect the intensity dependence of the ground state and the relevant Rydberg states associated with each of these ionization pathways. In particular, we are interested in which states are shifted in or out of resonance at the laser intensities used in the calculations presented in Section 4.2.

The single-color $(4 \times \omega)$ ionization pathway exhibits resonances with the 4^2P and 4^2F states at $I_{\text{red}} = 6 \times 10^{11}$ W/cm^2 and $I_{\text{red}} = 12 \times 10^{11}$ W/cm^2. At $I_{\text{red}} = 40 \times 10^{11}$ W/cm^2 no intermediate resonances are present. On the other hand, the two-color ionization pathways $(1 \times \omega + 1 \times 2\omega + 1 \times \omega)$ and $(1 \times 2\omega + 2 \times \omega)$ exhibit a resonance with the 4^2D state at $I_{\text{red}} + I_{\text{blue}} = 8 \times 10^{11}$ W/cm^2 and with the 4^2S state at $I_{\text{red}} + I_{\text{blue}} = 16 \times 10^{11}$ W/cm^2. At $I_{\text{red}} + I_{\text{blue}} = 45 \times 10^{11}$ W/cm^2 no intermediate resonances are present. For the calculations of the energy shifts of the ground state and the Rydberg states, we used the approximations presented in Subsection 1.2.3. Specifically, we used Eq. (1.8) for the energy shift of the ground state, and the approximation that their energy shift is very close to the ponderomotive shift of the continuum for the Rydberg states.

Tables 3.1 and 3.2 summarize the energy level shifts of the ground state and the resonant Rydberg states at certain fundamental intensities, as well as the sum of the fundamental and SH light intensities, respectively.

$I_{\text{red}} \times 10^{11}$ [W/cm^2]	$\Delta E(2^2S)$ [eV]	$\Delta E(4^2P)$ [eV]	$\Delta E(4^2F)$ [eV]
6	-0.072	0.034	
12	-0.144	0.068	

Table 3.1.: Energy shifts of the ground and the resonant Rydberg states at certain intensities of the fundamental radiation used in the calculations in Section 4.2.

$(I_{\text{blue}} + I_{\text{red}}) \times 10^{11}$ [W/cm^2]	$\Delta E(2^2S)$ [eV]	$\Delta E(4^2D)$ [eV]	$\Delta E(4^2S)$ [eV]
2 + 6 = 8	-0.088	0.037	-
4 + 12 = 16	-0.176	-	0.074

Table 3.2.: Energy shifts of the ground and the resonant Rydberg states at certain intensities of the sum of the fundamental and SH radiation used in the calculations in Section 4.2.

3.3. Two-color optical setup

Figure 3.10 shows a schematic drawing of our collinear optical setup for generating a phase-locked two-color laser field. This setup provides the generation of the SH radiation, control of the temporal overlap between the fundamental and SH pulses, and the control

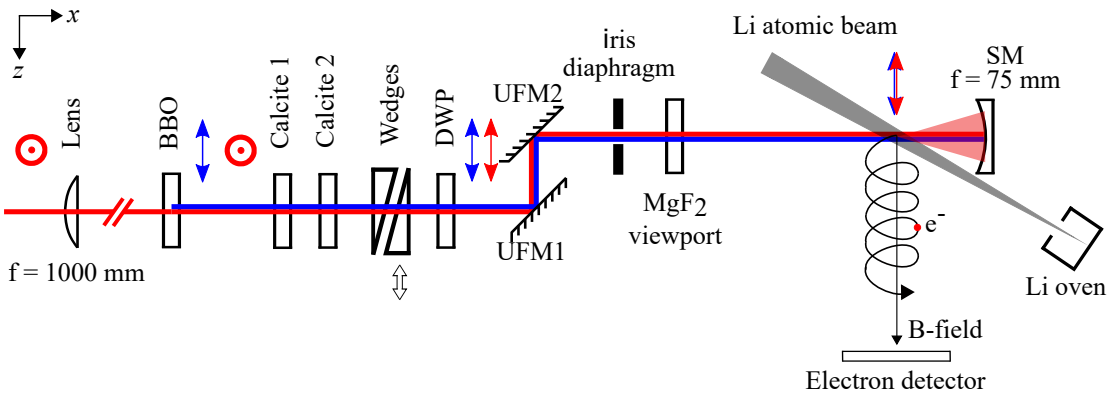

Figure 3.10.: Schematic illustration of the optical setup for generating a phase-locked two-color laser field. Lens: Plano-concave lens with f = 1000 mm; BBO: Beta Barium Borate crystal; Calcite 1, Calcite 2: Calcite delay compensation plates; Wedges: A pair of dispersion wedges; DWP: Dual wavelength waveplate; UFM1, UFM2: Dual-band ultrafast mirrors coated for 800 nm and 400 nm. MgF_2 viewport: vacuum viewport window of the Reaction Microscope. SM: Aluminum-coated concave spherical mirror with f = 75 mm. Red and blue arrows: p-polarization of the fundamental and SH harmonics, respectively; Red circles: s-polarization of the fundamental harmonic.

of the relative phase between the temporally overlapping pulses with subwavelength accuracy.

3.3.1. Second-Harmonic Generation

We generate the SH light using a β-BBO crystal (BBO-602H, EKSMA OPTICS). β-BBO crystals are birefringent materials, i.e., their refractive index depends on the polarization and propagation direction of the light beam with respect to the crystal optical axis (O.A.). Light beams with their polarization perpendicular to the O.A. are defined as ordinary waves. The refractive index n_o of an ordinary wave does not depend on the light-propagation direction. Light beams that do not propagate along the O.A. and whose polarization lies in the plane spanned by the propagation direction of the light beam $\vec{k}$ and the O.A. are defined as extraordinary waves. The refractive index $n(\Theta)$ of an extraordinary wave depends on the beam propagation direction, where Θ is the angle between the wave vector $\vec{k}$ and the O.A. For $\vec{k} \parallel$ O.A., $\Theta = 0°$. In general, the extraordinary index of refraction $n(\Theta)$ can be calculated according to the following expression

$$\frac{1}{n^2(\Theta)} = \frac{\cos^2\Theta}{n_o^2} + \frac{\sin^2\Theta}{n_e^2}, \tag{3.4}$$

where $n_e = n(\Theta = 90°)$ [51].

Birefringent crystals are categorized as positive and negative. This is determined by the birefringence parameter

$$\Delta n = n_o - n_e. \tag{3.5}$$

β-BBO crystals exhibit negative birefringence. In such a material, Second-Harmonic

Generation (SHG) takes place when the phase-matching (PM) condition

$$n_o(\omega) = n(\Theta, 2\omega) \tag{3.6}$$

is fulfilled. Here ω and 2ω are the angular frequencies of the fundamental and its SH radiation.

The PM condition can be better understood by means of the refractive index surfaces illustrated in Figure 3.11 (a). They show that the PM condition is fulfilled at the PM angle Θ_m formed between the PM direction and the O.A. The latter two define the PM plane. In practice, the PM condition can be realized if the crystal is cut so that the PM direction is normal to the manufactured crystal surface and the fundamental beam propagates along it as illustrated in Figure 3.11 (b). This illustration shows that Θ_m can be fine-tuned by rotating the crystal around its ordinary axis. It also indicates the orientation of polarization of the fundamental and SH waves. A fundamental wave is an ordinary wave with its polarization orthogonal to the PM plane. The SH wave is extraordinary, and its polarization is orthogonal to that of the ordinary wave, i.e., it lies within the PM plane. Therefore, the BBO crystal generates a co-propagating two-color beam with orthogonal linear polarizations.

The SHG efficiency depends on the peak intensity of the fundamental pulses, which is defined as

$$I = \frac{2E_p}{\pi w_1 w_2 T}, \tag{3.7}$$

where E_p is the pulse energy, w_1, w_2 are beam diameters along the x- and y-directions measured at the 1/e^2 level, and T is the pulse duration. The required pulse peak intensity for reaching an SHG efficiency higher than 20% with our BBO crystal is about 300 GW/cm^2. Therefore, we focus the fundamental beam with a 1000 mm lens to reach a sufficiently high fundamental pulse peak intensity and place the BBO crystal at its waist. We also compensate for the dispersion of fundamental pulses at the plane of the BBO crystal by precompensating it with a prism compressor of the femtolaser system. When precompensating the dispersion of the fundamental pulses, we assumed that they were optimally compressed when the peak SHG efficiency was reached. However, we cannot compensate for the dispersion of the co-propagating fundamental and SH pulses introduced by all the optical elements behind the β-BBO crystal.

3.3.2. Delay compensation

Different group velocities of the pulses at 780 nm and 390 nm, while propagating through various optical elements behind the β-BBO crystal and in the air, lead to a delay between them. There are two ways to compensate for this delay. One way is to build a two-color interferometer. For example, a two-color Mach-Zehnder interferometer is based on an optical delay line consisting of a retroreflector combined with a translation stage built in the arm of the fundamental beam [52]. Another example is a two-color interferometer, where the delay is changed by a pair of dispersion wedges instead of a conventional optical delay line [53]. A two-color interferometer might be preferred if an independent control of the absolute intensities or polarizations of the two-color beams is

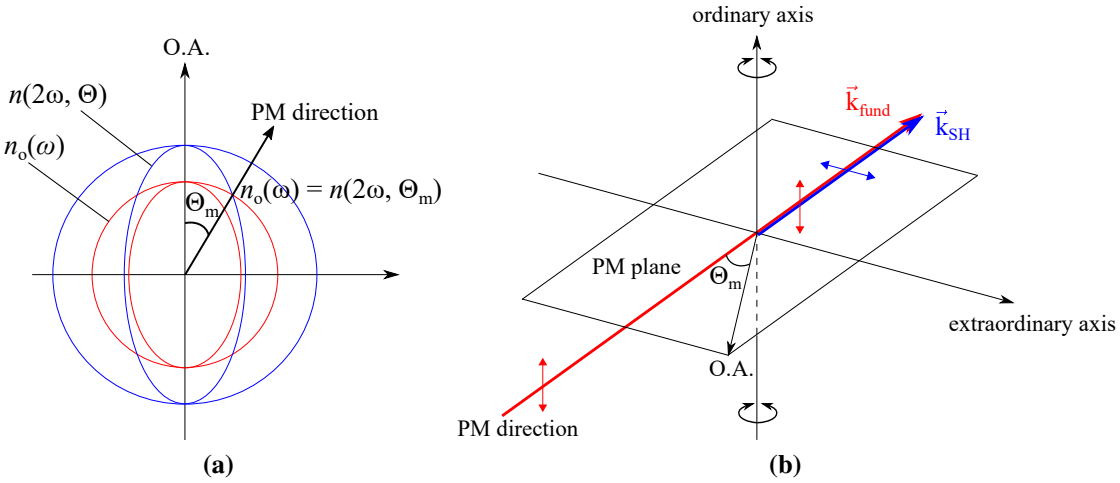

Figure 3.11.: (a) Refractive index ellipsoid depicting a negative birefringence crystal. Red (blue) spheres represent $n_o(\omega)$ ($n_o(2\omega)$). Red (blue) ellipsoids represent $n(\Theta, \omega)$ ($n(\Theta, 2\omega)$). The arrow at an angle Θ_m with respect to the O.A. indicates the PM direction. (b) The PM plane is defined by the crystal O.A. and the PM direction, where the latter is normal to the crystal surface. The fundamental and SH beams are co-propagating along the PM direction. The ordinary axis of the crystal defines the direction along which the polarization of the fundamental beam must be oriented. The extraordinary axis of the crystal defines the orientation of the SH light polarization.

necessary. Otherwise, delay compensation with an in-line, i.e., collinear, optical setup is recommended, where the fundamental and SH beams are co-propagating, and the relative delay between the two-color pulses is controlled by delay compensation plates [10, 54]. Compared to the two-color interferometer, one advantage is that it does not require splitting and recombining the two-color beams. The latter is often accompanied by lateral displacements between them, as the recombination requires precise alignment and good beam pointing stability.

Calculated delays τ between the 780 nm and 390 nm pulses introduced by optical elements of our optical setup and the air are listed in Table 3.3. All optical elements given in the table and the air make the 780 nm pulse advance the 390 nm pulse. We compensate for the total delay τ_{total} by using two calcite delay compensation plates (TDC12108-AR and TDC12102-AR, Newlight Photonics). For this, the ordinary axis of the calcite plate has to be aligned with the polarization of the advancing 780 nm pulse, whereas its extraordinary axis with a lagging 390 nm pulse. The compensated delay is then varied by changing the angle of incidence of the two-color beam on the calcite crystal surface. We mount one of the calcite plates on a manual rotation stage and adjust it at a fixed angle. The other calcite plate is mounted on a motorized rotation stage (PRM1/MZS, Thorlabs) and is used to vary the relative delay between the two harmonics.

	τ [fs]
β-BBO	42
wedges	309.6
dual-wavelength waveplate	365.5
MgF_2	216.2
air	93.4
τ_{total} [fs]	1026.8 fs

Table 3.3.: Calculated delays between the 780 nm and 390 nm pulses introduced by optical elements of the two-color optical setup and the air. $\tau > 0$ corresponds to the 780 nm pulse advancing the 390 nm pulse.

3.3.3. Subwavelength delay control

A pair of fused silica wedges (23RQ12-02-M, Newport) is implemented for performing delay scans with subwavelength accuracy. By installing one of the wedges on a linear translation stage, its insertion can be varied, thereby effectively forming a glass plate with a variable thickness. In the literature, using a pair of wedges for subwavelength delay scans is recommended because the coarse displacement of the wedge insertion corresponds to much finer steps in the optical delay [55]. The relative delay change $\Delta\tau$ for 780 nm and 390 nm pulses by changing the displacement of the wedge insertion Δl is described by the relationship

$$\Delta\tau = \Delta l \left(n_{390} - n_{780}\right) \tan(\alpha), \tag{3.8}$$

where n_{390} and n_{780} are the refractive indices of fused silica at 780 nm and 390 nm, respectively, and α is the wedge angle. According to this expression, we estimate that, for our wedges, a displacement of 454 μm corresponds to one optical period of the 390 nm light, which is ~1.3 fs.

3.3.4. Integration of two-color beam in ReMi

Before passing through a vacuum viewport window, the fundamental pulse polarization is aligned along that of the SH pulse using a dual-wavelength waveplate (465-4221, EKSMA OPTICS), which acts as a $\lambda/2$ waveplate at 780 nm and as a λ waveplate at 390 nm. Because the fundamental beam size is larger than the second-harmonic beam, we use an iris diaphragm to cut away the part of the two-color beam, where only the fundamental beam is present. The two-color beam is focused on a lithium atomic beam by an aluminum-coated spherical mirror with f = 75 mm (CM254-075-G01, Thorlabs). Since the beam waist of a focused Gaussian beam is proportional to its wavelength, the fundamental beam exhibits a twice as large beam waist as the SH beam. However, due to the imperfect matching of the beam sizes of the two harmonics, we cannot state that this was exactly the case in our experiments. Nevertheless, the mismatch between the sizes of the foci of the two frequency beams is generally the disadvantage of the collinear arrangement of the two-color optical setup. Photoelectrons created within the

focal volume of the two-color beam are extracted by means of electric and magnetic fields and detected (see Section 2.1).

4. Results

This chapter presents the main results of this thesis. In Section 4.1, we compare longitudinal momentum spectra (intensity of the photoelectrons as a function of their momenta along the light polarization direction) of the main photoline and the 1st Above-Threshold Ionization (ATI) photoline resulting from two-color ionization with temporally overlapping and non-overlapping fundamental and second-harmonic (SH) pulses. In Section 4.2, we demonstrate the left-right asymmetry control of the photoelectron angular distributions (PADs) with subwavelength accuracy and compare the measured PADs with the theoretical predictions.

All the calculations that we compare our results with were performed by Prof. Klaus Bartschat (Drake University, Des Moines, Iowa, USA). Briefly, the Li atom is treated as a quasi-one-electron system, in which the $(1s^2)$ He-like core is considered inert, i.e., only the valence electron is affected by the laser radiation. The effect of the core is simulated by a static potential, which is enhanced by accounting for electron exchange and the polarizability of the core by semi-empirical potentials. More details can be found in several recent papers [56–59].

The laser pulses used in the calculations (see Figure 3.8) were generated as follows. We provided our best estimate of the pulse envelopes based on single-color measurements with 780 nm and 390 nm radiation. Since the remaining pedestals cannot be handled by the computer program without resulting in serious numerical problems, the pulses were slightly modified near the start and the end to ensure zero fields at these temporal edges. Then the peak intensities and the desired delays were set.

The experimental results presented in Section 4.1 and Section 4.2 were obtained at two different strengths of the magnetic extraction field B_{ext}, namely 3.8 G and 1.8 G, respectively. Examples of the corresponding photoelectron momentum and angular distributions measured at B_{ext} = 3.8 G can be seen in Figures 4.1 (a1) - (c1) and at B_{ext} = 1.8 G in Figures 4.1 (a2) - (c2). The two-dimensional momentum distributions are intersected by divergences, which arise from photoelectrons with their Time-of-Flight equal multiples of the cyclotron motion period. In this case, the electron is detected on the spectrometer axis (r = 0), and according to Eq. (2.6), the transversal momentum diverges. By changing the magnetic field strength and, thereby, the cyclotron motion period, the number and positions of the divergences can be varied. In (a1), both the main photoline and the 1st ATI photoline are intersected by divergences at p_z ~ -0.38 a.u., 0 a.u. and 0.45 a.u., whereas in (a2), only the 1st ATI photoline is affected at p_z ~ -0.35 a.u. and 0.43 a.u. On the other hand, B_{ext} = 3.8 G (a1) provides a higher acceptance of the transversal momentum, now including the 1st ATI photoline at 0.45 a.u. while this is not included at B_{ext} = 1.8 G (a2).

Since the divergences intersect both photolines at B_{ext} = 3.8 G, we study their

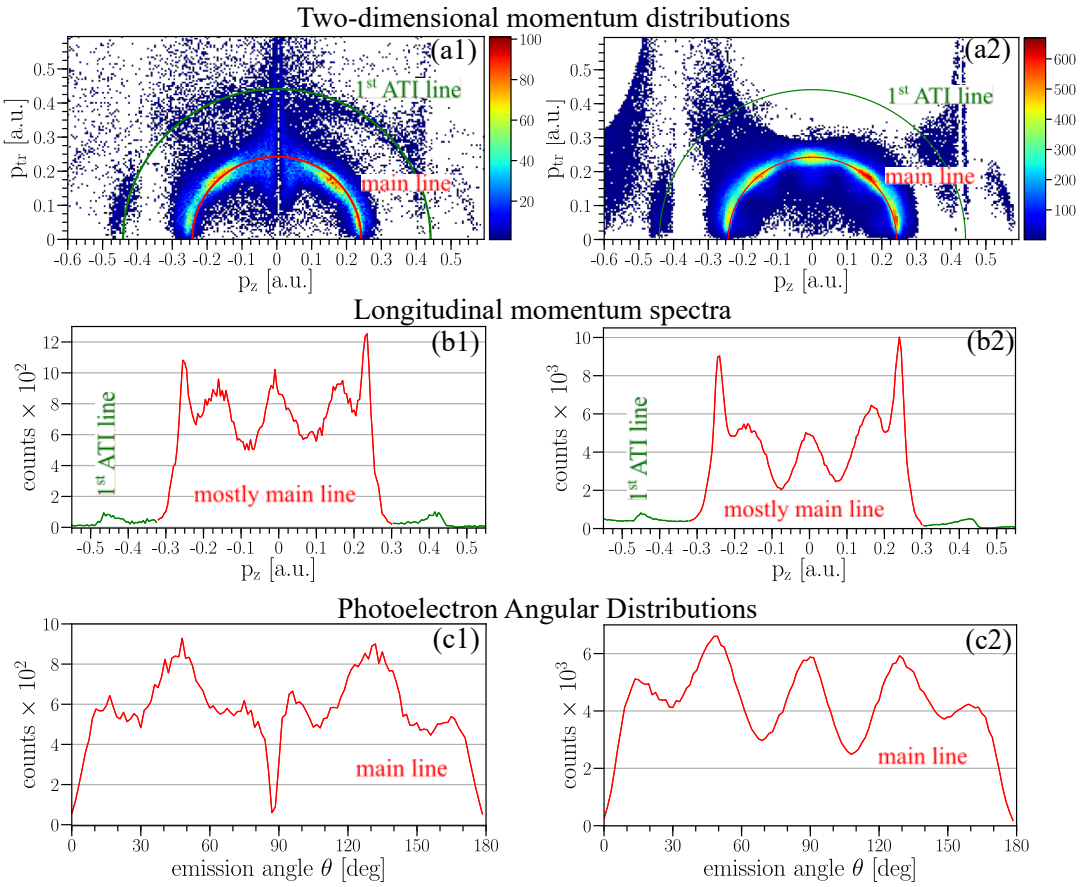

Figure 4.1.: Photoelectron distributions at the magnetic extraction field (a1) - (c1) B_{ext} = 3.8 G and (a2) - (c2) B_{ext} = 1.8 G.

longitudinal momentum spectra, where the divergences play no role. At B_{ext} = 1.8 G the main photoline is free of divergences. Therefore, we choose to study its PADs instead of its longitudinal momentum spectra.

4.1. Ionization with temporally overlapping and non-overlapping two-color pulses

This section deals with the difference between longitudinal momentum spectra resulting from ionization with temporally overlapping and non-overlapping two-color pulses. In addition, we want to determine whether the spectra generated at positive delays $\tau > 0$ are identical to those at negative delays $\tau < 0$.

Following the ionization pathways for the excitation of the main photoline indicated in Figure 3.3, in the case of the non-overlapping pulses, we expect the longitudinal momentum spectra at $\tau < 0$ and $\tau > 0$ to be identical, since only the single-color ionization pathways by each frequency component are accessible. On the other hand, differences

are expected in the longitudinal momentum spectra of the 1st ATI line. In particular, according to the ionization pathways shown in Figure 3.4, in addition to the single-color ionization pathways, the two-color ionization pathway (c) can be induced if the fundamental pulse advances the SH pulse ($\tau > 0$). This pathway can take place due to intermediate resonances with the Rydberg states, which are excited after the absorption of three photons at the fundamental frequency. Regarding the pulse overlap delay range, predicting how the spectra might differ at positive and negative delays is more difficult due to the many interfering pathways.

To investigate the delay-dependent features mentioned above, we look at the measured and calculated delay traces of longitudinal momentum spectra that cover the delay range extending between the SH pulse advancing the fundamental pulse ($\tau < 0$) and vice versa ($\tau > 0$).

The discussion below begins with inspecting first the measured and calculated delay traces of the longitudinal momentum spectra independently in Subsections 4.1.1 and 4.1.2, respectively. Specifically, we distinguish between the delay ranges corresponding to temporally overlapping and non-overlapping two-color pulses. After this, we compare the spectra at $\tau < 0$ and $\tau > 0$ to our expectations from the ionization pathways discussed above. We finish the discussion by comparing the measured and calculated delay traces in Subsection 4.1.3. Here, we also demonstrate the assignment of the dominant partial-wave character to several delay ranges of the longitudinal momentum spectra.

4.1.1. Measured delay trace

Figure 4.2 (a) shows the measured delay trace of longitudinal momentum spectra in steps of 8.75 fs. This step size is 3.36 times the optical period of the fundamental light of 2.6 fs. We observe a gradual change in the intensity distribution of the longitudinal momentum spectra along the delay scan range. This change results from the ionization pathways that can only be induced when the two-color pulses are temporally overlapping. We see that the redistribution of the longitudinal momentum spectra is symmetric with respect to $p_z = 0$. The symmetric redistribution of the spectra is associated with the interference between the ionization pathways involving partial waves of either the same angular momenta or the same parity (see Figures 3.7 (a) and (b)). Below, we demonstrate that after the background resulting from the single-color ionization is subtracted from the delay trace, the symmetrically redistributed spectra also show delay-dependent oscillations between their left-right intensity distributions with respect to $p_z = 0$.

4.1.1.1. Temporal overlap

As explained in Subsection 3.1.2, temporally overlapping two-color pulses excite both even- and odd-parity partial waves, and their interference results in asymmetric photoelectron angular distributions with respect to a plane orthogonal to the laser polarization direction. Therefore, we expect to observe an onset of asymmetry in the longitudinal momentum spectra if the two-color pulses temporally overlap. The delay range, where the two-color pulses overlap, can be determined by calculating the integrated ionization

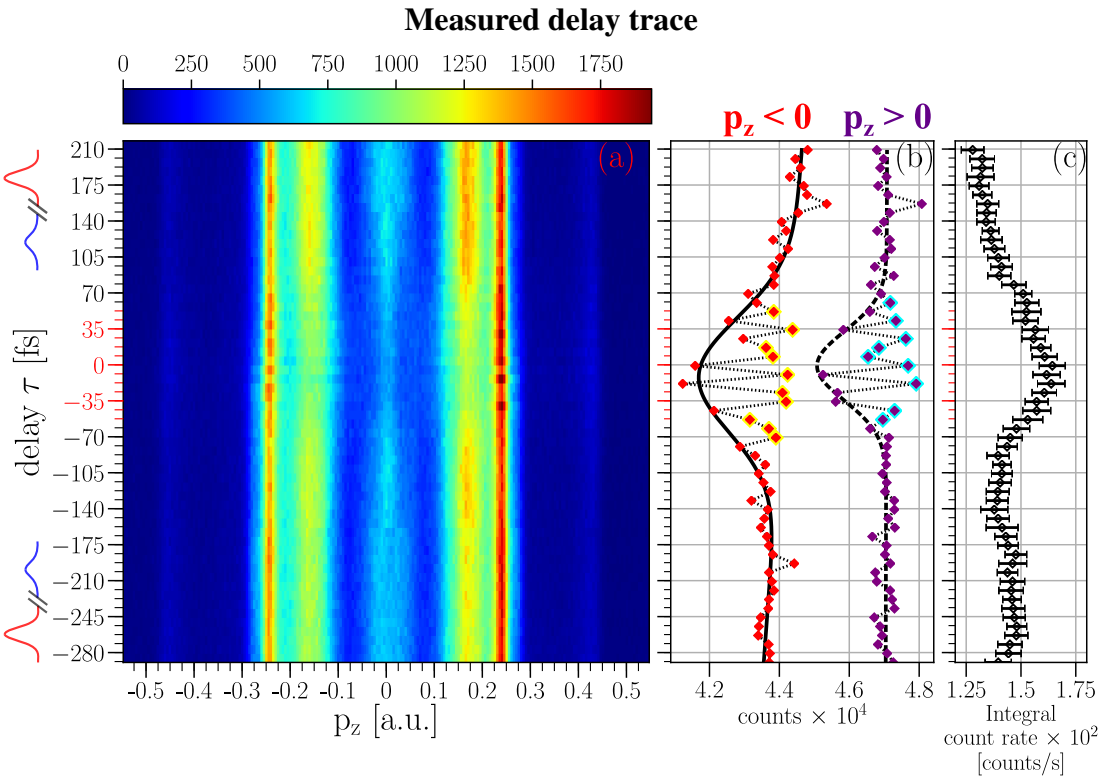

Figure 4.2.: (a) Measured delay trace of longitudinal momentum spectra in steps of 8.75 fs at an intensity ratio between the SH and the fundamental pulses of 0.3. (b) Integrated ionization yields over $p_z < 0$ (red diamonds) and $p_z > 0$ (purple diamonds) as a function of the delay. The black solid (dashed) curve is a Gaussian fit to selected data points without the yellow (blue) marked diamonds. The latter points show a rapid variation of the signal with the delay, which is indicated by the dotted lines to guide the eye. (c) Measured integrated count rate at each delay step. The error bars represent standard deviations. In (a) - (c), the red ticks of the delay axes correspond to the span of the average value of the FWHM extracted from Gaussian fits to positive and negative momentum data.

yield over $p_z < 0$ and $p_z > 0$ as a function of the delay τ as shown in Figure 4.2 (b). The temporal overlap range can be identified by oscillations of the integral ionization yields over positive and negative momenta, which are out of phase by 180° relative to each other.

To estimate the width of the pulse overlap delay range, we select data points for fitting to a Gaussian function. Within the pulse overlap range, we chose those data that show a reduced integrated ionization yield with respect to the delay range of non-overlapping pulses. The extracted FWHM amounts to 130 fs for $p_z < 0$ and 80 fs for $p_z > 0$. Assuming that both laser pulses have a Gaussian shape envelope and knowing the ratio of their duration, one can extract the duration of each pulse according to the relationship describing the standard deviation σ of a convolution of two Gaussian functions and the standard deviation of each Gaussian function, σ_1 and σ_2, as

$$\sigma = \sqrt{\sigma_1^2 + \sigma_2^2}. \tag{4.1}$$

For example, if we assume our two pulses have the same duration and their convolution

width is 100 fs, they have individual FWHM durations of 71 fs.

In addition to the onset of asymmetry, two-color ionization with temporally overlapping pulses is also associated with an increase in the integral ionization rate. In the simplest picture, this is explained by the nonlinear ionization rate as a function of the laser intensity for the present multiphoton process (see Eq. (1.4)). Thus, for summed intensities of the two-color pulses in the overlap region, the ionization rate is higher than the sum of the individual ionization rates in the non-overlap regions. Figure 4.2 (c) presents the measured integrated ionization rate at each delay step. Besides the enhancement within the overlap range, the rate is slightly higher for non-overlapping pulses at $\tau < 0$ than at $\tau > 0$. In the calculations discussed below (see Subsection 4.1.2), a similar enhancement at the negative delays can be observed in the integrated ionization yield over $p_z > 0$. There, it can be explained by the increase in the ionization yield of the 1^{st} ATI photoline at $\tau < 0$ compared to $\tau > 0$.

When calibrating the delay axis of (a), we selected $\tau = 0$ to be around the minima of both Gaussian fits in (b) and the maximum in (c). Therefore, we assumed that the symmetry center of the temporal overlap delay range corresponds to $\tau = 0$ between the two-color pulses. However, the calculations discussed in Subsection 4.1.2 show a slight shift of the symmetry center of the overlap feature towards negative delays. Therefore, for the measured delay traces, we do not know the actual location of $\tau = 0$.

4.1.1.2. Background subtraction

In all our measurements, strong ionization by single-color beams is present due to the imperfect matching of the two-color beam sizes and their profiles. Consequently, resolving the effect arising from two-color ionization on the longitudinal momentum spectra is difficult. Therefore, to eliminate the single-color background from the longitudinal momentum spectra, we process them by first calculating the average longitudinal momentum spectrum over the entire delay range and then subtracting it from the individual spectra measured at each delay step. Finally, we normalize the resulting data by setting the peak difference between the raw and the averaged data to 1.

The processed delay trace of the measured longitudinal momentum spectra is shown in Figure 4.3. It reveals the delay-dependent features of the longitudinal momentum spectra, which could not be resolved in the raw data. In the temporal overlap delay range, the out-of-phase oscillations between the negative and positive momentum sides of the longitudinal momentum spectra can now be seen directly, even without calculating the integral ionization yields as above. We also see that the momentum distributions within the temporal overlap delay range differ significantly from those within the non-overlap delay range. Furthermore, the measured longitudinal momentum spectra at $\tau < 0$ and $\tau > 0$ are not identical, regardless of whether it is the delay range of the overlapping or non-overlapping pulses. This contradicts the expectations described at the introduction of this section. Based on the enhancement or reduction in the longitudinal momentum-resolved ionization yield intensities, one can recognize the dominant partial wave character contributing to the spectrum at the particular delay range. We demonstrate this assignment in Subsection 4.1.3 when comparing the measurements

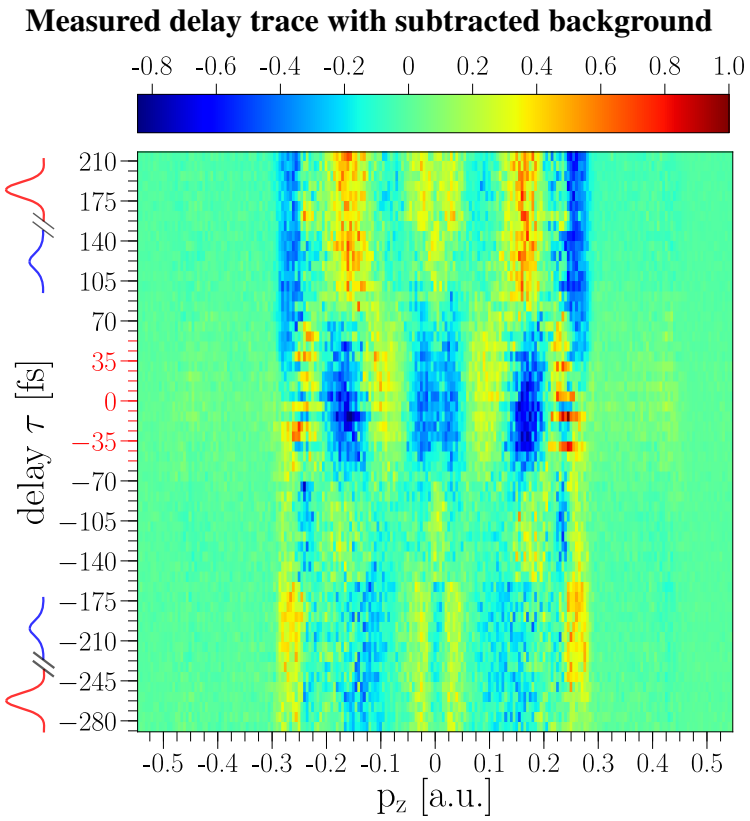

Figure 4.3.: Processed delay trace of Figure 4.2 (a) according to the steps described in the main text. The red ticks of the delay axis correspond to the span of the FWHM of the overlap delay range.

with the calculations.

4.1.2. Calculated delay trace

Figure 4.4 (a) shows raw data of the calculated delay trace of longitudinal momentum spectra. The limits of the delay range correspond to the onset of no overlap between the two-color pulses. The relative phase Φ between the fundamental and SH pulses is fixed to $\Phi = 0$. The delay step size is one optical cycle of the fundamental light. Consequently, the maximum left-right asymmetry is observed, and the longitudinal momentum distributions at $p_z < 0$ and $p_z > 0$ are out of phase.

In Figure 4.4 (b), the integrated ionization yield for $p_z > 0$ is shown and compared with a Gaussian with its width equal a convolution between the fundamental and SH pulses. The fundamental and SH pulse durations in these calculations are 34.3 fs and 36.5 fs, respectively. Interestingly, the peak integrated ionization yield is skewed towards negative delays, and it does not coincide with the zero delay of the pulses.

The longitudinal momentum spectra of the main photoline calculated at positive and negative delays between the two-color pulses, when only their wings are temporally overlapping, look identical as expected according to the ionization pathways explained in the introduction of this section. However, this is not the case for the peaks of the 1st ATI

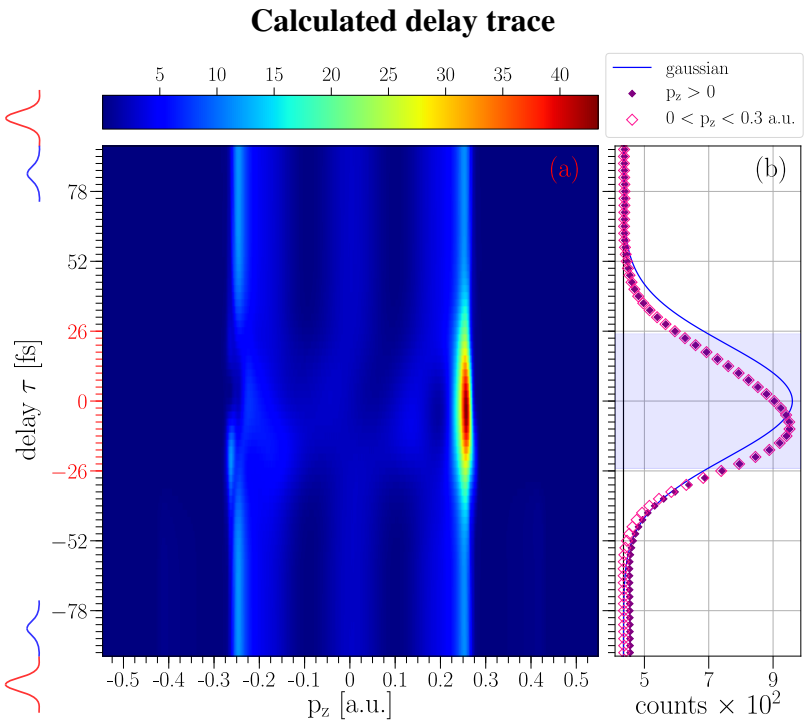

Figure 4.4.: (a) Calculated delay trace of longitudinal momentum spectra in steps of one optical cycle of the fundamental light, i.e., ~ 2.6 fs, at fundamental and SH pulse peak intensities of 6×10^{11} W/cm^2 and 2×10^{11} W/cm^2, respectively. (b) Integrated ionization yield over $p_z > 0$ (purple diamonds) and $0 < p_z < 0.3$ a.u. (open magenta diamonds). The blue curve is a Gaussian with its FWHM corresponding to a convolution of the fundamental and SH laser pulses used in the calculations. The black solid line is the baseline of the Gaussian, and the blue shaded area marks its FWHM. The red ticks in (a) correspond to the span of the FWHM.

photoline. From the comparison between the integrated ionization yields over $p_z > 0$ and $0 < p_z < 0.3$ a.u. in (b), where the latter momentum range only covers the main photoline, we conclude that at negative delays a slight enhancement in the integrated ionization yield results from the increase in the ionization yield of the 1st ATI photoline. This contradicts the expectations described in the introduction of this section, where based on the ionization pathways that excite the 1st ATI photoline, the increase in the ionization yield is expected at positive rather than negative delays. At this moment, we do not have an explanation for this contradiction.

4.1.3. Comparison between experiment and theory

We now compare delay traces of the measured and calculated longitudinal momentum spectra displayed in Figures 4.5 (a1) and (a2), respectively. They correspond to the processed raw data after the background subtraction described in Subsubsection 4.1.1.2 and symmetrizing each longitudinal momentum spectrum with respect to zero momentum. We symmetrize the delay traces because the original calculations yield a delay trace with the spectra being out of phase with respect to $p_z = 0$ (see Figure 4.4). Symmetrizing, on

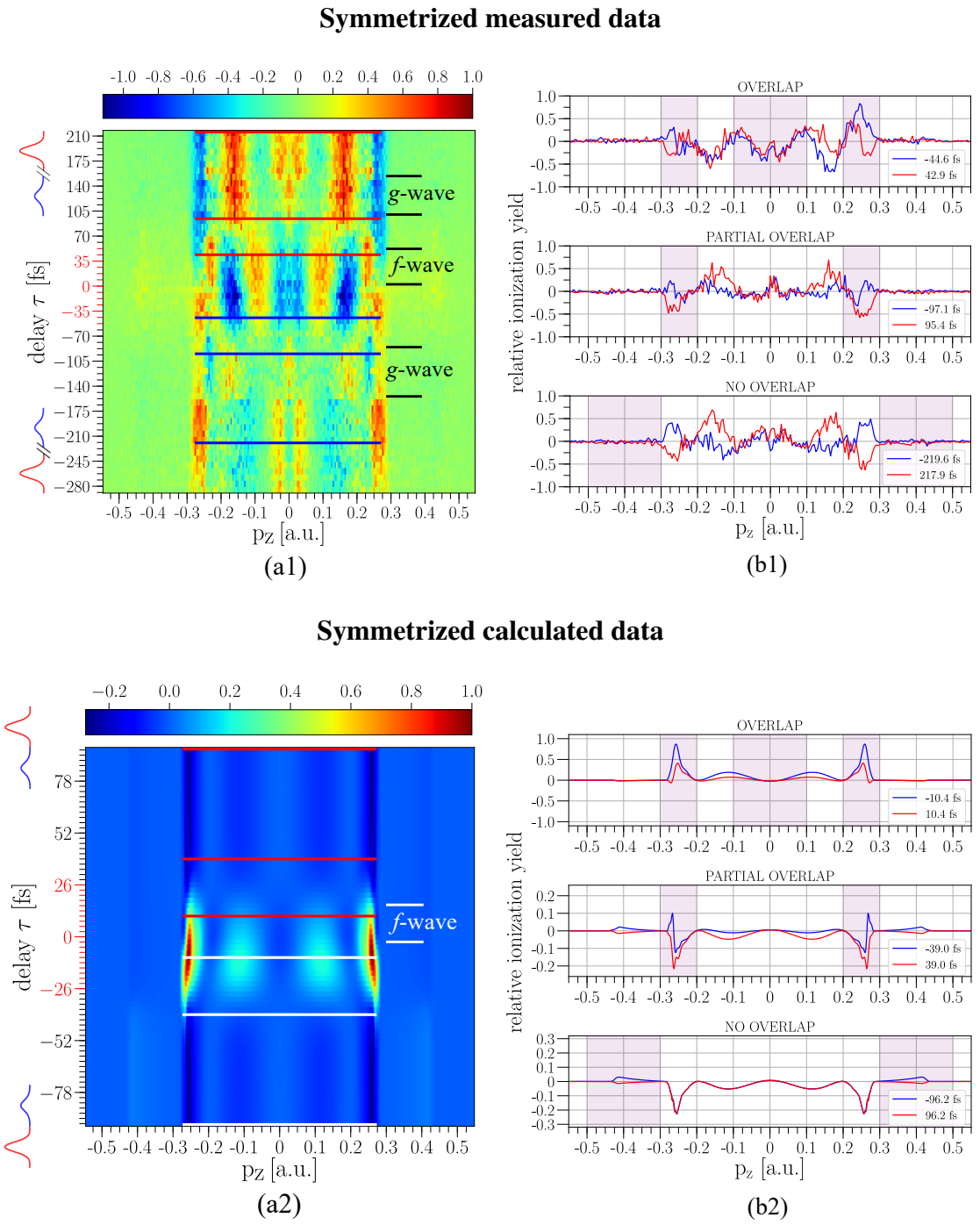

Figure 4.5.: (a1, a2) Symmetrized delay traces of longitudinal momentum spectra. Red ticks mark the span of the FWHM of the pulse overlap delay range. (b1, b2) Comparison between processed longitudinal momentum spectra at positive and negative delays within the overlap, partial overlap, and no overlap delay ranges between the two-color pulses. Purple-shaded areas mark features that appear both in experiment and theory. Red and white horizontal lines in (a1) and (a2) mark the delays of (b1) and (b2), respectively.

the contrary, helps to better identify the delay-dependent features.

We distinguish between the delay ranges, where the two-color pulses are overlapped ($|\tau|$ < FWHM), partially overlapped (FWHM < $|\tau|$ < 2 FWHM), and not overlapped ($|\tau|$ > 2 FWHM). Here FWHM refers to the width of the temporal overlap delay range in experiment and theory, which amounts to ~100 fs and 50 fs, respectively.

Within the delay range of the overlap and partial overlap, the calculations closely reproduce the photoelectron intensity pattern observed in the measurements. In contrast, disagreement is found in the non-overlap delay range. Since the intensity distribution of the photoelectron spectra strongly depends on the absolute and relative intensities of the two harmonics, the intensity changes during the measurements might account for this disagreement. In particular, we believe that the pulse intensities at $\tau < -157$ fs differed from the rest of the measurements.

Figure 4.6 shows examples of measured longitudinal momentum spectra at three different intensity ratios of the two harmonics. At each intensity ratio, measurements at three different absolute intensities are displayed. These data are measured at $\tau = 0$. Although we do not have data for the non-overlap delay range, we believe they might exhibit a similar dependence on the two-color field intensity as the photoelectron spectra of the overlap delay range. The measurements show that the enhancement of the intensity minima and the reduction of the maxima of the longitudinal momentum spectra becomes more pronounced with increasing absolute intensities and their ratios of the two harmonics.

Alternatively, the discrepancy between theory and experiment in the non-overlap delay range might be attributed to the unknown properties of the pulse shapes, e.g., a pedestal at the wings of the pulse envelopes. Although we have information about the temporal shape of the fundamental pulses (see Subsection 2.2.1), we do not know enough about the SH pulses. Therefore, even for large delays, there could be an overlap of the SH pulse with the fundamental pulse due to their possible weak pedestals.

In Figures 4.5 (b1) and (b2), a detailed comparison between the processed longitudinal momentum spectra at positive and negative delays for each delay range is presented. We see that the overlap region shows quite good agreement between the measured and calculated spectra. They both exhibit a minimum within $|p_z| < 0.1$ a.u., and at around $p_z \sim \pm 0.275$ a.u., the ionization yield is higher at negative than at positive delays. The latter feature appears and shows agreement within the partial overlap delay range as well. It relates to the PAD maxima at 0° and 180°, which are more localized at negative delay. Near zero delay, these maxima shift outwards both in experiment and theory. Within the non-overlap delay range, the calculations only reproduce the intensity ratios between the peaks of the 1st ATI photoline, but not of the main photoline.

The delay-dependent increase or decrease in the ionization yield at the minima and maxima of the longitudinal momentum spectra indicate changes in their partial-wave character with the delay. Ignoring the details, we can attribute a general partial wave character for several delay ranges as indicated in (a1) and (a2), e.g., the odd-parity f-wave for the overlap and the even-parity g-wave for no overlap (see also Figure 4.7). For a more detailed interpretation of delay-dependent photoelectron emission patterns, a fit to the data would be useful. However, due to the many partial waves contributing to

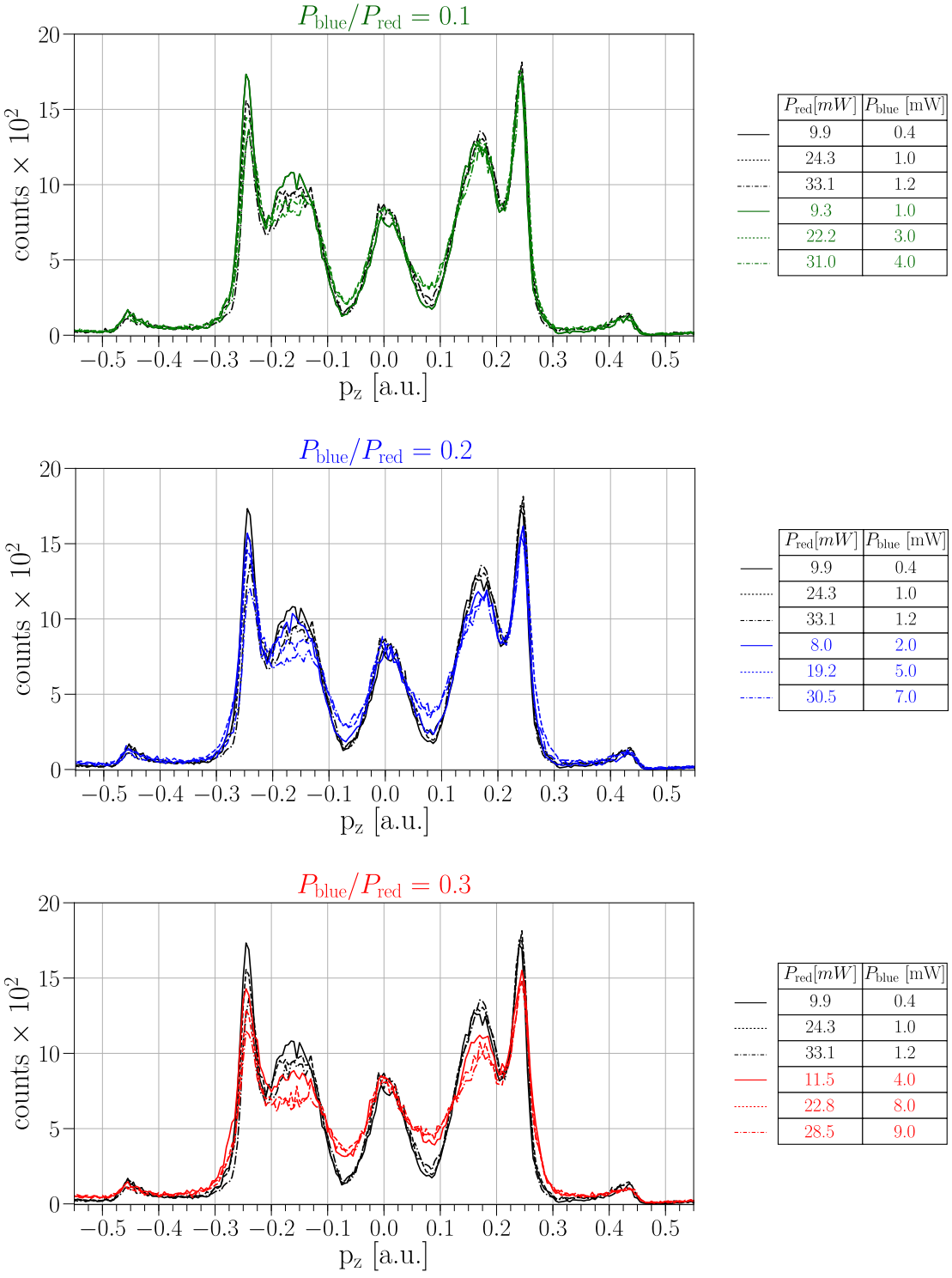

Figure 4.6.: Green, blue, and red curves: Longitudinal momentum spectra measured at three different average power ratios of the two harmonics. At each ratio, three longitudinal momentum spectra at different absolute beam powers are shown. Black curves: Longitudinal momentum spectra measured at different average powers of the fundamental light with a negligible fraction of the SH light so that their ratio is below 1%. These spectra serve as a reference to the spectra displayed in color to demonstrate the effect of increasing blue light fraction on the redistribution of the longitudinal momentum spectra. The average beam power is specified instead of the intensity since we cannot determine the latter directly. All spectra are measured at the delay $\tau = 0$.

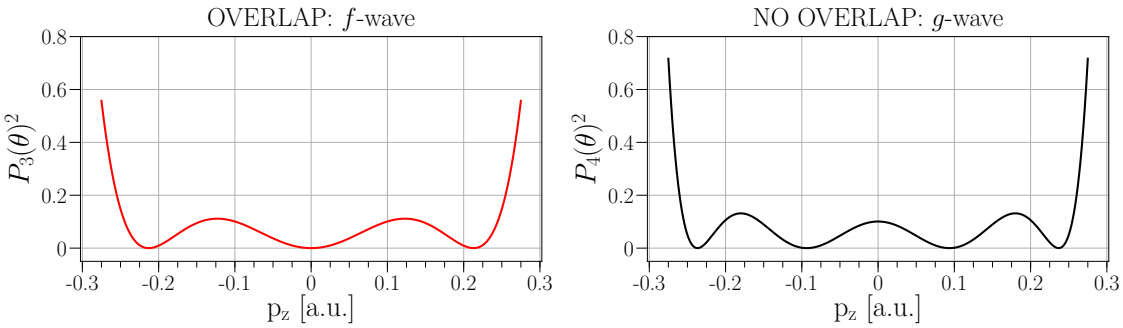

Figure 4.7.: Plots of squared Legendre polynomials describing the f- and g-waves in Cartesian coordinates.

the interference pattern as well as due to the subtracted background from the raw data, this task is not straightforward and not considered in this thesis.

4.2. Left-right asymmetry control of the PAD

In this Section, we describe our results for the coherent control of the left-right asymmetry of the PADs, which is achieved by changing the relative phase Φ between the fundamental and SH components of the two-color pulses with subwavelength accuracy. For these measurements, the delay was set to $\tau \approx 0$.

4.2.1. Relative phase Φ scan

Figures 4.8 (a) and (b) display measured and calculated relative phase Φ traces of PADs of the main photoline over two cycles of the blue light optical period, which is 1.3 fs. The Φ step sizes in the experiment and theory are $1/10^{\text{th}}$ and $1/8^{\text{th}}$ of the blue light optical period, respectively. The experimental and theoretical data shown correspond to the processed raw data after the average PAD over the entire scan range of the relative phase Φ has been subtracted from the individual PADs at each step of Φ. More details on the data processing can be found in Subsubsection 4.1.1.2. Good agreement is found between experiment and theory when appropriate absolute and relative intensities are used in the calculations. We see a left/right oscillation of the 0°/180° maxima but also respective oscillations of the 45°/135° and 90°.

4.2.2. Ionization yield modulation at various emission angles

Figure 4.9 shows the ionization yield modulation at various emission angles θ as a function of the relative phase Φ. These data correspond to those presented in Figure 4.8. Experiment and theory are in good agreement.

Our results reveal that the dependence of the ionization yield modulation on the relative phase Φ exhibits two pronounced characteristics. First, the oscillations of the ionization

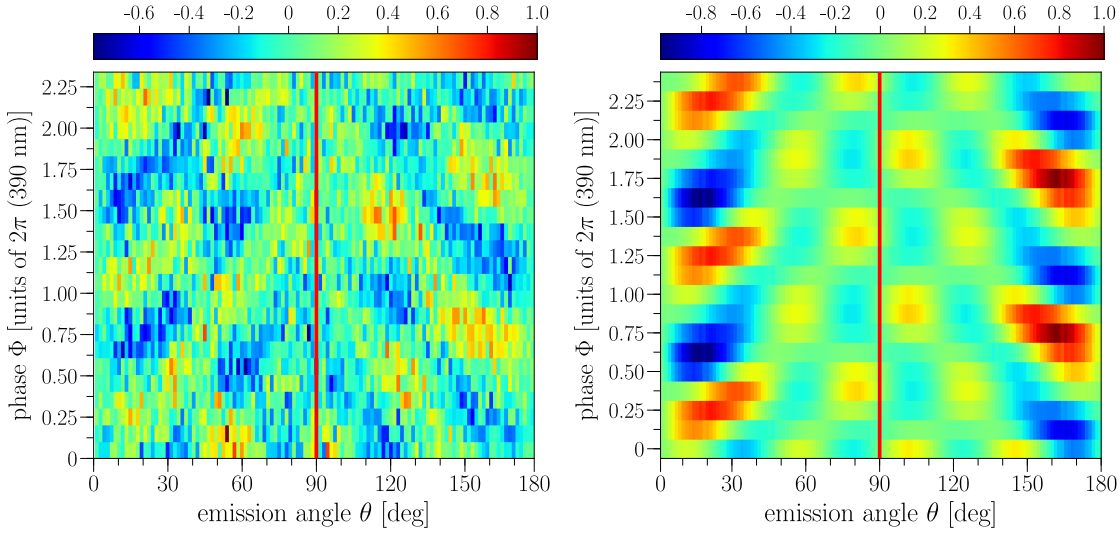

Figure 4.8.: (a) Measured and (b) calculated relative phase Φ traces of PADs of the main photoline with the background subtracted as described in Subsubsection 4.1.1.2. The measurements were performed at an intensity ratio of the SH and fundamental pulses of 0.3. The absolute intensities of the fundamental and SH pulses used in the calculations were 6×10^{11} W/cm^2 and 2×10^{11} W/cm^2, respectively.

yield modulation at opposite emission angles θ and $\pi - \theta$ are out of phase. Second, the oscillations exhibit an emission-angle-dependent phase shift. The same characteristics have been observed in similar experiments, where the left-right asymmetry of PADs was controlled via interference between one- and two-photon ionization pathways [11, 60]. In their recent work, You *et al.* [60] describe the origin of these characteristics. We summarize their explanation below.

The dependence of the ionization yield modulation $I(\theta, \Phi)$ at a fixed emission angle θ on the relative phase Φ is given by

$$I(\theta, \Phi) = A_0 + A\cos(\Phi - \Delta\eta(\theta)), \tag{4.2}$$

where A_0 is the signal offset, A is the amplitude, and $\Delta\eta(\theta)$ is the emission-angle-dependent phase shift determined by the phase difference between the even- and odd-parity partial waves induced via one- and two-photon ionization pathways. The ionization yield modulation at the emission angles $\pi - \theta$ can be derived based on the symmetry properties of the two-color laser field $E(t)$ (see Eq. 3.2). By reflecting $E(t)$ with respect to $\theta = 90°$, it gets inverted, i.e., $-E(t)$, and the relative phase Φ becomes $\Phi + \pi$. As a result, the ionization yield modulation at the emission angles $\pi - \theta$ can be written as

$$\begin{aligned} I(\pi - \theta, \Phi + \pi) &= A_0 + A\cos(\Phi + \pi - \Delta\eta(\pi - \theta)) \\ &= A_0 - A\cos(\Phi - \Delta\eta(\pi - \theta)), \end{aligned} \tag{4.3}$$

which oscillates out of phase relative to $I(\theta, \Phi)$.

Note that a simple cosine function cannot describe our results for the ionization yield modulation. This description applies to the interference schemes between one- and

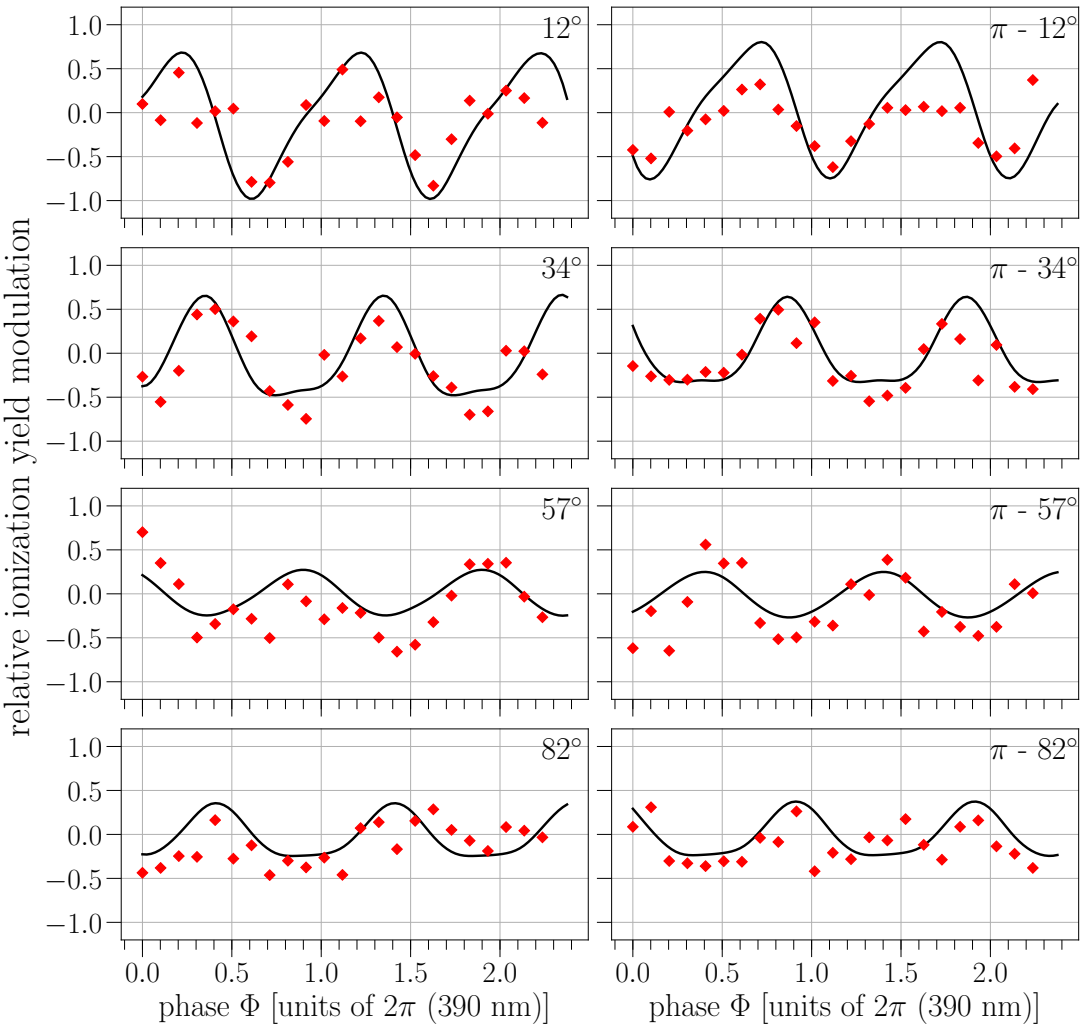

Figure 4.9.: Ionization yield modulation at various emission angles θ as a function of the relative phase Φ. Red diamonds: experimental data points. Black lines: theory.

two-photon ionization pathways and would require further development to describe the interference schemes between multiphoton ionization pathways.

The phase $\Delta\eta(\theta)$ corresponds to the emission-angle θ-dependent phase shift of the modulated ionization yield signal. It depends on the photoelectron kinetic energy and, thus, on the photon energy. You *et al.* [60] studied the dependence of $\Delta\eta(\theta)$ on the fundamental photon energy. They found that $\Delta\eta(\theta)$ changes more rapidly for photon energies resonant with or close to an intermediate bound state than for nonresonant photon energies. In their studies, You *et al.* also predicted that, for resonant photon energies, $\Delta\eta(\theta)$ depends on the absolute intensities of the two-color pulses.

In lithium, several intermediate resonances are excited (see Figures 3.3 and 3.4). Although the predictions and observations reported by You *et al.* cannot directly be related to our ionization scheme, they still provide insight into the role of intermediate resonances on $\Delta\eta(\theta)$. For example, we observe a rapid change in $\Delta\eta(\theta)$, which might result from the

resonant ionization pathways. Furthermore, theory predicts a dependence of $\Delta\eta(\theta)$ on the absolute intensities of the two harmonics. This is presented in Figure 4.10, although it is yet to be investigated experimentally.

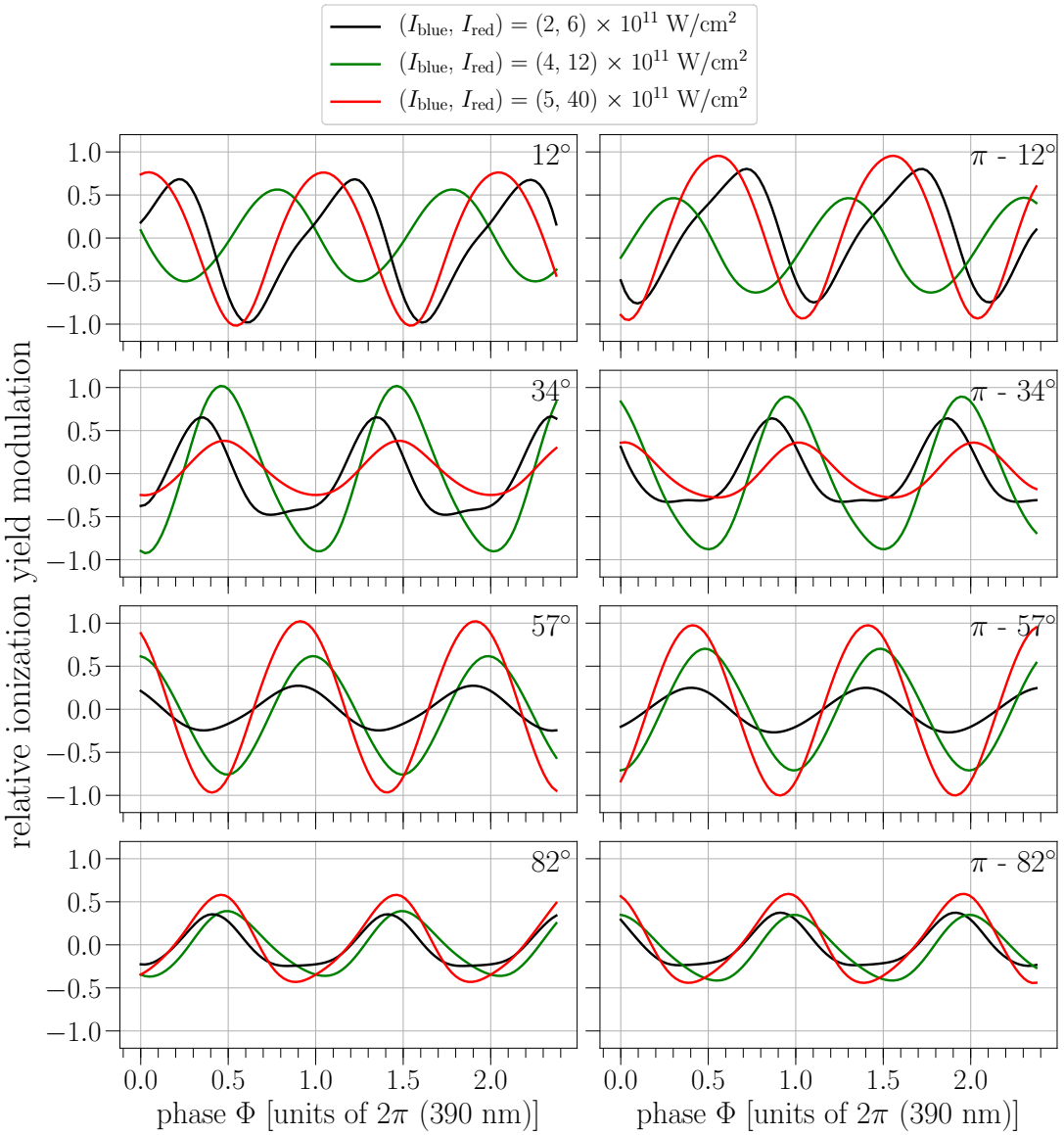

Figure 4.10.: Calculated dependence of the ionization yield modulation on the relative phase Φ at various emission angles θ for different absolute intensities and their ratios of the two harmonics.

4.2.3. Asymmetry parameter

The left-right asymmetry of the PADs can be quantified by the integral asymmetry parameter A_{LR} defined as

$$A_{LR} = \frac{I_L - I_R}{I_L + I_R}, \tag{4.4}$$

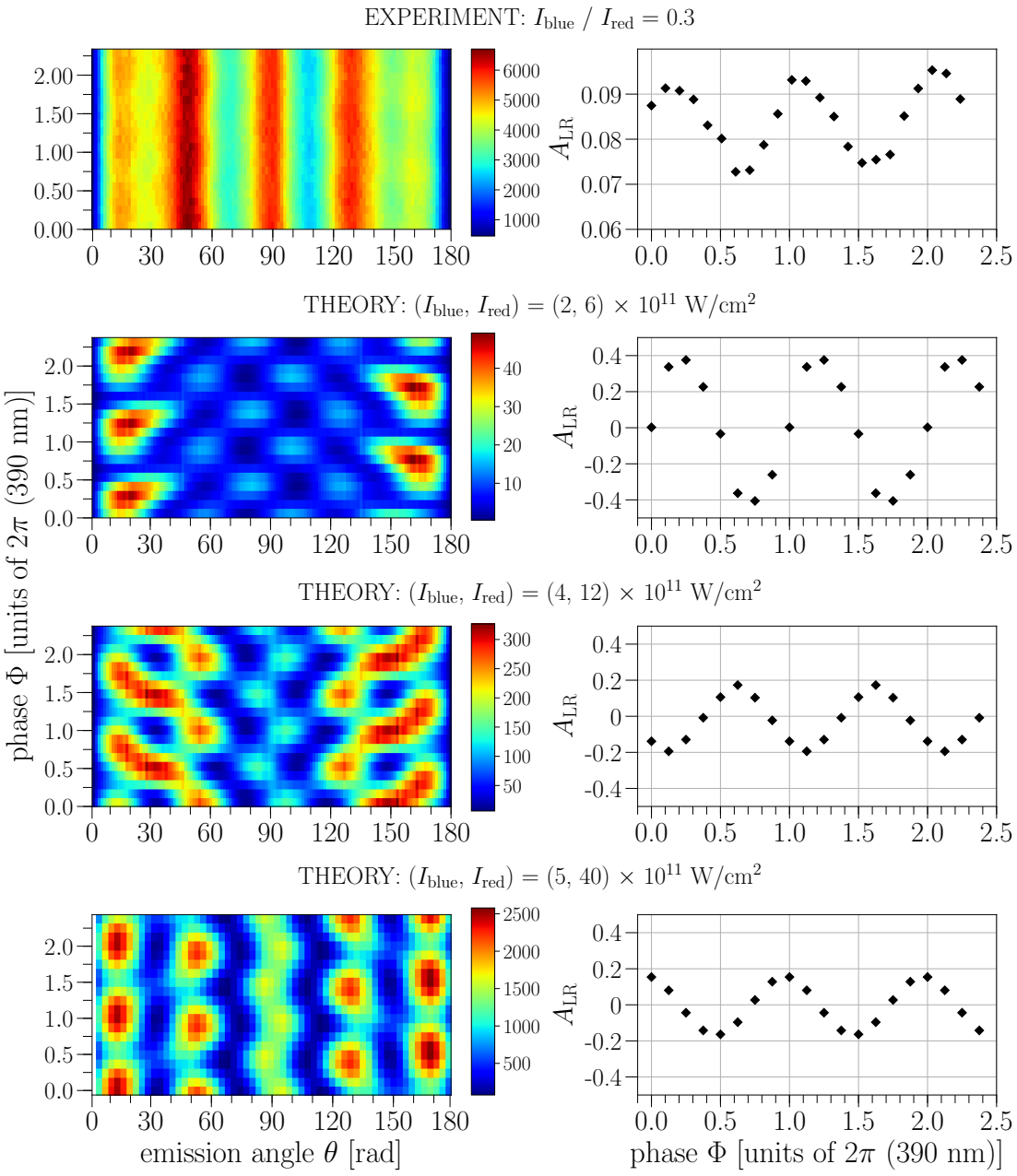

Figure 4.11.: Left column: raw measured and calculated relative phase Φ traces of PADs. Right column: Calculated integral asymmetry parameters A_{LR} of each trace.

where I_L is the integrated intensity of the PAD over emission angles $0 \leq \theta < \pi/2$, while I_R is obtained by integrating over $\pi/2 < \theta \leq \pi$ [13].

In the following, we exhibit our measured and calculated relative phase Φ traces of the PADs in terms of the A_{LR} parameter. Figure 4.11 shows the modulation of the asymmetry parameter A_{LR} as a function of the relative phase Φ for the measured PADs and the calculated PADs at three different sets of the fundamental and SH pulse peak intensities. A good phase agreement is found between the A_{LR} of the measured PADs

and the calculated PADs at $I_{\text{blue}} = 2 \times 10^{11}$ W/cm^2 and $I_{\text{red}} = 6 \times 10^{11}$ W/cm^2. We attribute the small modulation depth and the offset of A_{LR} in the experiment to strong ionization by single-color beams as explained earlier (see Subsubsection 4.1.1.2).

The modulation of A_{LR} in the calculated PADs exhibits a phase dependence on the absolute intensities of the fundamental and SH pulses. In recent theoretical studies on neon, a strong dependence of the phase of A_{LR} on the ionizing pulse intensities was found in the presence of resonant ionization transitions [61]. In particular, a phase jump of π is predicted close to a resonant intermediate state, and a gradual change of the phase by almost π is expected between the resonances. This scenario is very likely in lithium due to the presence of dynamic resonances with the Rydberg states considered in Section 3.2. We found out that the dynamic resonances at the various fundamental and SH pulse intensities used in the calculations lead to the population of different Rydberg states. This fact might account for the rapid changes in the phase shift of the A_{LR} modulation with the intensity of the two-color laser field. Experimental studies of the intensity-dependent population of various Rydberg states in lithium with 780 nm light were reported in a master thesis of our group [62] and in Ref. [63].

5. Conclusion and Outlook

This thesis presented results on the coherent control of the multiphoton ionization of ^{6}Li ground-state atoms using a bichromatic laser field with wavelengths of 780/390 nm. All experimental results were compared with theoretical predictions based on the numerical solution of the time-dependent Schrödinger equation in the single-active-electron approximation.

A delay scan between the second-harmonic pulse advancing the fundamental pulse and vice versa was performed to study the delay-dependent features of the photoelectron spectra. We considered both the main photoline and the 1st ATI photoline. Based on the intensity distributions of the photoelectron spectra at specific delay ranges, we could assign a dominant partial-wave character to several of them. In particular, the temporal overlap delay range clearly showed the presence of the odd-parity f-wave, whereas the non-overlap delay range exhibited features of the even-parity g-wave.

We also studied the effect of the interaction order of the two harmonics on the photoelectron spectra and compared the results with expectations according to the ionization pathways. We were interested in these studies due to intermediate resonances with long-living Rydberg states along several ionization pathways. While quite good agreement was found within the temporal overlap delay range between our measurements and the calculations, the non-overlap delay range showed discrepancies. The measured features in the main photoline did not agree with our expectations based on the ionization pathways or theory. We attributed the disagreement to either changes in the absolute intensities of the two colors during the measurements or the possible overlap of weak pedestals at the wings of the pulse envelopes. For the 1st ATI photoline, on the other hand, better agreement was found between experiment and theory. However, they both contradicted our expectations based on the ionization pathways. We have not yet found an explanation for this disagreement.

We performed a relative phase scan between the two harmonics with subwavelength accuracy at near-zero delay. We could demonstrate control of the left-right asymmetry of the photoelectron angular distributions of the main photoline. Good agreement was found with theory at the appropriate absolute intensities of the fundamental and the second-harmonic frequency components.

Until now, all experiments that demonstrated a left-right asymmetry control of the photoelectron angular distributions by changing the relative phase between the fundamental and second-harmonic pulses were based on the interference between single-photon and two-photon ionization pathways [11, 13, 14]. In this configuration, well-established theoretical models, for example, based on the proposal by Nakajima [12], can be applied to the measured PADs, which allow extracting the relevant photoionization parameters, such as phase differences between the continuum waves.

In contrast, our experiments involve interference between multiphoton transitions, i.e., the number of photons absorbed to overcome the ionization threshold ranges between two to four, leading to significant contributions from up to six partial waves. Due to this large number of partial waves, developing an analytical model to describe the asymmetric PADs is not straightforward in this case. Instead, one could fit the asymmetric PADs with a series of Legendre polynomials (see Eq. (1.9). Here, the current limitation is the low modulation contrast of our experimental data due to dominant ionization via single-color ionization pathways. The asymmetry contrast could be increased by matching the beam sizes and the profiles of the two colors.

Our scheme has the potential to study the role of intermediate resonances on the photoelectron angular distributions. Several effects predicted by the calculations but not yet investigated experimentally are discussed in this thesis. For example, in the presence of intermediate resonances, the PADs strongly depend on the absolute and relative intensities of the two harmonics. For experimental studies regarding the intensity dependence of the PADs, however, an interferometric two-color optical setup would be preferred instead of a collinear one. The former would enable an independent control of the intensity of the two colors. So far, experimental and theoretical studies on intermediate resonances occurring in two-color multiphoton ionization have been carried out with neon [13, 61].

In our laboratory, we recently demonstrated the preparation of lithium in its 2^2P excited state, followed by subsequent ionization with the second-harmonic radiation. These results are presented in Appendix A. Ionization of the 2^2P excited state via two-color multiphoton ionization would allow studying coherent control of the PADs resulting from ionizing the anisotropic initial state. However, prior to this, an optical pumping technique had to be employed to prepare the excited state in a particular magnetic sublevel of interest. At the moment, we can only prepare an unpolarized target of 2^2P excited lithium atoms with all of their magnetic sublevels being equally populated.

Another potential for studies of lithium would be to realize an ionization scheme based on the interference between single- and two-photon ionization pathways. While there has been experimental work on heavy alkalis like rubidium [11], this configuration would be intriguing because no experimental results are currently available for light alkalis such as lithium. In his proposal [12], Nakajima distinguishes between theoretical approaches devised for light and heavy alkalis. In the latter case, the spin-orbit interaction plays a significant role, whereas it can be neglected in the former, thereby simplifying the theoretical description.

A. Appendix: Preparation and ionization of the Li $(2p)^2P$ state

We prepare optically trapped ^{6}Li atoms initially in their $F = 1/2$ hyperfine ground state as described in detail in [36] in the 2^2P excited state by preparing two excitation pulses, which are resonant with the $F = 1/2 \rightarrow F'$ and $F = 3/2 \rightarrow F'$ transitions of the D_2 line. We name them RABI and REPUMPER, respectively (see Figure A.1). Because our femtosecond laser system operates at the 4 kHz repetition rate, we excite the atoms in a pulsed mode rather than a continuous wave (cw) mode. In this way, the number of scattering events followed by the absorption of excitation photons, which lead to the heating of the trapped atoms and subsequently to their loss from the trap, can be significantly reduced compared to the cw mode.

A.1. Rabi technique

We employ a Rabi technique typically applied in two-level systems for the population transfer. It is based on a coherent interaction between an exciting pulse and an atom. In the case of a resonant interaction, the Rabi frequency Ω is

$$\Omega = \sqrt{\frac{I_{\text{pulse}}}{2I_{\text{sat}}}}\,\Gamma, \tag{A.1}$$

where Γ is the natural linewidth of the excited state, I_{sat} is the saturation intensity of the optical transition, and I_{pulse} is the peak intensity of the excitation pulse. From this relation, a coherence condition can be derived. It is given as $\Omega \geq \Gamma$ or, in terms of the saturation intensity, as $I_{\text{pulse}} \geq 2I_{\text{sat}}$. Therefore, for the interaction to be coherent, the driving intensity must be at least twice the saturation intensity of the driven transition.

Because our ensemble of optically trapped atoms is unpolarized, we cannot establish an effective two-level system with a well-defined Rabi frequency. Instead, we drive all dipole-allowed transitions simultaneously, with their Rabi frequencies proportional to their dipole transition matrix elements. Different Rabi frequencies prevent us from reaching a high population transfer efficiency, as expected with a single Rabi frequency. However, in our experiment, we do not need to reach high transfer efficiencies. Figure A.2 illustrates undamped and damped Rabi oscillations for two different optical dipole transitions driven at the same laser intensity.

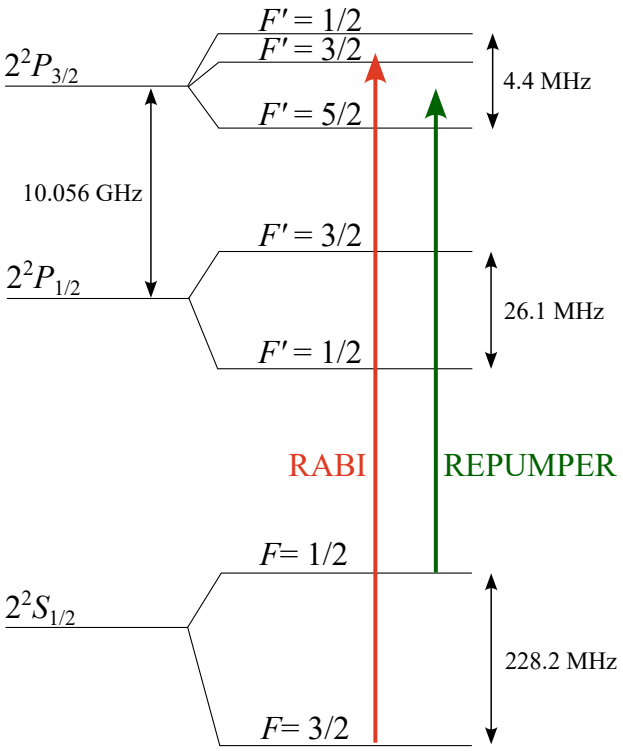

Figure A.1.: Energy level diagram of ^{6}Li with the relevant transitions for excitation of the 2^2P state.

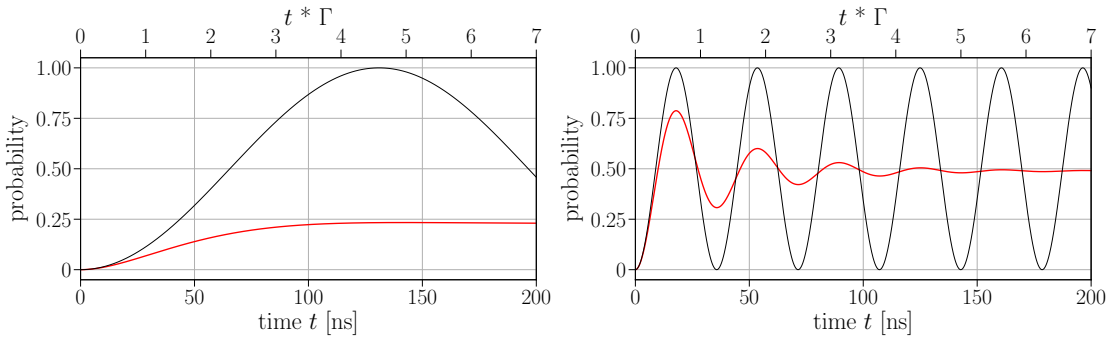

Figure A.2.: (a) $|F = 3/2, m_F = -3/2\rangle \rightarrow |F' = 5/2, m'_F = -5/2\rangle$. (b) $|F = 3/2, m_F = 1/2\rangle \rightarrow |F' = 1/2, m'_F = -1/2\rangle$. Black lines: Undamped Rabi oscillations. Red lines: damped Rabi oscillations with a decay time constant given by the natural lifetime of the 2^2P state, which is ~ 27 ns.

A.2. Excitation pulse generation

A.2.1. Optical setup

Figure A.3 shows a layout of the optical setup built for the following tasks:

- generate RABI pulses;
- spatially overlap the pulsed RABI and REPUMPER beams;

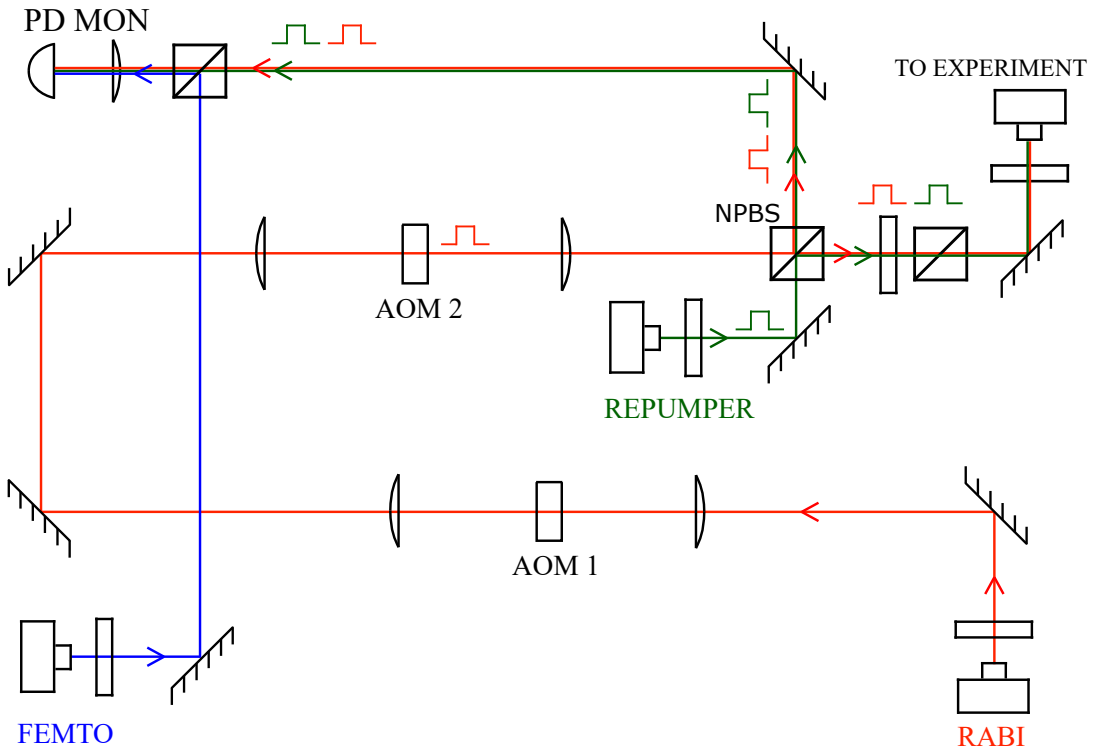

Figure A.3.: Optical setup. Orange line: RABI beam path. Green line: REPUMPER beam path. Blue line: beam path of the monitor light of the femtosecond laser.

- monitor RABI, REPUMPER, and FEMTO pulses on the same fast photodiode;
- fiber-couple overlapped beams for use in the experiment.

While the first acousto-optical modulator (AOM1) in the RABI beam path is used to shift the frequency, AOM2 generates the RABI pulses. REPUMPER pulses are produced in an external optical setup, and the pulsed REPUMPER beam is delivered to this optical setup via an optical fiber. The light for monitoring the femtosecond pulse train is picked up at the compressor input of our femtosecond laser using pellicles and is fiber-coupled for the delivery to this optical setup (see Figure A.4).

The RABI and REPUMPER pulses are spatially overlapped by using a nonpolarizing beam splitter cube (NPBS). NPBSs are manufactured with predefined fractions for the reflected and transmitted beam independently of the incoming beam polarization. Two spatially overlapped RABI and REPUMPER beam pairs emerge from the NPBS cube. One pair is guided to the monitor photodiode, whereas the other is fiber-coupled for use in the experiment.

A.2.2. Electronics

For creating the RABI pulses, we use an AOM MT250-A0,2-VIS (AOM2 in Figure A.3) and with it associated an RF driver MODA250 from AA OPTO-ELECTRONIC. This

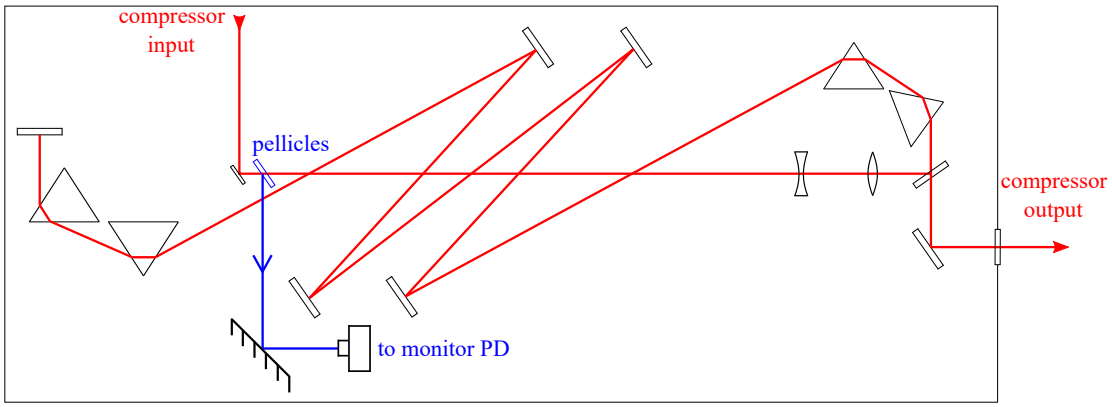

Figure A.4.: Implemented optics inside the femtolaser compressor to pick up the femtolaser monitor light reflected off the pellicles and fiber-couple it to guide it to the monitor photodiode.

AOM model is designed for high-speed applications, such as intensity modulation. A crucial specification of the AOM for generating short light pulses is the beam diameter inside the crystal. By focusing the RABI beam inside the AOM crystal down to ~ 55 μm, we generate pulses as short as ~ 30 ns. The pulse shape is defined via an analog input of the RF driver.

REPUMPER pulses are created with an AOM MT110-B50A1-VIS. RF electronics for driving this AOM and controlling the applied RF power strength include several RF components such as a Voltage Controlled Oscillator (VCO), RF switch, Voltage Controlled Attenuator (VCA), and an RF amplifier. Figure A.5 represents the applied RF circuit. Here, the pulses are defined by the TTL signal applied to the TTL input of the RF switch.

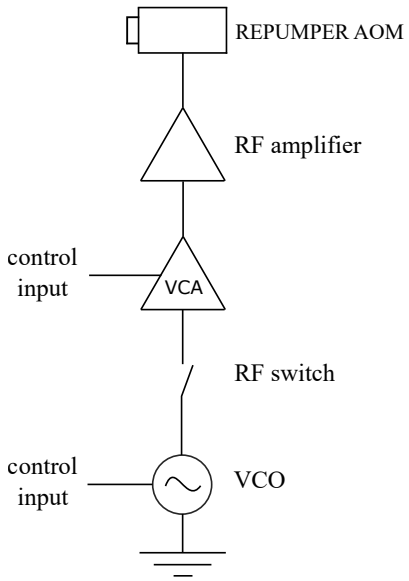

Figure A.5.: RF circuit for the REPUMPER pulse generation.

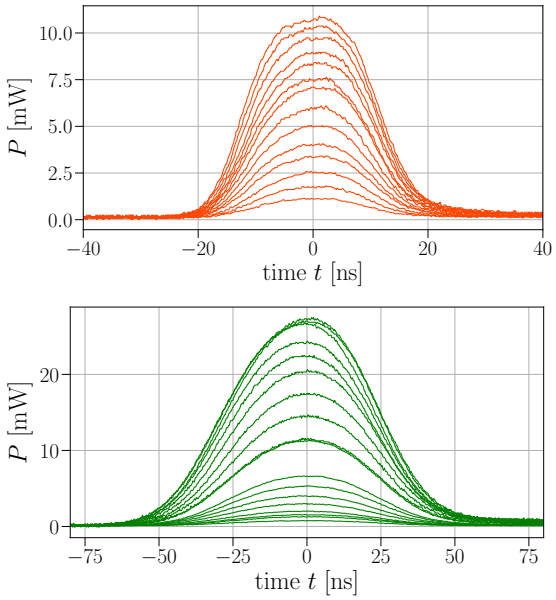

Figure A.6.: (a) RABI and (b) REPUMPER pulses at various pulse peak intensities.

Both analog pulses for the RABI RF driver and TTL pulses for the REPUMPER RF switch are generated by the same digital delay/pulse generator DG535 from Stanford Research Systems (SRS) (see Figure A.7). Outputs of this delay/pulse generator can be programmed to deliver TTL, ECL, NIM logic signals, or variable level (-3 to +4 V) pulses. We use its AB output to generate analog pulses applied to the RABI RF driver and its CD output for generating TTL pulses applied to the REPUMPER RF switch. The peak power of the RABI pulse can be varied via the set analog pulse amplitude, whereas that of the REPUMPER pulse using the VCA (Figure A.7) below. Figure A.6 shows pulse shapes of RABI and REPUMPER pulses at various pulse peak amplitudes detected on the monitor photodiode.

A.3. Triggering the excitation pulse train

To ionize the atoms in the excited 2^2P state, we need to synchronize the excitation pulses with the ionizing femtosecond laser pulses. Therefore, the pulse generator DG535 must trigger output signals at the repetition rate of our femtolaser, which is 4 kHz. Because it takes 800 ns for the pulse generator to reset all of its outputs after the longest delay, a second pulse generator (called DG535 II in Figure A.7) is connected in series with the first (called DG535 I in Figure A.7) to bridge its busy time when the next trigger event occurs.

A trigger signal is generated in the following way. From the photodiode signal of the monitored femtolaser output, NIM logic signals are generated by the constant fraction discriminator (CFD). The CFD output is applied as an external trigger to the DG535 I.

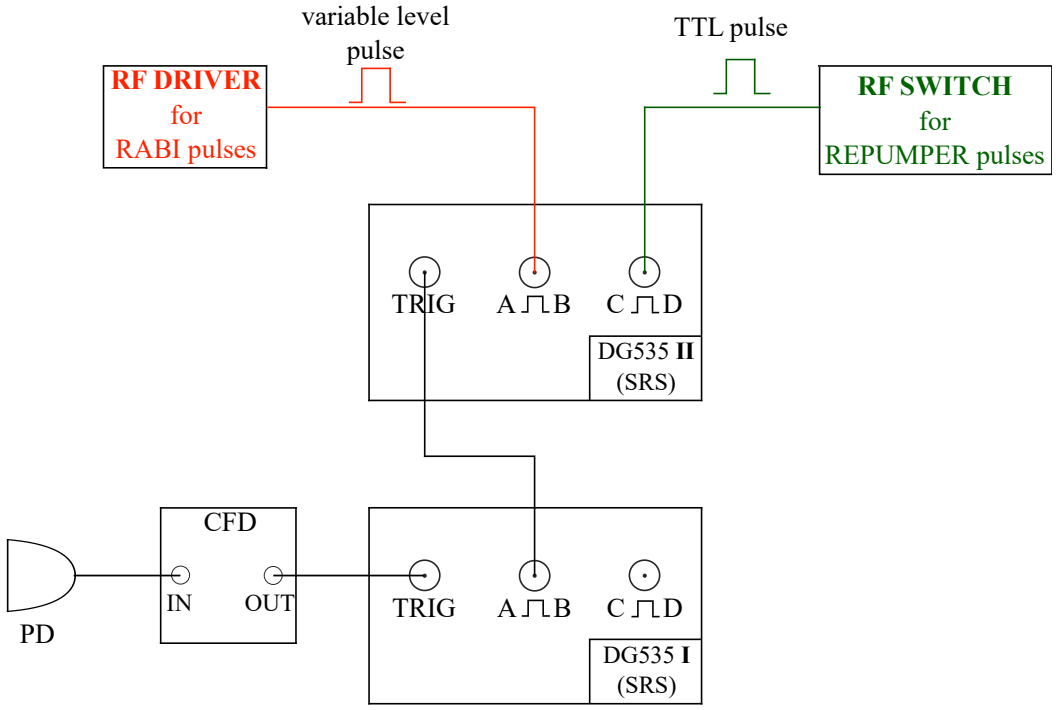

Figure A.7.: Schematics showing the processing of a trigger signal, which triggers the output of the DG535 I.

The signal of its output AB is also a NIM signal with a delay set to less than 250 μs with respect to the external trigger to avoid the above-mentioned busy time. This output is applied to a trigger input of DG535 II, which outputs the analog and digital signals required for generating the RABI and REPUMPER excitation pulses, respectively.

To summarize, by adjusting the delay of DG535 II, we can change the delay of both excitation pulses with respect to the femtosecond laser pulse simultaneously by the same amount. In contrast, the fact that RABI and REPUMPER pulses are generated from two independent output channels of DG535 II makes it possible to shift them in time with respect to each other, i.e., to make them either overlapped or separated in time. However, one should remember that the optically trapped atoms are initially in their F = 1/2 hyperfine ground state. From this, it follows that, in the case of temporally separated pulses, the RABI pulse has to arrive first, and the REPUMPER should follow it.

A.4. Ionization pathways

Ionization pathways induced by the fundamental and SH pulses starting from the 2^2S and 2^2P states are shown in Figure A.8. While the ionization of the 2^2S and 2^2P states by the fundamental pulses happens via intermediate resonances with Rydberg states, the

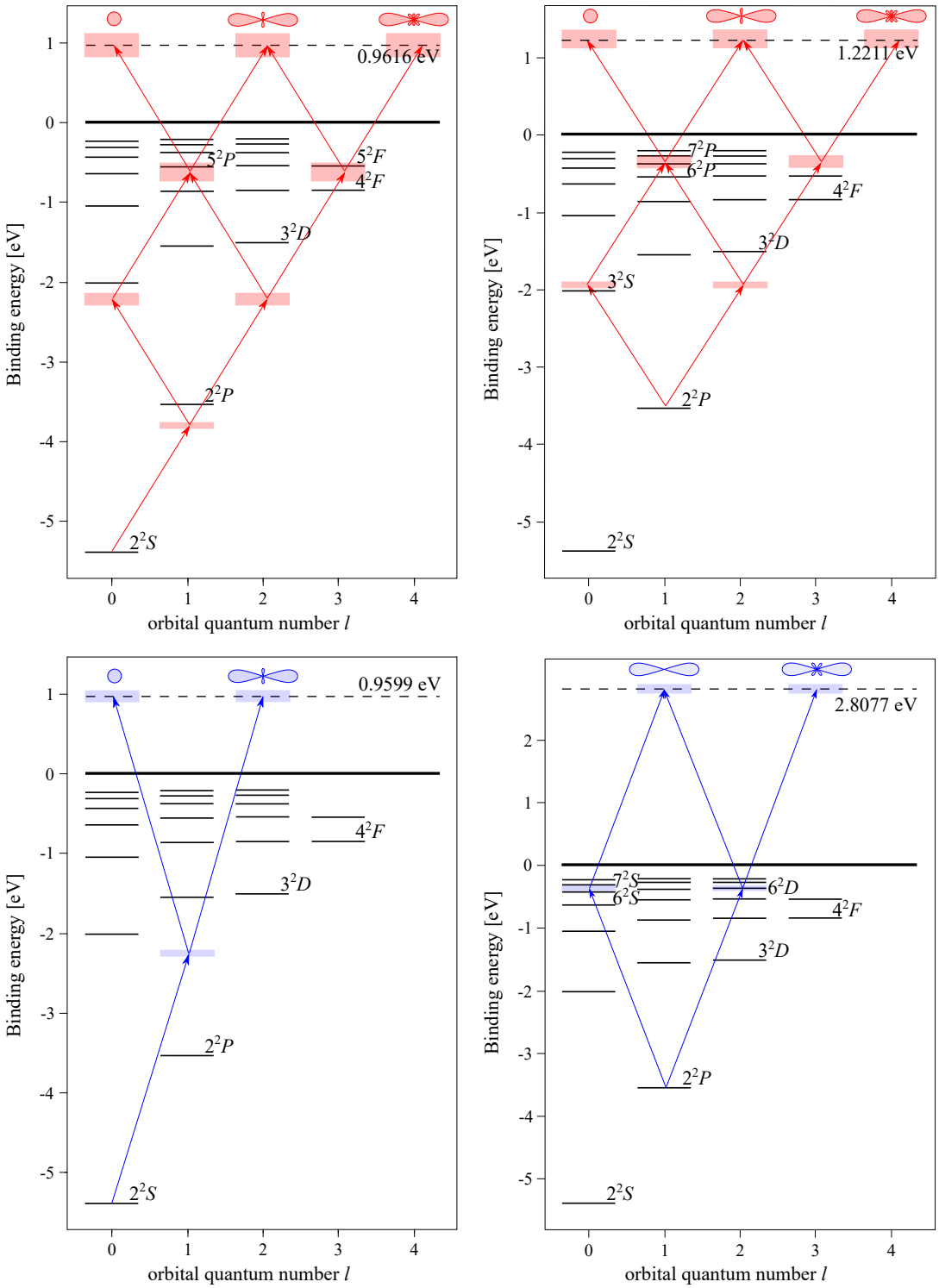

Figure A.8.: Energy level diagrams of ^{6}Li showing ionization pathways induced by the fundamental pulses in (a) and (b), and by the second-harmonic pulse in (c) and (d) starting from the 2^2S and 2^2P states, respectively.

SH pulses ionize the 2^2S state via direct absorption of two photons and the 2^2P state via an intermediate Rydberg state after absorption of a single photon. Therefore, when ionizing the 2^2P atoms with the SH pulse, we expect an increase in the ionization yield compared to ionization of the 2^2S state. We apply this fact to detect the temporal overlap between the excitation pulses and the ionizing femtosecond pulse as the temporal delay between them is changed.

A.5. Results for ionization of the 2^2P state with second-harmonic pulses

Figure A.9 shows a photograph of the oscilloscope screen, where the RABI, REPUMPER, and FEMTO signals detected by the monitor photodiode can be seen. Here, the RABI and REPUMPER pulses are temporally overlapped, and the spacing between the fringes corresponds to the energy difference between the hyperfine ground states.

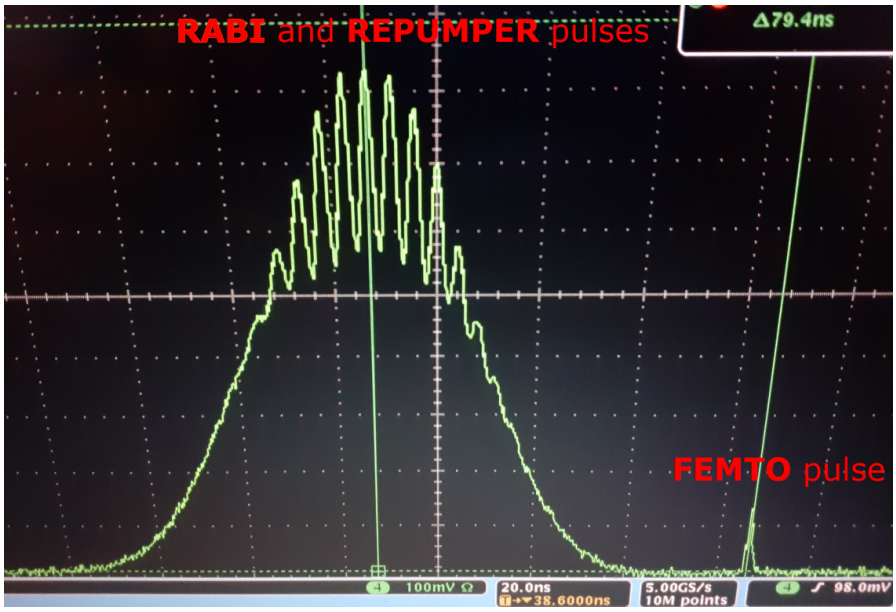

Figure A.9.: Photograph of the oscilloscope screen showing the temporally overlapped RABI and REPUMPER pulses, as well as the FEMTO pulse detected by the monitor photodiode.

A.5.1. Delay scan

Figure A.10 shows results of the 2^2P state ionization with the SH pulses when the delay between either both or at least one of the excitation pulses is changed. We see an increase in the ionization count rate when the FEMTO pulse is temporally overlapping with the excitation pulses. We attribute the higher peak count rate in the delay scan between the REPUMPER and FEMTO pulses displayed in (c) compared to the delay scan between the RABI and FEMTO pulses shown in (b) to the larger population in the F = 3/2 ground

state relative to $F = 1/2$ ground state. This follows directly from the branching ratios of the transitions between the excited 2^2P state and the two hyperfine ground states.

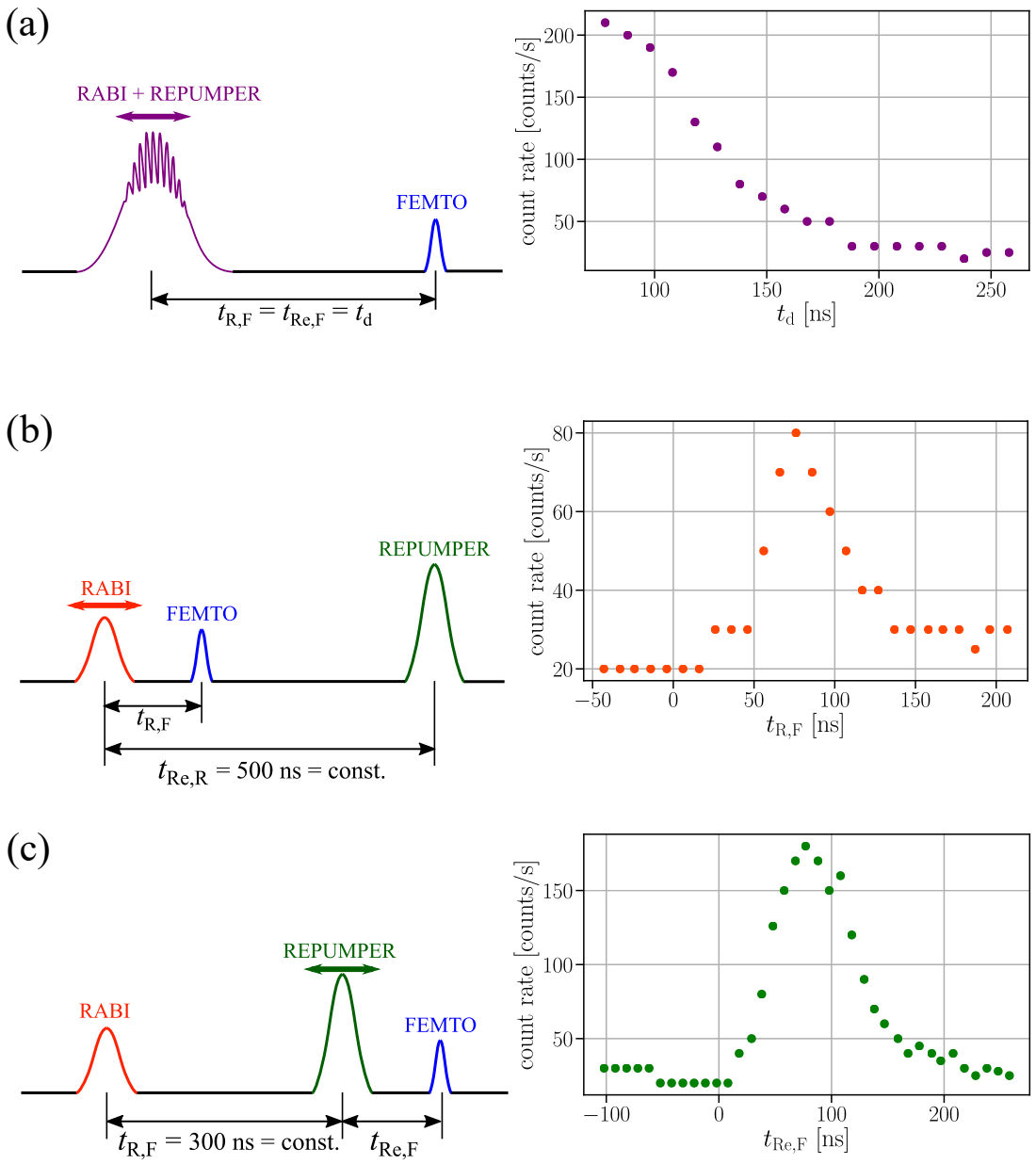

Figure A.10.: Delay change between the excitation pulses and the femtosecond laser pulse with an onset of the increased ionization count rate when the 2^2P atoms are detected, i.e., at least one of the excitation pulses overlaps with the ionizing FEMTO pulse. (a) Both RABI and REPUMPER pulses are temporally overlapped. Their delay is changed simultaneously with respect to the FEMTO pulse. (b) RABI and REPUMPER pulses are temporally separated, and their delay is fixed. The delay is varied between the RABI and FEMTO pulses. (c) RABI and REPUMPER pulses are temporally separated, and their delay is fixed. The delay is changed between the REPUMPER and FEMTO pulses.

A.5.2. Detuning scan

The results shown in Figure A.11 were obtained with temporally overlapping excitation pulses as depicted in Figure A.10 (a). They had an optimal overlap with the ionizing FEMTO pulse. Figure A.11 (a) shows the detected counts via fluorescence imaging of the optically trapped atoms. The optically trapped atoms interact with the pulsed excitation beam every 250 μs. The measurements were taken after the optical trap time of 200 μs. The loss maximum appears at the resonance and is associated with an increased excitation probability at small detuning. The loss maximum in the number of trapped atoms agrees with the measured increase in the ionization count rate close to the resonance. This result confirms that the increase in the ionization count rate arises from ionization of the atoms inthe 2^2P state.

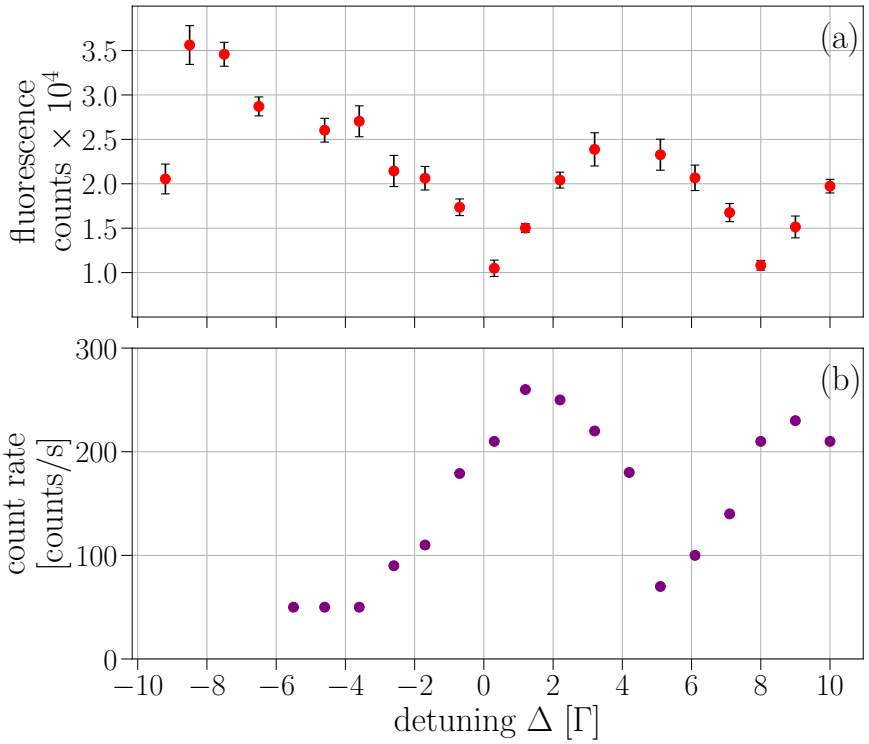

Figure A.11.: (a) Detected counts from the fluorescence imaging of the optically trapped lithium atoms as a function of the detuning of the temporally overlapped RABI and REPUMPER pulses. The atoms are imaged after the optical trap time of 200 ms. Excitation of ground-state lithium takes place every 250 μs. The error bars represent standard deviations. (b) Ionization count rate dependence on the detuning of the temporally overlapped excitation pulses. Here, the excitation pulses are optimally overlapped with the ionizing FEMTO pulse.

A.5.3. Ionization yield of the 2^2S and ^{2}P states

Figure A.12 shows measurements of the ionization count rate as a function of the ionizing beam power. We compare the ionization count rates of the 2^2S and 2^2P states. The

much higher count rate of the 2^2P ionization with the SH pulses is due to intermediate resonances with Rydberg states (see Figure A.8 (d)). As expected, the ionization count rate of the 2^2S atoms does not change with the detuning, whereas that of the 2^2P atoms exhibits a noticeable change.

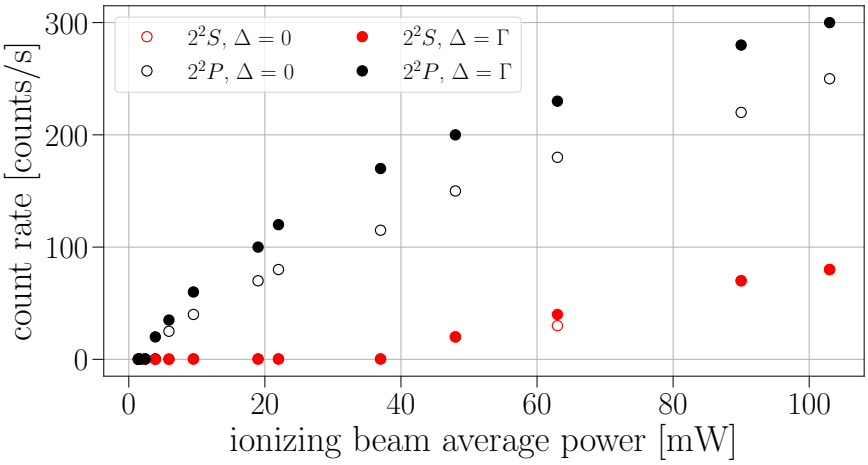

Figure A.12.: Measured ionization count rate as a function of the average power of the ionizing beam. The measurements are performed with atoms in the 2^2S and 2^2P states at two different detunings.

Bibliography

[1] N. Delone, E. Yankovsky, and V. Krainov. *Atoms in Strong Light Fields*. Springer Series in Chemical Physics. Springer Berlin Heidelberg, 2012. URL: https://books.google.de/books?id=R_ftoAEACAAJ (cit. on p. 9).

[2] C.-G. Wahlström, J. Larsson, A. Persson, T. Starczewski, S. Svanberg, P. Salières, P. Balcou, and A. L'Huillier. "High-order harmonic generation in rare gases with an intense short-pulse laser." In: *Phys. Rev. A* 48 (1993), p. 4709. URL: https://journals.aps.org/pra/abstract/10.1103/PhysRevA.48.4709 (cit. on p. 9).

[3] M. V. Ammosov, N. B. Delone, and V. P. Krainov. *High Intensity Laser Processes*. SPIE, 1986. URL: https://doi.org/10.1117/12.938695 (cit. on p. 9).

[4] N. B. Delone. "Multiphoton ionization of atoms." In: *Soviet Physics Uspekhi* 18 (1975), p. 169 (cit. on p. 9).

[5] K. J. Schafer, B. Yang, L. F. DiMauro, and K. C. Kulander. "Above threshold ionization beyond the high harmonic cutoff." In: *Phys. Rev. Lett.* 70 (1993), p. 1599. URL: https://link.aps.org/doi/10.1103/PhysRevLett.70.1599 (cit. on p. 9).

[6] P. B. Corkum. "Plasma perspective on strong field multiphoton ionization." In: *Phys. Rev. Lett.* 71 (1993), p. 1994. URL: https://link.aps.org/doi/10.1103/PhysRevLett.71.1994 (cit. on p. 9).

[7] J. Mauritsson, P. Johnsson, E. Gustafsson, A. L'Huillier, K. J. Schafer, and M. B. Gaarde. "Attosecond Pulse Trains Generated Using Two Color Laser Fields." In: *Phys. Rev. Lett.* 97 (2006), p. 013001. URL: https://link.aps.org/doi/10.1103/PhysRevLett.97.013001 (cit. on p. 9).

[8] I. J. Kim, C. M. Kim, H. T. Kim, G. H. Lee, Y. S. Lee, J. Y. Park, D. J. Cho, and C. H. Nam. "Highly Efficient High-Harmonic Generation in an Orthogonally Polarized Two-Color Laser Field". In: *Phys. Rev. Lett.* 94 (2005), p. 243901. URL: https://link.aps.org/doi/10.1103/PhysRevLett.94.243901 (cit. on p. 9).

[9] X. He, J. M. Dahlström, R. Rakowski, C. M. Heyl, A. Persson, J. Mauritsson, and A. L'Huillier. "Interference effects in two-color high-order harmonic generation." In: *Phys. Rev. A* 82 (2010), p. 033410. URL: https://link.aps.org/doi/10.1103/PhysRevA.82.033410 (cit. on p. 9).

[10] N. Dudovich, O. Smirnova, J. Levesque, Y. Mairesse, M. Y. Ivanov, D. M. Villeneuve, and P. B. Corkum. "Measuring and controlling the birth of attosecond XUV pulses." In: *Nature Physics* 2 (2006), p. 781. URL: https://www.nature.com/articles/nphys434 (cit. on pp. 9, 41).

[11] Y.-Y. Yin, C. Chen, D. S. Elliott, and A. V. Smith. "Asymmetric photoelectron angular distributions from interfering photoionization processes." In: *Phys. Rev. Lett.* 69 (1992), p. 2353. URL: https://link.aps.org/doi/10.1103/PhysRevLett.69.2353 (cit. on pp. 9, 56, 61, 62).

[12] T. Nakajima. "Possibility of direct determination of the quantum phase of continua utilizing the phase of lasers." In: *Phys. Rev. A* 61 (2000), p. 041403. URL: https://link.aps.org/doi/10.1103/PhysRevA.61.041403 (cit. on pp. 10, 61, 62).

[13] K. C. Prince et al. "Coherent control with a short-wavelength free-electron laser." In: *Nature Photonics* 10 (2016), p. 176. URL: https://doi.org/10.1038/nphoton.2016.13 (cit. on pp. 10, 33, 59, 61, 62).

[14] M. Di Fraia et al. "Complete Characterization of Phase and Amplitude of Bichromatic Extreme Ultraviolet Light." In: *Phys. Rev. Lett.* 123 (2019), p. 213904. URL: https://link.aps.org/doi/10.1103/PhysRevLett.123.213904 (cit. on pp. 10, 29, 61).

[15] P. M. Paul, E. S. Toma, P. Breger, G. Mullot, F. Augé, P. Balcou, H. G. Muller, and P. Agostini. "Observation of a Train of Attosecond Pulses from High Harmonic Generation." In: *Science* 292 (2001), p. 1689. URL: https://www.science.org/doi/abs/10.1126/science.1059413 (cit. on p. 10).

[16] H. G. Muller. "Reconstruction of attosecond harmonic beating by interference of two-photon transitions." In: *Applied Physics B* 74 (2002), p. 17. URL: https://doi.org/10.1007/s00340-002-0894-8 (cit. on p. 10).

[17] M. Schultze, M. Fieß, N. Karpowicz, J. Gagnon, M. Korbman, M. Hofstetter, S. Neppl, A. L. Cavalieri, Y. Komninos, T. Mercouris, C. A. Nicolaides, R. Pazourek, S. Nagele, J. Feist, J. Burgdörfer, A. M. Azzeer, R. Ernstorfer, R. Kienberger, U. Kleineberg, E. Goulielmakis, F. Krausz, and V. S. Yakovlev. "Delay in Photoemission." In: *Science* 328 (2010), p. 1658. URL: https://www.science.org/doi/abs/10.1126/science.1189401 (cit. on p. 10).

[18] H. Hertz. "Ueber einen Einfluss des ultravioletten Lichtes auf die electrische Entladung." In: *Annalen der Physik* 267 (1887), p. 983. URL: https://onlinelibrary.wiley.com/doi/abs/10.1002/andp.18872670827 (cit. on p. 13).

[19] L. V. Keldysh. "Ionization in the Field of a Strong Electromagnetic Wave". In: *J. Exp. Theor. Phys.* 20 (1965), p. 1307. URL: https://inspirehep.net/literature/1793133 (cit. on p. 13).

[20] "Symphony on strong field approximation". In: *Reports on Progress in Physics* 82 (2019), p. 116001. URL: https://dx.doi.org/10.1088/1361-6633/ab2bb1 (cit. on p. 13).

[21] H. B. Bebb and A. Gold. "Multiphoton Ionization of Hydrogen and Rare-Gas Atoms." In: *Phys. Rev.* 143 (1966), p. 1. URL: https://link.aps.org/doi/10.1103/PhysRev.143.1 (cit. on p. 15).

[22] C. J. Joachain, N. J. Kylstra, and R. M. Potvliege. *Atoms in Intense Laser Fields.* Cambridge University Press, 2011 (cit. on p. 15).

[23] J. Morellec, D. Normand, and G. Petite. "Resonance shifts in the multiphoton ionization of cesium atoms." In: *Phys. Rev. A* 14 (1976), p. 300. URL: https://link.aps.org/doi/10.1103/PhysRevA.14.300 (cit. on p. 15).

[24] V. Schyja, T. Lang, and H. Helm. "Channel switching in above-threshold ionization". In: *Phys. Rev. A* 57 (1998), p. 3692. URL: https://link.aps.org/doi/10.1103/PhysRevA.57.3692 (cit. on p. 15).

[25] P. Agostini, F. Fabre, G. Mainfray, G. Petite, and N. K. Rahman. "Free-Free Transitions Following Six-Photon Ionization of Xenon Atoms." In: *Phys. Rev. Lett.* 42 (1979), p. 1127. URL: https://link.aps.org/doi/10.1103/PhysRevLett.42.1127 (cit. on p. 16).

[26] J. Steinmann. "Multiphoton Ionization of Laser Cooled Lithium." PhD thesis. University of Heidelberg, 2007 (cit. on pp. 17, 24).

[27] L. A. L. Pan and J. H. Eberly. "Comments on the effect of the ponderomotive potential in the above-threshold ionization processes." In: *J. Opt. Soc. Am. B* 3 (1986), p. 1319. URL: https://opg.optica.org/josab/abstract.cfm?URI=josab-3-10-1319 (cit. on p. 16).

[28] R. Moshammer, D. Fischer, and H. Kollmus. *Recoil-Ion Momentum Spectroscopy and "Reaction Microscopes"*. Springer Berlin Heidelberg, 2003. URL: https://doi.org/10.1007/978-3-662-08492-2_2 (cit. on p. 19).

[29] J. Ullrich, R. Moshammer, A. Dorn, R. Dörner, L. P. H. Schmidt, and H. Schmidt-Böcking. "Recoil-ion and electron momentum spectroscopy: reaction-microscopes." In: *Reports on Progress in Physics* 66 (2003), p. 1463. URL: https://dx.doi.org/10.1088/0034-4885/66/9/203 (cit. on p. 19).

[30] R. Moshammer, J. Ullrich, M. Unverzagt, W. Schmidt, P. Jardin, R. E. Olson, R. Mann, R. Dörner, V. Mergel, U. Buck, and H. Schmidt-Böcking. "Low-Energy Electrons and Their Dynamical Correlation with Recoil Ions for Single Ionization of Helium by Fast, Heavy-Ion Impact." In: *American Physical Society* 73 (1994), p. 3371. URL: https://link.aps.org/doi/10.1103/PhysRevLett.73.3371 (cit. on pp. 19, 20).

[31] R. Moshammer, M. Unverzagt, W. Schmitt, J. Ullrich, and H. Schmidt-Böcking. "A 4 recoil-ion electron momentum analyzer: a high-resolution "microscope" for the investigation of the dynamics of atomic, molecular and nuclear reactions." In: *Nuclear Instruments and Methods in Physics Research Section B: Beam Interactions with Materials and Atoms* 108 (1996), p. 425. URL: https://www.sciencedirect.com/science/article/pii/0168583X95012591 (cit. on p. 19).

[32] J. Ullrich, R. Moshammer, R. Dörner, O. Jagutzki, V. Mergel, H. Schmidt-Böcking, and L. Spielberger. "Recoil-ion momentum spectroscopy." In: *Journal of Physics B: Atomic, Molecular and Optical Physics* 30 (1997), p. 1997. URL: https://dx.doi.org/10.1088/0953-4075/30/13/006 (cit. on p. 19).

[33] S. Sharma, B. P. Acharya, A. H. N. C. De Silva, N. W. Parris, B. J. Ramsey, K. L. Romans, A. Dorn, V. L. B. de Jesus, and D. Fischer. "All-optical atom trap as a target for MOTRIMS-like collision experiments." In: *Phys. Rev. A* 97 (2018), p. 043427. URL: https://link.aps.org/doi/10.1103/PhysRevA.97.043427 (cit. on p. 19).

[34] F. Thini, K. L. Romans, B. P. Acharya, A. H. N. C. de Silva, K. Compton, K. Foster, C. Rischbieter, O. Russ, S. Sharma, S. Dubey, and D. Fischer. "Photo-ionization of polarized lithium atoms out of an all-optical atom trap: a complete experiment." In: *Journal of Physics B: Atomic, Molecular and Optical Physics* 53 (2020), p. 095201. URL: https://dx.doi.org/10.1088/1361-6455/ab7671 (cit. on p. 19).

[35] "Coincident detection of recoil ions and photoelectrons after multiphoton-ionisation of cold 6Li atoms trapped in a dipole trap." In: *Journal of Physics: Conference Series* 1412 (2020), p. 122022. URL: https://dx.doi.org/10.1088/1742-6596/1412/12/122022 (cit. on pp. 19, 20).

[36] N. Kurz. "Kinematically complete multiphoton ionization studies on optically trapped ^{6}Li and $^6Li_2$ created by single-color photoassociation." PhD thesis. University of Heidelberg, 2021 (cit. on pp. 19, 20, 63).

[37] T. Arion and U. Hergenhahn. "Coincidence spectroscopy: Past, present and perspectives." In: *Journal of Electron Spectroscopy and Related Phenomena* 200 (2015), p. 222. URL: https://www.sciencedirect.com/science/article/pii/S0368204815001310 (cit. on p. 20).

[38] M. Schuricke. "Two and Three Photon Double Ionization of Lithium." PhD thesis. University of Heidelberg, 2012 (cit. on pp. 20, 21, 23).

[39] T. Weber, M. Weckenbrock, A. Staudte, L. Spielberger, O. Jagutzki, V. Mergel, F. Afaneh, G. Urbasch, M. Vollmer, H. Giessen, and R. Dörner. "Recoil-Ion Momentum Distributions for Single and Double Ionization of Helium in Strong Laser Fields." In: *Phys. Rev. Lett.* 84 (2000), p. 443. URL: https://link.aps.org/doi/10.1103/PhysRevLett.84.443 (cit. on p. 20).

[40] A. Fischer, A. Sperl, P. Cörlin, M. Schönwald, H. Rietz, A. Palacios, A. González-Castrillo, F. Martín, T. Pfeifer, J. Ullrich, A. Senftleben, and R. Moshammer. "Electron Localization Involving Doubly Excited States in Broadband Extreme Ultraviolet Ionization of H_2." In: *Phys. Rev. Lett.* 110 (2013), p. 213002. URL: https://link.aps.org/doi/10.1103/PhysRevLett.110.213002 (cit. on p. 20).

[41] A Rudenko, Y. H. Jiang, M Kurka, K. U. Kühnel, L Foucar, O Herrwerth, M Lezius, M. F. Kling, C. D. Schröter, R Moshammer, and J Ullrich. "Exploring few-photon, few-electron reactions at FLASH: from ion yield and momentum measurements to time-resolved and kinematically complete experiments." In: *Journal of Physics B: Atomic, Molecular and Optical Physics* 43 (2010), p. 194004. URL: https://dx.doi.org/10.1088/0953-4075/43/19/194004 (cit. on p. 20).

[42] J. L. Wiza. "Microchannel plate detectors." In: *Nuclear Instruments and Methods* 162 (1979), p. 587. URL: https://www.sciencedirect.com/science/article/pii/0029554X79907341 (cit. on p. 20).

[43] S. Sobottka and M. Williams. "Delay line readout of microchannel plates." In: *IEEE Transactions on Nuclear Science* 35 (1988), p. 348. URL: https://ieeexplore.ieee.org/document/12740 (cit. on p. 20).

[44] R. Hubele. "Kinematisch vollstandige und zustands-selektive Untersuchung der stossinduzierten Einfachionisation von Lithium." PhD thesis. University of Heidelberg, 2013 (cit. on p. 21).

[45] O. Jagutzki, A. Cerezo, A. Czasch, R. Dorner, M. Hattas, M. Huang, V. Mergel, U. Spillmann, K. Ullmann-Pfleger, T. Weber, H. Schmidt-Bocking, and G. Smith. "Multiple hit readout of a microchannel plate detector with a three-layer delay-line anode." In: *IEEE Transactions on Nuclear Science* 49 (2002), p. 2477. URL: https://ieeexplore.ieee.org/document/1046770 (cit. on p. 21).

[46] W. C. Wiley and I. H. McLaren. "Time-of-Flight Mass Spectrometer with Improved Resolution." In: *Review of Scientific Instruments* 26 (2004), p. 1150. URL: https://doi.org/10.1063/1.1715212 (cit. on p. 21).

[47] A. Senftleben. "Kinematically complete study of electron impact ionization of aligned hydrogen molecules." PhD thesis. University of Heidelberg, 2009 (cit. on pp. 22, 23).

[48] D. Strickland and G. Mourou. "Compression of amplified chirped optical pulses." In: *Optics Communications* 56 (1985), p. 219. URL: https://www.sciencedirect.com/science/article/pii/0030401885901208 (cit. on p. 24).

[49] B. Alonso, I. J. Sola, and H. Crespo. "Self-calibrating d-scan: measuring ultrashort laser pulses on-target using an arbitrary pulse compressor." In: *Scientific Reports* 8 (2018), p. 3264. URL: https://doi.org/10.1038/s41598-018-21701-6 (cit. on p. 25).

[50] M. Miranda, J. Penedones, C. Guo, A. Harth, M. Louisy, L. Neoričić, A. L'Huillier, and C. L. Arnold. "Fast iterative retrieval algorithm for ultrashort pulse characterization using dispersion scans." In: *J. Opt. Soc. Am. B* 34 (2017), p. 190. URL: https://opg.optica.org/josab/abstract.cfm?URI=josab-34-1-190 (cit. on p. 25).

[51] B. E. A. Saleh and M. C. Teich. *Fundamentals of photonics*. Wiley New York, 1991. URL: https://onlinelibrary.wiley.com/doi/book/10.1002/0471213748 (cit. on p. 39).

[52] D. G. Arbó, C. Lemell, S. Nagele, N. Camus, L. Fechner, A. Krupp, T. Pfeifer, S. D. López, R. Moshammer, and J. Burgdörfer. "Ionization of argon by two-color laser pulses with coherent phase control." In: *Phys. Rev. A* 92 (2015), p. 023402. URL: https://link.aps.org/doi/10.1103/PhysRevA.92.023402 (cit. on p. 40).

[53] J. Dai, N. Karpowicz, and X.-C Zhang. "Coherent Polarization Control of Terahertz Waves Generated from Two-Color Laser-Induced Gas Plasma." In: *Phys. Rev. Lett.* 103 (2009), p. 023001. URL: https://journals.aps.org/prl/abstract/10.1103/PhysRevLett.103.023001 (cit. on p. 40).

[54] R. Budriũnas. "Collinear Setup for Two-Color High-Harmonic Generation." BA thesis. Lund University, 2013 (cit. on p. 41).

[55] J. Dai. "Terahertz wave generation from gas plasma using a phase compensator with attosecond phase-control accuracy." In: *Applied Physics Letters* 94 (2009), p. 021117. URL: https://pubs.aip.org/aip/apl/article-abstract/94/2/021117/336860/Terahertz-wave-generation-from-gas-plasma-using-a?redirectedFrom=fulltext (cit. on p. 42).

[56] A. H. N. C. De Silva, D. Atri-Schuller, S. Dubey, B. P. Acharya, K. L. Romans, K. Foster, O. Russ, K. Compton, C. Rischbieter, N. Douguet, K. Bartschat, and D. Fischer. "Using Circular Dichroism to Control Energy Transfer in Multiphoton Ionization." In: *Phys. Rev. Lett.* 126 (2021), p. 023201. URL: https://link.aps.org/doi/10.1103/PhysRevLett.126.023201 (cit. on p. 45).

[57] A. H. N. C. De Silva, T. Moon, K. L. Romans, B. P. Acharya, S. Dubey, K. Foster, O. Russ, C. Rischbieter, N. Douguet, K. Bartschat, and D. Fischer. "Circular dichroism in atomic resonance-enhanced few-photon ionization." In: *Phys. Rev. A* 103 (2021), p. 053125. URL: https://link.aps.org/doi/10.1103/PhysRevA.103.053125 (cit. on p. 45).

[58] B. P. Acharya, M. Dodson, S. Dubey, K. L. Romans, A. H. N. C. De Silva, K. Foster, O. Russ, K. Bartschat, N. Douguet, and D. Fischer. "Magnetic dichroism in few-photon ionization of polarized atoms." In: *Phys. Rev. A* 104 (2021), p. 053103. URL: https://link.aps.org/doi/10.1103/PhysRevA.104.053103 (cit. on p. 45).

[59] B. P. Acharya, S. Dubey, K. L. Romans, A. H. N. C. De Silva, K. Foster, O. Russ, K. Bartschat, N. Douguet, and D. Fischer. "Two-path interference in resonance-enhanced few-photon ionization of Li atoms." In: *Phys. Rev. A* 106 (2022), p. 023113. URL: https://link.aps.org/doi/10.1103/PhysRevA.106.023113 (cit. on p. 45).

[60] D. You et al. "New Method for Measuring Angle-Resolved Phases in Photoemission." In: *Phys. Rev. X* 10 (2020), p. 031070. URL: https://link.aps.org/doi/10.1103/PhysRevX.10.031070 (cit. on pp. 56, 57).

[61] E. V. Gryzlova, A. N. Grum-Grzhimailo, E. I. Staroselskaya, N. Douguet, and K. Bartschat. "Quantum coherent control of the photoelectron angular distribution in bichromatic-field ionization of atomic neon." In: *Phys. Rev. A* 97 (2018), p. 013420. URL: https://link.aps.org/doi/10.1103/PhysRevA.97.013420 (cit. on pp. 60, 62).

[62] M. Schuricke. "Multiphoton Ionization of Lithium". MA thesis. University of Heidelberg, 2008 (cit. on p. 60).

[63] M. Schuricke, G. Zhu, J. Steinmann, K. Simeonidis, I. Ivanov, A. Kheifets, A. Grum-Grzhimailo, K. Bartschat, A. Dorn, and J. Ullrich. "Strong-field ionization of lithium." In: *Phys. Rev. A* 83 (2011), p. 023413. URL: https://journals.aps.org/pra/abstract/10.1103/PhysRevA.83.023413 (cit. on p. 60).

Acknowledgements

First, I would like to express my gratitude to Prof. Thomas Pfeifer, who gave me an opportunity to work out my thesis in his division. Thank you very much for your encouragement and for always finding time for helpful discussions whenever they were needed. Your faith in the success of your students is very uplifting. Thank you very much for your support.

I would also like to express my sincere thanks to my supervisor, Dr. Alexander Dorn. Working in your laboratory gave me a great opportunity to develop my experimental skills. Thank you also for your many suggestions to improve my work.

My gratitude goes to Prof. Klaus Bartschat. Klaus did all the calculations we asked him for and was always very helpful. His calculations certainly made the second half of this thesis. I am also very thankful for the time he invested in correcting my thesis. Thank you for your patience.

I am also grateful to Prof. Markus Oberthaler, who agreed to be the second referee of my thesis. Thank you very much for supporting me with your advice.

Finally, I am deeply grateful to my family for all the support during my studies.